GNSS-R AS A SOURCE OF OPPORTUNITY FOR REMOTE SENSING OF THE CRYOSPHERE

PhD Thesis Dissertation

By:

Fran Fabra

Instituto de Ciencias del Espacio (ICE-CSIC/IEEC)

Submitted to the Universitat Politècnica de Catalunya (UPC)
in partial fulfillment of the requirements for the degree of

Doctor of Philosophy

April 5, 2013

Advisor: Dr. Estel Cardellach (ICE-CSIC/IEEC)

Tutor: Dr. Adriano Camps (UPC/IEEC)

PhD program on Signal Theory and Communications

UNIVERSITAT POLITÈCNICA DE CATALUNYA
BARCELONATECH
Escola de Doctorat

Acta de qualificació de tesi doctoral

Curs acadèmic:

Nom i cognoms

Programa de doctorat

Unitat estructural responsable del programa

Resolució del Tribunal

Reunit el Tribunal designat a l'efecte, el doctorand / la doctoranda exposa el tema de la seva tesi doctoral titulada

_____

_____.

Acabada la lectura i després de donar resposta a les qüestions formulades pels membres titulars del tribunal, aquest atorga la qualificació:

☐ APTA/E ☐ NO APTA/E

(Nom, cognoms i signatura) President/a		(Nom, cognoms i signatura) Secretari/ària
(Nom, cognoms i signatura) Vocal	(Nom, cognoms i signatura) Vocal	(Nom, cognoms i signatura) Vocal

_____, _____ d'/de _____ de _____

El resultat de l'escrutini dels vots emesos pels membres titulars del tribunal, efectuat per l'Escola de Doctorat, a instància de la Comissió de Doctorat de la UPC, atorga la MENCIÓ CUM LAUDE:

☐ SÍ ☐ NO

(Nom, cognoms i signatura) Presidenta de la Comissió de Doctorat	(Nom, cognoms i signatura) Secretària de la Comissió de Doctorat

Barcelona, _____ d'/de _____ de _____

Abstract

This work evaluates the potential use of signals from the Global Navigation Satellite Systems (GNSS) that scatter off the Earth surface for the retrieval of geophysical information from the cryosphere.

For this purpose, the present study is based on data collected with a dedicated reflectometry GNSS receiver during two field campaigns, which were focused on two types of characteristic surfaces of the cryosphere: thin sea ice covers and thick dry snow accumulations.

During the first experiment, the complete process of formation, evolution and melting of sea ice was monitorized for more than seven months in a bay located in Greenland. This type of ice is typically characterized by its thickness, concentration and roughness. Different observables from GNSS reflections are analyzed to try to infer these properties.

The ice thickness is linked to the free-board level, defined as the height of the sea ice surface. Accurate phase altimetry is achieved, showing good agreement with an Arctic tide model. In addition, the long term results of ellipsoidal height retrievals are consistent with the evolution of the ice surface temperature product given by MODIS, which is a key parameter in the rate of growth of sea ice. On the other hand, the presence of salinity in the sea ice modifies its dielectric properties, resulting in different amplitude and phase for the co- and cross-polar components of the complex Fresnel coefficients. The polarimetric measurements obtained show good agreement with visual inspections of ice concentration from an Arctic weather station. Finally, the shape of the reflected signals and its phase dispersion are tested as potential signatures of surface roughness. For comparison, ice charts of the experimental area are employed. In particular, maximums in roughness given by the GNSS observables coincide with fast ice events. Fast ice is defined as ice anchored to the coast, where the tidal movements contribute to the development of strange patterns, cracks, and fissures on its surface, thus consistent with the GNSS-R roughness retrievals.

The second experiment took place on Antarctica, monitoring a pristine snow area which is well-known for the calibration of remote sensing instruments. Due to the relative stability of the snow layers, the data acquisition was limited to ten continuous days.

Interferometric beats were found after a first analysis of the amplitude from the collected signals, which were consistent with a multipath model where the reflector lies below the surface level. Motivated by these results, a forward model is developed that reconstructs the complex received signal as a sum of a finite number of reflections, coming from different snow layers (a snow density profile obtained from in-situ measurements). The interferometric information is then retrieved from the spectral analysis applied to time series from both real and modeled signals (lag-holograms). We find that the frequency bands predicted by the model are in general consistent with the data and the lag-holograms show repeatability for different days. Then, we attempt a proper inversion of the collected data to determine the dominant layers of the dry snow profile that contribute to L-band reflections, which are related to significant gradients of snow density/permittivity.

Resum

Aquest treball avalua el possible ús dels senyals dels sistemes mundials de navegació per satèl·lit (GNSS) que es reflecteixen a la superfície terrestre, per a l'extracció de la informació geofísica de la criosfera.

Amb aquest propòsit, el present estudi es basa en dades recollides amb un reflectòmetre GNSS durant dues campanyes experimentals, centrades en dos tipus de superfícies característiques de la criosfera: cobertes de gel marí i gruixudes acumulacions de neu seca.

En el primer experiment, el procés complet de formació, evolució i fusió del gel marí va ser monitoritzat durant més de set mesos a una badia situada a Groenlàndia. Aquest tipus de gel es caracteritza típicament amb el seu gruix, concentració i rugositat. Diferents observables de les reflexions GNSS són analitzats per tractar de fer una estimació d'aquestes propietats.

El gruix de gel està relacionat amb el nivell de francbord, que a la seva vegada està relacionat amb l'alçada de la superfície de gel marí. S'ha aconseguit altimetria de fase precisa, que mostra correlació amb un model de marea de l'Àrtic. A més, els resultats a llarg termini de l'alçada elipsoidal segueixen l'evolució de les mesures de temperatura de superfície de gel donades per MODIS. La temperatura és un paràmetre clau en el ritme de creixement del gel marí. Per altra banda, la presència de sal a aquest tipus de gel modifica les seves propietats dielèctriques, el que implica variacions d'amplitud i fase per als coeficients de Fresnel complexos amb polaritzacions oposades. Les mesures polarimètriques obtingudes mostren concordança amb els valors de concentració de gel obtinguts des d'una estació meteorològica propera. Finalment, la forma de la senyal reflectida i la dispersió de la seva fase s'evaluen com a potencials indicadors de la rugositat de superfície. Per a la seva comparació, es fan servir mapes del gel de la zona experimental. En concret, els valors màxims a la rugositat estimada a partir pels observables GNSS coincideixen amb el gel fixe, que es refereix a gel ancorat a la costa, on els moviments de les marees contribueixen al desenvolupament de patrons estranys, esquerdes i fissures en la seva superfície.

El segon experiment es va dur a terme a l'Antàrtida, monitoritzant una àrea de neu pristina que és ben coneguda per al calibratge d'instruments de teledetecció. A causa de la relativa estabilitat de les capes de neu, l'adquisició de dades es va limitar a deu dies consecutius.

Es van trobar pulsacions interferomètriques a partir d'un primer anàlisi de l'amplitud de les senyals recollides, les quals eren compatibles amb un model de propagació multicamí a on el reflector es troba per sota del nivell de superfície. Com a conseqüència d'aquests resultats, s'ha desenvolupat un model que reconstrueix el senyal complexe rebut com la suma d'un nombre finit de reflexions, procedents de diferents capes de neu (determinat per mesures locals). La informació interferomètrica es recupera després de l'anàlisi espectral aplicat a les sèries temporals tant de les senyals reals, com de les modelades (lag-holograms). Trobem que les bandes de freqüències predites pel model són en general consistents amb les dades i que els lag-holograms mostren repetibilitat per dies diferents. Posteriorment, es realitza un anàlisi de les dades recollides per determinar les capes dominants del perfil de neu seca que contribueixen a les reflexions en banda L, i que a la seva vegada, estan relacionades amb gradents significatius de densitat/permitivitat.

Resumen

Este trabajo evalúa el posible uso de las señales de los sistemas globales de navegación por satélite (GNSS) que se reflejan en la superficie terrestre para la extracción de información geofísica de la criosfera.

Con este propósito, el presente estudio se basa en datos recogidos con un reflectómetro GNSS durante dos campañas experimentales, centradas en dos tipos de superficies características de la criosfera: capas de hielo marino y gruesas acumulaciones de nieve seca.

Durante el primer experimento, el proceso completo de formación, evolución y fusión del hielo marino fue monitorizado durante más de siete meses en una bahía ubicada en Groenlandia. Este tipo de hielo se caracteriza típicamente por su grosor, concentración y rugosidad. Diferentes observables de las reflexiones GNSS son analizados para tratar de estimar dichas propiedades.

El espesor de hielo está relacionado con el nivel de francobordo o borda libre, que a su vez está relacionado con la altura de la superficie de hielo marino. Se ha logrado altimetría de fase precisa, mostrando correlación con un modelo de marea del Ártico. Además, los resultados a largo plazo de la altura elipsoidal siguen la evolución de las mediciones de temperatura de superficie de hielo proporcionadas por MODIS. La temperatura es un parámetro clave en el ritmo de crecimiento del hielo marino. Por otro lado, la presencia de sal en este tipo de hielo modifica sus propiedades dieléctricas, lo que implica variaciones en las amplitudes y fases de los coeficientes complejos de Fresnel con polarizaciones opuestas. Los resultados polarimétricos concuerdan con los valores de concentración de hielo obtenidos mediante inspección visual desde una estación meteorológica cercana. Por último, la forma de la señal reflejada y la dispersión de su fase son evaluadas como potenciales indicadores de la rugosidad de superficie. Para su comparación, se emplean mapas del hielo de la zona experimental. En particular, valores máximos de rugosidad estimada por los observables GNSS coinciden con hielo fijo, que se refiere al hielo anclado a la costa, donde los movimientos de las mareas contribuyen al desarrollo de patrones extraños, grietas y fisuras en su superficie.

El segundo experimento se llevó a cabo en la Antártida, monitorizando una área de nieve pristina que es bien conocida para la calibración de instrumentos de teledetección. Debido a la relativa estabilidad de las capas de nieve, la adquisición de datos se limitó a diez días consecutivos.

Se encontraron pulsaciones interferométricas a partir de un primer análisis de la amplitud de las señales recibidas, las cuales eran compatibles con un modelo de propagación multicamino donde el reflector se encuentra por debajo del nivel de la superficie. Como consecuencia de estos resultados, se ha desarrollado un modelo que reconstruye la señal recibida como la suma de un número finito de reflexiones, procedentes de diferentes capas de nieve (caracterizados por mediciones locales). La información interferométrica se recupera después del análisis espectral aplicado a las series temporales tanto de las señales reales, como de las modeladas (lag-hologramas). Encontramos que las bandas de frecuencias predichas por el modelo son en general consistentes con los datos y que los lag-hologramas muestran repetibilidad para días diferentes. Posteriormente, se realiza un análisis de los datos recogidos para determinar las capas dominantes del perfil de nieve seca que contribuyen a las reflexiones en banda L, y que a su vez, están relacionadas con gradientes significativos de densidad/permitividad.

Acknowledgements

This thesis is the result of a *journey* that I started a few years ago. Fortunately, I have not been *travelling* alone, and the work gathers the contributions of different people. My sincere acknowledgement to all of them:

First of all to my advisor, Estel Cardellach, for her keen guidance and dedication. Her enthusiasm for research is an exciting challenge for all who have the honor of working with her. Next, to the rest of the people from the Earth Observation group at ICE-CSIC/IEEC. In particular, to Antonio Rius, head of the group and probably the person from whom I have learned most during the last years; Serni Ribó, whose professionality keeps the group highly competitive in the GNSS-R community; Santi Oliveras and Juan Carlos Arco, the group masters of software and hardware respectively; and finally Oleguer Nogués, who left us the imprint of his expertise in the form of invaluable instrumentation, before embarking on his own professional way.

To the other people with whom I have shared my time at the institute: Sante Carloni, Nancy Elias, Josep Guerrero and the colleagues from the office at the "Eureka" building. This work has been surely benefited from such friendly work environment.

To my tutor at the UPC, Adriano Camps, for his expert comments and insights on remote sensing, and his efficient guidance through the administrative intricacies of the University.

It is also a pleasure to acknowledge the collaboration of people from other institutions who took part on the experimental campaigns where the datasets analyzed in this work were collected. In particular, Salvatore D'Addio, whose discussions in all the aspects of GNSS-R have been always enriching; Maximilian Semmling, who was in charge of the German equipment and datasets as a part of his equivalent *journey*; Maria Belmonte, the chief in remote sensing of sea ice, whose advises have been of irreplaceable help; Martin Sørensen, who provided valuable support during the installation setup in Greenland and helpful ancillary measurements afterwards; Giovanni Macelloni, who gave us the opportunity to put our equipment near the South Pole, and his inspiring suggestions related to remote sensing of snow have been of inestimable help; and Simone Pettinato, who after dedicating Christmas 2009 to do scientific work in Antarctica, made possible to obtain a priceless dataset for this thesis.

To Ismael Colomina and Manuel Martín-Neira, for their participation during the reviewing process. In the last case, my acknowledgment goes even further, due to his continuous support and leadership towards this amazing research field of GNSS-R.

To Alejandro Egido and Enric Valencia, whom, along with Max Semmling, have done similar *journeys* during these years, and it has been really encouraging to share our experiences. Guys, we did it!

Last but not least, to Naroa and my family. Their patience and comprehension during this time period have been more valuable than the wisest advice.

This work has been supported by the FPI grant BES-2009-012218 from the Spanish National Research AYA2008-05906-C02-02, and ESA Contract Number 21793/08/NL/ST. These grants are partially funded by the EU FEDER project.

"In general we look for a new law by the following process. First we guess it. Then we compute the consequences of the guess to see what would be implied if this law that we guessed is right. Then we compare the result of the computation to nature, with experiment or experience, compare it directly with observation, to see if it works. If it disagrees with experiment, it is wrong. In that simple statement is the key to science. It does not make any difference how beautiful your guess is. It does not make any difference how smart you are, who made the guess, or what his name is. If it disagrees with experiment, it is wrong. That is all there is to it."

The Character of Physical Law, Richard Feynman.

CONTENTS

LIST OF TABLES

LIST OF FIGURES

1

INTRODUCTION

1.1 MOTIVATION

The publication of the fourth assessment report by the Intergovernmental Panel on Climate Change (IPCC) (Solomon et al., 2007) has put climate change on the international agenda as one of the most important issue the world is currently facing. The report is based on a very large number of peer reviewed studies that over the years have been published on the topic. Given the societal importance of global warming an unprecedented effort has been put in trying to understand the processes responsible for the observed changes. Similar effort has been put in building new data-sets needed for assessing the skills of the models to reproduce current climate.

Climate scientists have known for quite some time that polar areas experienced an enhanced response to any change in climate as a consequence of a number of positive feedbacks (e.g. sea ice albedo) operating in the region. At the same time polar regions are also thought to be an important component of the climate system. For example the polar ice sheets have an important influence on the global water cycle by locking up or releasing large amounts of fresh water. Ice-sheet and polar caps are also affecting the radiation budget by modulating surface albedo. Finally the thermohaline overturning circulation, which to a large extent controls the heat transport between the tropics and the polar areas, is known to be controlled by the the amount of fresh water released to the ocean by ice melting.

It has been said (Eisen et al., 2008) that *"the understanding of the surface mass balance of the continental ice sheets is necessary to determine the present state of the ice sheet, to make predictions of its potential contribution to sea level rise and its consequences"*. It is also reported (Lemke et al., 2007) that due to the extreme polar environmental conditions, the surface mass balance and its most important parameter, the snow accumulation, are poorly retrieved. Moreover, the European Commission, through the GMES Bureau, has identified a set of Essential Climate Variables (ECV) the provision of which needs to be secured at European and global scale. Among them, the snow cover, glaciers, ice caps, sea ice and ice sheets are listed (Uppala et al., 2011; Stitt et al., 2011). Remote sensing systems aboard satellite are specially helpful for monitoring these areas.

Satellites represent an important source of data for climate studies given that a similar level of global coverage, spatial homogeneity and stability in time is nearly unobtainable with conventional instruments. This advantage comes to a cost which is intimately related to the remote sensing nature of the satellite data: the quality of the final data-set crucially depends on the quality of the retrieval technique used.

The use of space-based systems for tracking the Polar regions started approximately in the late 70's. Concretely, dealing with sea ice, a wide base of knowledge about mi-

crowave and optical signatures has been acquired since 1978, allowing the determination of the global extent of the ice cover over the oceans and to classify it into broad categories of age/thickness. The different techniques employed are mainly based on radar backscattering or radiometric measurements, including combinations of multiple sensors (Cavalieri et al., 1999; Andersen et al., 2006; Dedrick et al., 2001). By these means, the gradual loss of the sea ice both in the Arctic (Stroeve et al., 2005; Comiso et al., 2008) and the Antarctic (Shepherd et al., 2004) areas during the last years has been shown (Lemke et al., 2007). The characterization of the snow cover over large areas (Drinkwater et al., 2001; Markus et al., 2006) has been another potential use of these techniques.

Regarding remote sensing techniques suitable for cryospheric monitorization, a new approach was suggested in 1993: Passive Reflectometry and Interferometry System (PARIS) (Martín-Neira, 1993). It is based on the analysis of reflected L-band GPS signals and it was motivated by the availability of the GPS, GLONASS and (still) future Galileo and BeiDou-2/Compass constellation of navigation satellites. For this reason, the concept is usually referred as GNSS-R (Global Navigation Satellite Systems - Reflectometry). Despite being initially conceived for sea surface altimetry, this technique has been successfully proved for many other purposes, such as ocean wind speed retrieval (Garrison et al., 2002; Cardellach et al., 2003); soil moisture estimation (Masters et al., 2000; Katzberg et al., 2006); sea surface state determination (Cardellach, 2002; Rius et al., 2002; Clarizia et al., 2012); sea ice detection (Komjathy et al., 2000a); and sea ice classification (Belmonte-Rivas, 2007).

GNSS-R signals suppose an already existing and well characterized source of opportunity, given the vast experience with the GPS system and the availability of precise orbits and other detailed information. On the other hand, the inversion of parameters like ice extent, type and snow depth from other satellite data is based on a collection of rather ad hoc techniques, which in most cases require a priori statistical knowledge of the ice conditions and is encumbered by internal ambiguities (e.g. salinity vs. roughness in backscatter data or surface effects using thermal emissions). Therefore, the utilization of scattered GPS signals brings an excellent opportunity to promote the theoretical and empirical study of bistatic microwave signatures over the cryosphere and has the potential to provide a validating reference to current active and passive observation techniques. In addition, GNSS-R systems only need to deploy the receivers, and it leads to consider an inexpensive constellation of LEOs (Low Earth Orbiters) with global coverage and high spatio-temporal resolution (GNSS-R providing other suitable applications at mid- and Equatorial-latitudes).

1.2 GOALS

The aim of this study is to evaluate the potential of GNSS-R towards remote sensing over two types of ice extensions that characterize the cryosphere: thin –hundreds of centimeters– sea ice covers and thick –hundreds of meters– dry snow accumulations.

The work is mainly based on the analysis of experimental data gathered from fixed platforms during the GPS-SIDS (Global Positioning System - Sea Ice Dry Snow) project, an ESA's (European Space Agency) project carried on jointly by IEEC (Institut d'Estudis Espacials de Catalunya), GFZ (GeoForschungsZentrum), IFAC (Istituto di Fisica Applicata), DMI (Danmarks Meteorologiske Institut) and AD Telecom, with the purpose of collecting relatively long term high quality data sets of reflected GPS signals from Polar sea ice and dry snow scenarios for research interests.

The general research purpose of the present study can be split into the next list of more concrete objectives:

- To develop models for retrieving accurate altimetry (cm-level) from **sea ice** surface with GNSS-R.
- To develop models for retrieving roughness estimates of the **sea ice** cover with GNSS-R.
- To develop models for retrieving permittivity estimations of the **sea ice** cover with GNSS-R.
- To perform a **sea ice** characterization by combining the results obtained from the previous retrievals.
- To develop a model for L-band GNSS reflections off **dry snow** accumulations characterized by multiple layers with different snow density/permittivity.
- To develop a methodology to retrieve geophysical information from **dry snow** L-band GNSS reflections, such as the main contributor layers to the reflected signal.

1.3 OVERVIEW

In order to properly expose the different steps of knowledge needed to reach –or at least to be close enough– the research purposes previously described, the present dissertation is split into five chapters, each of them covering the following topics:

- **Chapter 2 - Background:** Description of the GNSS-R concept, enumeration of different techniques for remote sensing of the cryosphere and current state of the art. It is a compilation of useful information the understanding of it is required to better comprehend the bulk of the research. It does not provide detailed demonstrations, since this can be obtained from other bibliographic resources. Specially recommended for those readers without basic knowledge in GNSS-R.
- **Chapter 3 - GNSS-R Experimental System Analysis:** Description of the instrumental setup employed in the two field campaigns considered in this study, as well as a characterization of the scenarios' main aspects from each experiment. The author has contributed to the design and implementation of the high-level functionality of the setup; as well as on the campaigns' design, planning, preparation and monitorization.
- **Chapter 4 - Remote sensing of Sea Ice:** Analysis of applicability of GNSS-R for remote sensing of sea ice, including description of different techniques for the retrieval of relevant characteristics of sea ice and the results obtained for each case. The author has contributed with design and implementation of the processing algorithms and procedures; their validation; and end-to-end analysis.
- **Chapter 5 - Remote sensing of Dry Snow:** Analysis of applicability of GNSS-R for remote sensing of dry snow, including description of the developed model for GNSS L-band signals reflected off multiple dry snow layers and results obtained. As in the previous Chapter, the author has contributed with design and implementation of the processing algorithms and procedures; their validation; and end-to-end analysis.
- **Chapter 6 - Summary, conclusion and future work:** Synopsis and recommendations for future work with dedicated comments for each of the two main themes in this study.

Figure 1 provides a flowchart of the different chapters and their basic contents with the aim to serve as a guidance for the reader through this dissertation. A complete list of the acronyms and symbols/variables employed during this work is given in Appendix A. Table 1 enumerates the publications issued from the study presented along this dissertation. Finally, the experimental GNSS-R datasets analyzed here are publicly available for the scientific community at the web server described in Appendix B.

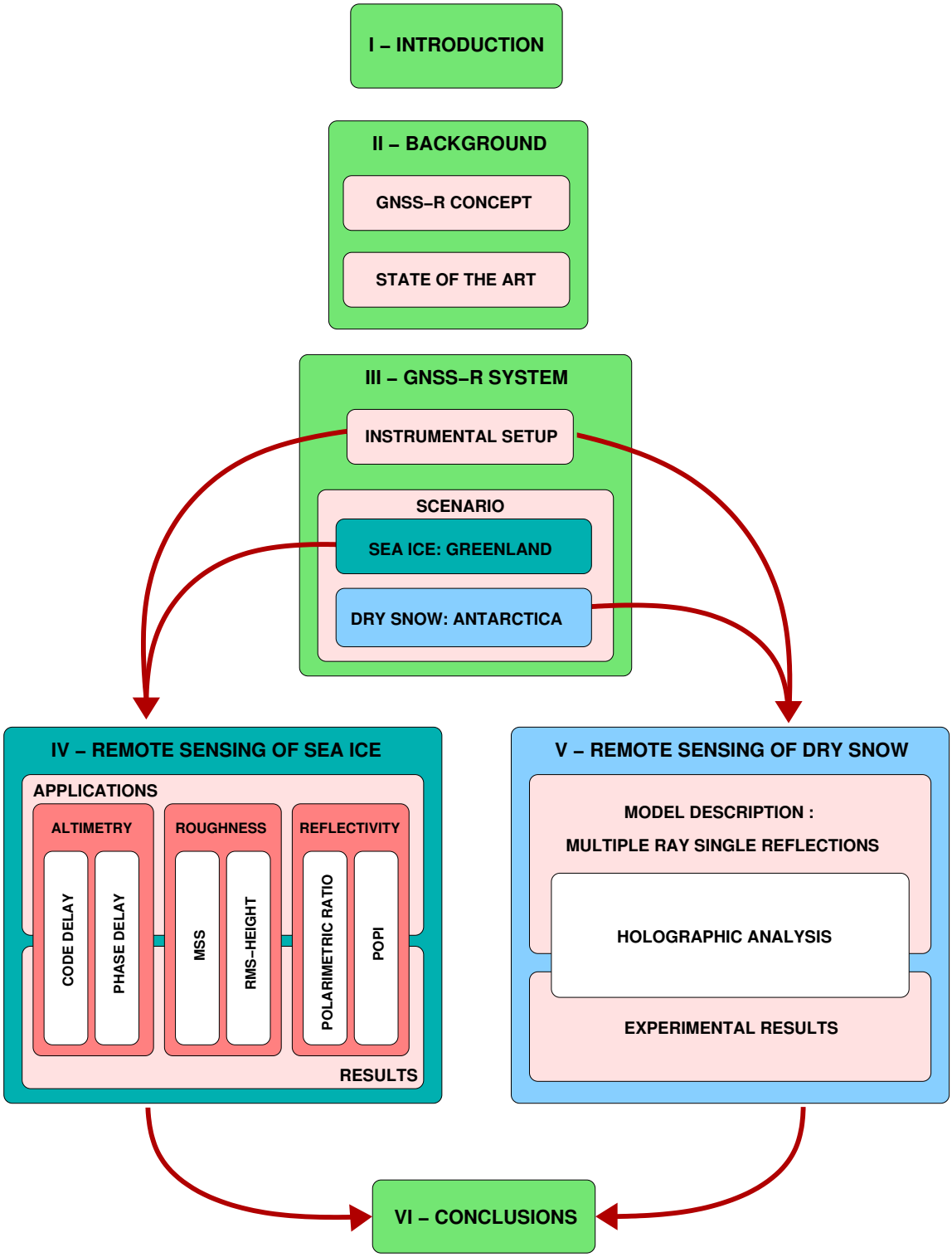

Figure 1.: Flowchart of the different chapters that compose this dissertation and their basic contents.

Title	Reference
Sea Ice remote sensing with GNSS Reflections	Fabra et al. (2009)
Monitoring sea ice and dry snow with GNSS reflections	Fabra et al. (2010)
Detection of Arctic Ocean Tides using Interferometric GNSS-R Signals	Semmling et al. (2011)
An empirical approach towards characterization of dry snow layers using GNSS-R	Fabra et al. (2011a)
Phase Altimetry with Dual Polarization GNSS-R over Sea Ice	Fabra et al. (2011b)
GNSS Reflectometry for the remote sensing of sea ice and dry snow	Fabra et al. (2011d)
GNSS-R for the Retrieval of Internal Layers' Information from Dry Snow Masses	Fabra et al. (2011c)
On the Retrieval of the Specular Reflection in GNSS Carrier Observations for Ocean Altimetry	Semmling et al. (2012)
Characterization of Dry-snow Sub-structure using GNSS Reflected Signals	Cardellach et al. (2012)
Sun reflections off Antarctica's snow sub-structural layers	In preparation for *Geophysical Research Letters*

Table 1.: List of publications arisen from the work presented in this dissertation.

2

BACKGROUND

This Chapter provides the general context of the present dissertation. Whereas Section 2.1 gives a basic description of the technique that will be further analyzed for remote sensing of the cryosphere (GNSS-R), a summary of other current approaches and instrumentation employed towards the same purpose (state of the art) is described in Section 2.2.

2.1 GNSS-R CONCEPT

Roughly speaking, the GNSS-R or PARIS concept consists in the use of signals transmitted from the GNSS satellites and reflected off different types of Earth's surfaces. Geophysical information is extracted from the changes suffered by these signals due to the reflection process. In spite of being initially conceived towards sea surface altimetry applications (by measuring the delay experienced by GPS signals through the reflected path), further research studies on the applicability of this technique for other remote sensing purposes have extended the GNSS-R concept to the more general definition previously given. Figure 2 illustrates the general scheme of a GNSS-R system. At a first glance, we can see the two main advantages of this approach compared with other satellite-based remote sensing techniques. The first one is the use of a well consolidated, calibrated and properly maintained constellation of transmitter satellites, therefore only the receiver units have to be deployed and built; working as passive instruments. This fact not only implies a saving in the economic budget, but also –and not less important– a saving in the power budget of the hypothetic GNSS-R satellite's architecture. The second advantage is related to the multiple footprints that appear over the surface as a consequence of having several transmitters available at the same time. Such property permits to obtain a swath with higher spatial resolution than the standard single-footprint instruments, therefore offering the possibility to study spatially and temporally variable phenomena like ocean mesoscale flows, wave and wind fields, and ocean/sea-ice interactions (Martín-Neira, 1993). These same advantages apply, in smaller magnitude, to other non-satellital GNSS-R systems, such as airborne or coastal-based systems. Moreover, GNSS-R might have a niche in highly restrictive platforms such as unmanned aerial vehicles (UAV).

The next subsections provide a general description of the different elements that constitute a GNSS-R system, including a GNSS's basic description, characterization of the signals employed, formulation of bistatic radar equation and electromagnetic models for signal scattering. Further references will be given for those readers interested on a more comprehensive description of the different topics, since the purpose here is just to emphasize those aspects that are relevant for the present study.

2.1.1 AN OVERVIEW OF THE GPS SYSTEM

The Global Positioning System (GPS) started to develop in 1973 by the Department of Defense (DoD) of the United States as an effort to overcome the limitations of previous navigation systems. After the launching of its first satellite in 1978, the system was declared operational in 1995 and constitutes the reference GNSS.

The positioning method employed by GPS is called *trilateration* and basically consist on estimating the receiver's location from the distance measurement of at least 4 different reference transmitters (GPS satellites). These distances, known as *pseudoranges*, are retrieved by the estimation of the time delays experienced by the transmitted signals until they reach the receiver. Therefore, we can imagine that the goodness of these delay estimations is an important factor to determine the accuracy of the positioning solution. They are called *pseudoranges* rather than ranges because in principle they might have accuracy errors in the time measurement.

In order to provide the proper visibility at any Earth's location and at any instant of time (four satellites are needed to solve a three-dimensional position plus a receiver clock bias), the original designed constellation was composed by a baseline of 24 satellites (GPS Space Segment) distributed in six orbital planes at an altitude of 20200 km, with each satellite making two complete orbits each sidereal day and repeating the same ground track afterwards. Under such conditions, it is estimated that about 99.99% of GPS users around the world would see six or more satellites (70% would see eight or more). Nowadays, there are up to 32 actively broadcasting GPS satellites, improving the full system's visibility and the precision of GPS receiver calculations by providing redundant measurements at different geometries.

Before entering in how the receiver determines the pseudoranges with respect to each visible satellite, it will be worth knowing how it learns their position. This information is broadcasted in real time by the GPS satellites in what is known as *Navigation Data Message*, which is carried by the GPS signal and transmitted at a rate of 50 bps. The whole message is composed by 25 frames of 1500 bits with a well defined format, taking then 12.5 minutes to be completely transmitted. The information contained for each transmitter satellite includes *clock corrections*, *satellite quality* index (marking an ad hoc degradation in the range accuracy), *ephemeris* (a tabulation of the satellite's position and velocity vectors), *ionospheric corrections*, *UTC correction* (UTC to GPS time offset) and *almanac* (a coarse version of the *ephemerides* of all satellites in the constellation). All these parameters are updated and uploaded to the transmitting satellites by the GPS Control

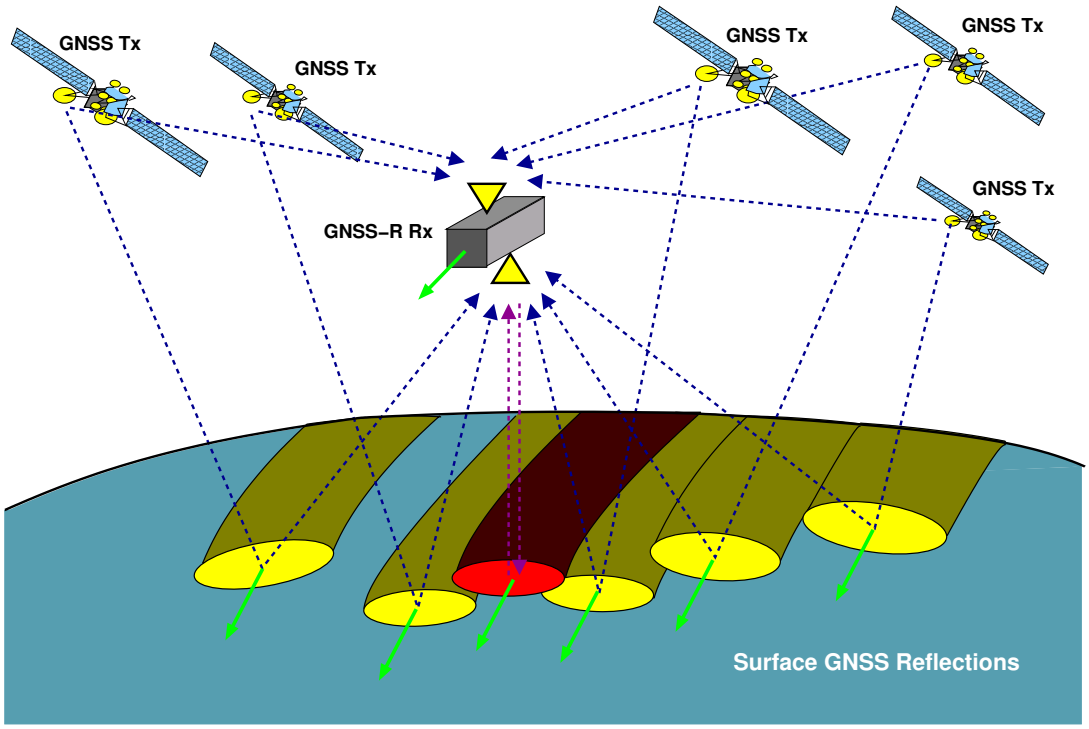

Figure 2.: Scheme of a typical GNSS-R system with several transmitters (yellow footprints) and comparison with a standard nadir-looking radar altimeter (red footprint). Up-looking and down-looking antennas are represented with yellow triangles. Green arrows mark the velocity vectors from the receiver and the surface footprints.

Segment, a set of Ground Stations that deal with the management of the satellite operations.

The methodology employed to determine pseudoranges and to let the receiver discern between signals coming from different satellites is based on the use of *ranging codes*. This multiple access technique, with several users (the GPS satellites would play the role of users in this definition) sharing the same time and frequency resources, is known as Code Division Multiple Access (CDMA) and is also used in other applications, such as the third generation of mobile communications (UMTS). In GPS, the ranging codes are a family of binary codes called pseudo-random noise (PRN) sequences, due to their similar spectral properties to actually random sequences, assigned to each satellite with a unique number in the range 1 through 32. The main characteristics of these codes are their good autocorrelation properties (maximum value obtained when aligned and a constant decay afterwards) and that they are nearly uncorrelated between them (orthogonal behavior). Therefore, the receiver only needs to correlate the GPS signal (in baseband and Doppler-corrected) against modeled replicas of these codes in order to distinguish among different satellites and to estimate the pseudorange value from the location of the correlation peak. The length and rate of a PRN code determine the acquisition and tracking characteristics of the signal in the presence of noise and interference.

Overall, the basic structure of a GPS signal consists of three components: a carrier RF sinusoidal signal ($f(t)$), a ranging code ($C(t)$) and the navigation data message ($D(t)$). This scheme is displayed in Figure 3. In order to provide different levels of service, the actual signal transmitted by each GPS satellite has two ranging codes: *coarse/acquisition* (C/A) with standard positioning service for peaceful civil use, and *precise* (encrypted) P(Y) for the DoD-authorized users. The C/A-code is a unique sequence of 1023 bits, called *chips* to differentiate them from the actual *bits* –a source of information– of the navigation data message, with a repetition period of 1 ms. The resultant chip-duration is $\sim 1\mu$s, or $\sim$ 300m in the space domain, with a chip-rate of 1.023 MHz. On the other hand, the P(Y)-code has a duration of 1 week ($\sim 10^{14}$ chips), with a chip-rate of 10.23 MHz and a chip-duration of $\sim$ 30m. One can guess that the better performance achieved by the P(Y)- with respect to the C/A-code is related to the order of magnitude of difference in their respective characteristics. In addition, the C/A-code was intentionally degraded in its origins ("selective availability" disabled 2000), thus increasing this difference. Note that both ranging codes have a rate significantly higher than the navigation data message (50 bps). The composite binary signal obtained from the combination of the latest with the C/A- or the P(Y)-code is then impressed upon the carrier in what in communications engineering is known as binary phase shift keying (BPSK) modulation.

Currently, each GPS satellite transmits continuously using –at least– two carrier frequencies in the L-band, known as Link 1 (L1) and Link 2 (L2):

$$f_{L1} = 1575.42\text{MHz} = 154 \times 10.23\text{MHz}$$
$$f_{L2} = 1227.60\text{MHz} = 120 \times 10.23\text{MHz}$$

By comparing these values with the C/A- and P(Y)- chip-rates, one can understand why the clock frequency of the atomic standards aboard the GPS satellites is 10.23 MHz.

Finally, the analytical expression for the L1 and L2 transmitted signals becomes:

$$s_{L1}(t) \quad = \quad \sqrt{2P_{C/A_{L1}}}C_{C/A}(t)D(t)\cos(2\pi f_{L1}t + \phi_{L1}) +$$

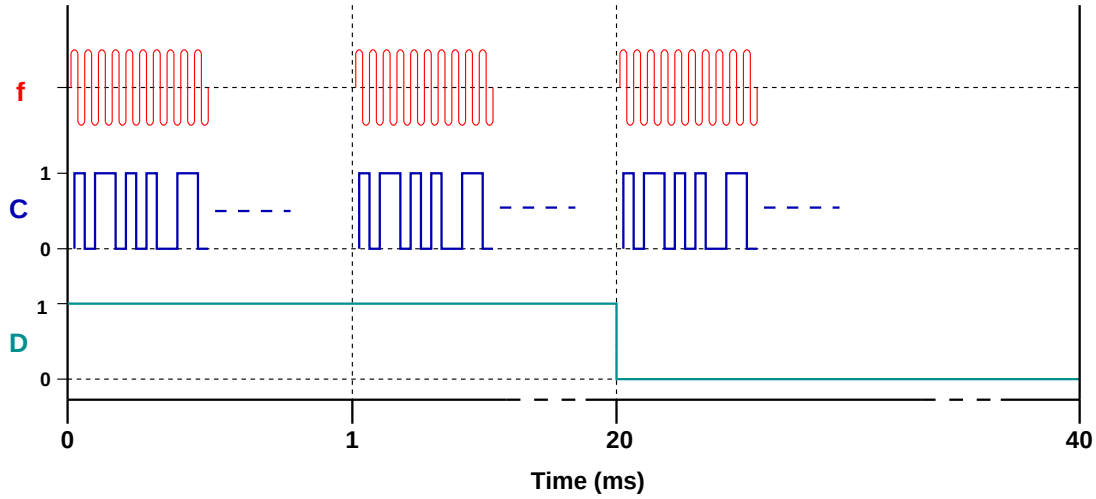

Figure 3.: Different components of a GPS L1 C/A signal: navigation data message (D), C/A-code (C) and carrier f_{L1} (f). The whole signal is obtained as $[D(t) \oplus C(t)] \otimes f(t)$, where $\oplus$ stands for a module 2 summation and $\otimes$ a biphase modulation.

$$
\begin{aligned}
& + \sqrt{2P_{P(Y)_{L1}}} C_{P(Y)}(t) D(t) \sin(2\pi f_{L1} t + \phi_{L1}) \qquad (1) \\
s_{L2}(t) \quad = \quad & \sqrt{2P_{P(Y)_{L2}}} C_{P(Y)}(t) D(t) \sin(2\pi f_{L2} t + \phi_{L2})
\end{aligned}
$$

where $P_{C/A_{L1}}$, $P_{P(Y)_{L1}}$ and $P_{P(Y)_{L2}}$ are the signal power for signals carrying C/A-code on L1, and P(Y)-codes on L1 and L2 respectively; $C_{C/A}$ and $C_{P(Y)}$ are the C/A- and P(Y)-code sequences assigned to the satellite; D is the navigation data message; f_{L1} and f_{L2} are the carrier frequencies corresponding to L1 and L2; and ϕ_{L1} and ϕ_{L2} are phase offsets.

From Equation (1) we can see that s_{L2} only transmits P(Y)-code. This is true for the older satellites currently in orbit and healthy, that belong to Blocks IIA and IIR and nowadays still represent a majority in the whole constellation (22 of 32). However, with the modernization made with Block IIR-M (8 satellites launched in 2005-2009), a civil code was added to L2 (known as L2C) in addition to the military-use-only M-code added to both L1 and L2. Moreover, the last update (Block IIF), with 2 satellites launched and another ready-to-launch in current year 2012, has planned to add a new L5 signal at the newly allocated frequency band centered at $f_{L5} = 1176.45$ MHz, for civil users interested in precise positioning (similar characteristics than P(Y)-code) and safety-of-life applications.

As a last comment, all the aspects compiled up to this point that briefly summarize the GPS system can be found and are deeper explained in references Misra and Enge (2006) and Spilker et al. (1996) (among others), which represent a comprehensive source of information for those readers interested in the GPS world. The next subsections provide more details about the signal employed in the present study (GPS L1 C/A) and a basic comparison of GPS with other GNSS in order to know if the results obtained using GPS reflections could be extrapolated to a more general context with several GNSS constellations.

2.1.1.1 *The GPS L1 C/A signal*

Most of GPS receivers designed for civilian applications only use the L1 C/A-code signal. The other contributions in the same frequency band (modulated with P(Y)- or even M-code also) are transparent to these instruments since, without the proper code replicas for cross-correlating them, they remain below the noise level. The dedicated GPS-R receiver employed in the experimental campaigns that are the core of this study and will be later introduced in Chapter 3 shares these characteristics.

We have seen that pseudoranges are estimated from the location of the peak of the cross-correlation between the received signal and its modeled replica. We thus need to know the characteristics of the C/A-code's auto-correlation. As stated before, this code is a sequence of 1023 chips at a rate of 1.023 MHz. The chip-duration or chip-width is $\tau_{C/A} = 1/1.023\text{MHz} \approx 1\mu s$ or $\sim$ 300m in the space domain. The type of codes employed are known as *Gold* sequences and are mathematically designed to have an auto-correlation function with maximum at $\Delta t = 0$ and linear decay until $\Delta t = \pm\tau_{C/A}$, keeping then low values until the next period, as illustrated in Figure 4. The same representation shows some sidelobes, whose strongest values are always at least -24dB relative to the main auto-correlation peak. Therefore, the primary observable to analyze in a common civilian GPS receiver would basically be a triangular-shape amplitude function with a base-width of $\sim 2\tau_{C/A}$. The methodology further employed towards positioning purposes is out of the scope of this work.

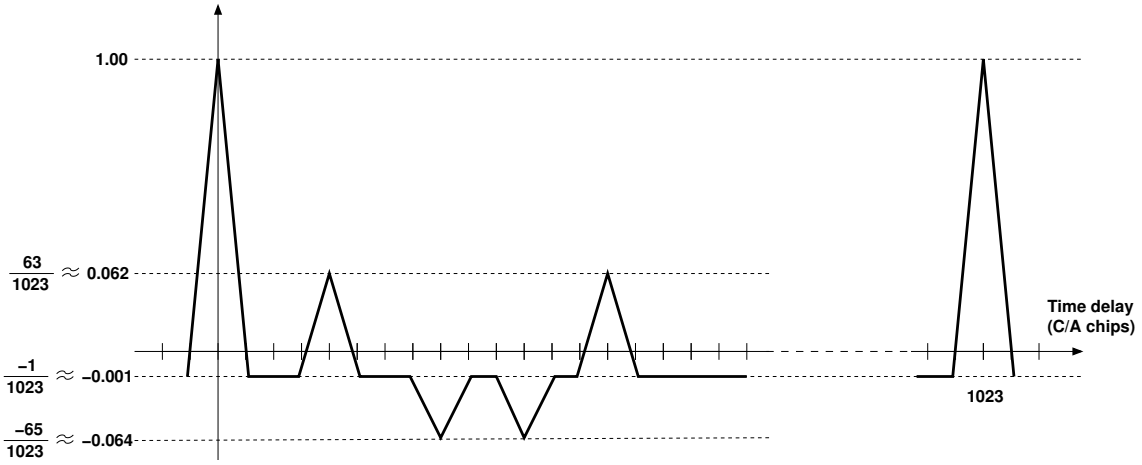

Figure 4.: Non-scaled example of the auto-correlation function of the C/A-code. The function only takes the four value levels shown and more sidelobes appear until chip #1023.

Regarding its spectral properties, the GPS L1 C/A signal spectrum's can be approximated by a sinc function with a main lobe of bandwidth $B_{C/A} = 2.046$ MHz (between the first nulls) and centered at the carrier f_{L1}, produced by the chip transitions (rectangular pulses) of the C/A-code. In fact, this sinc-shape spectrum is internally constituted by a train of δ-pulses with frequency steps of 1 kHz due to the C/A-code's periodicity, which in turn are convolutioned against the spectrum of the navigation data message, another sinc function with a bandwidth of 50 Hz. The contributing effects of the different components of the GPS L1 C/A signal on its spectrum are illustrated on Figure 5. On the

other hand, Figure 6 shows a comparison between the spectrum of the different signals transmitted by the newest GPS satellites (Block IIF).

Finally, about their more general electromagnetic characteristics, the GPS signals are transmitted in right-hand circular polarization (RHCP), with an ellipticity (semi-axis ratio) better than 1.2 dB for L1, and 3.2 dB for L2 above the Earth surface. The minimum received power on ground is -158.5 dBW for L1 C/A, +3 dB than the P(Y)-code in the same band. The other GPS civil signals have these levels at -160.0 dBW (L2C) and -154.9 dBW (L5). The different power loss due to the different path ray length and atmospheric absorption corresponding to different elevation angles is compensated through the shape of the transmitter antenna gain-pattern.

2.1.1.2 *Comparison with other GNSS*

Among the different GNSS initiatives, probably the most potential GPS *competitors* are GLONASS and future Galileo and BeiDou-2/Compass. A summary of the orbital characteristics of the three systems is shown in Table 2, while their frequency allocations at L-band are displayed in Figure 7.

GNSS	**GPS**	**GLONASS**	**Galileo**	**BeiDou-2 Compass***
Number of satellites (operational/designed)	32/24	24/24	0/27	4/27
Number of orbital planes	6	3	3	3
Inclination (deg)	55	65.8	56	55
Radius (km)	26562	25510	29994	27878
Period (hh:mm)	11:58	11:16	14:04	12:53
Ground track repeat (days)	1	8	10	-

Table 2.: Orbital characteristics of GPS, GLONASS, Galileo and BeiDou-2/Compass. * Only MEO satellites are considered here.

GLONASS (Global'naya Navigatsionnaya Sputnikovaya Sistema) is the GNSS that the Soviet Union started to develop in 1976, achieving their full orbital constellation of 24 satellites in 1995. From 2003 to 2011, under the Russian Federal Space Agency's control, the system has been completely replaced by a second generation of satellites (GLONASS-M) and one space vehicle of the third generation (GLONASS-K) is already in orbit. GLONASS has many similarities with GPS in terms of system architecture, origin as a military system, and even the terminology: C/A-code, P-code and two types of service (standard and precise). Moreover, the system was originally designed to work in two frequency bands (G1 and G2, contiguous to their equivalents L1 and L2 in GPS), using both codes in G1 and only the P-code in G2 (a civil signal has been also added to G2 with GLONASS-M and beyond). The main difference with GPS relies on the use of a frequency division multiple access (FDMA) technique instead of CDMA, dividing G1 and G2 bands into 14 RF channels of 0.5625 MHz and 0.4375 MHz spacing respectively. The 24 satellites get by with 14 channels by assigning the same channel to satellites on the opposite sides of the Earth. Then, a single pair of C/A and P codes are employed by all the transmitters, with rates of 0.511 MHz and 5.11 MHz respectively. In spite of that,

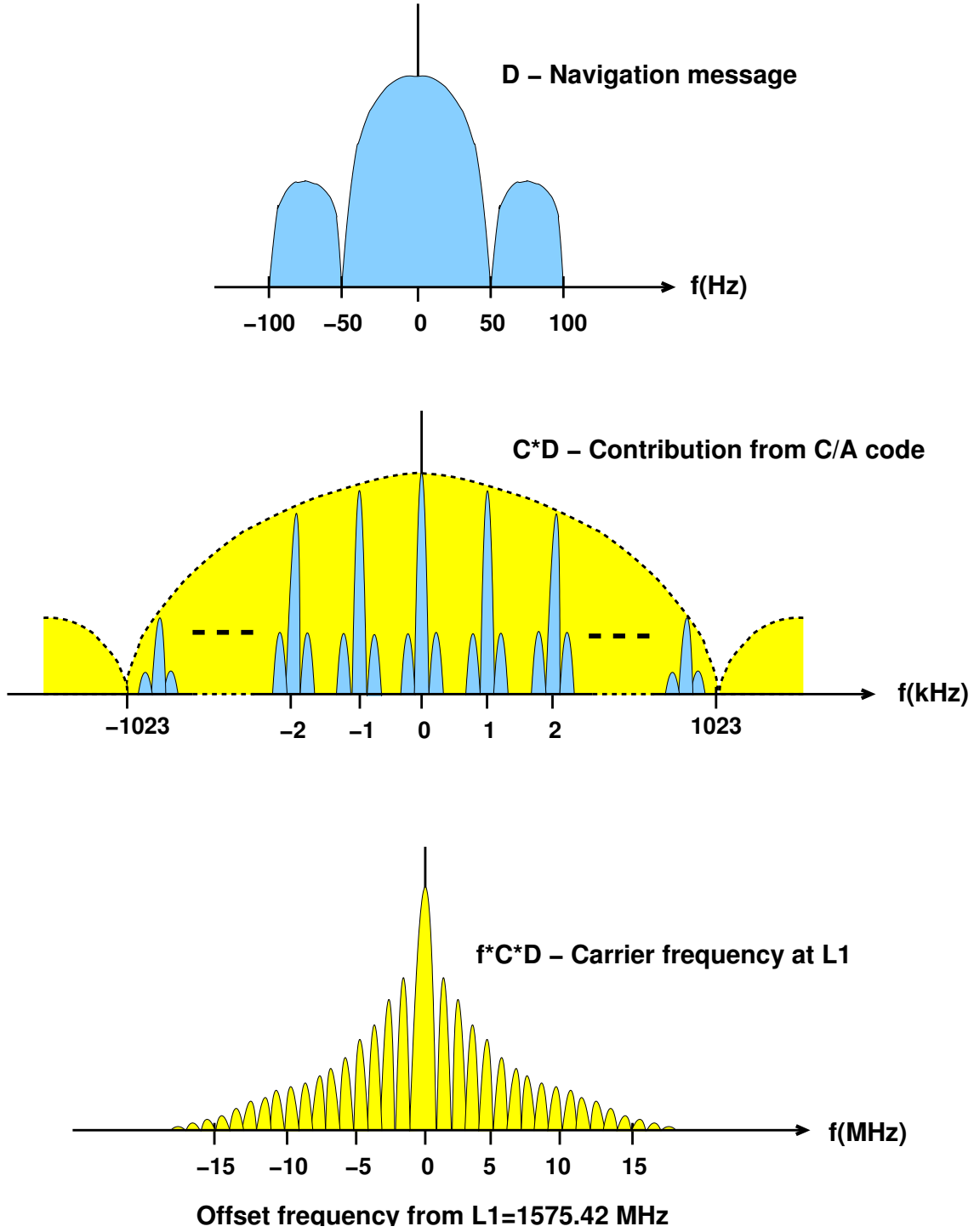

Figure 5.: Up to bottom: Contributing effects of the different components of the GPS L1 C/A signal (navigation data message, C/A-code and carrier f_{L1}) on its spectrum.

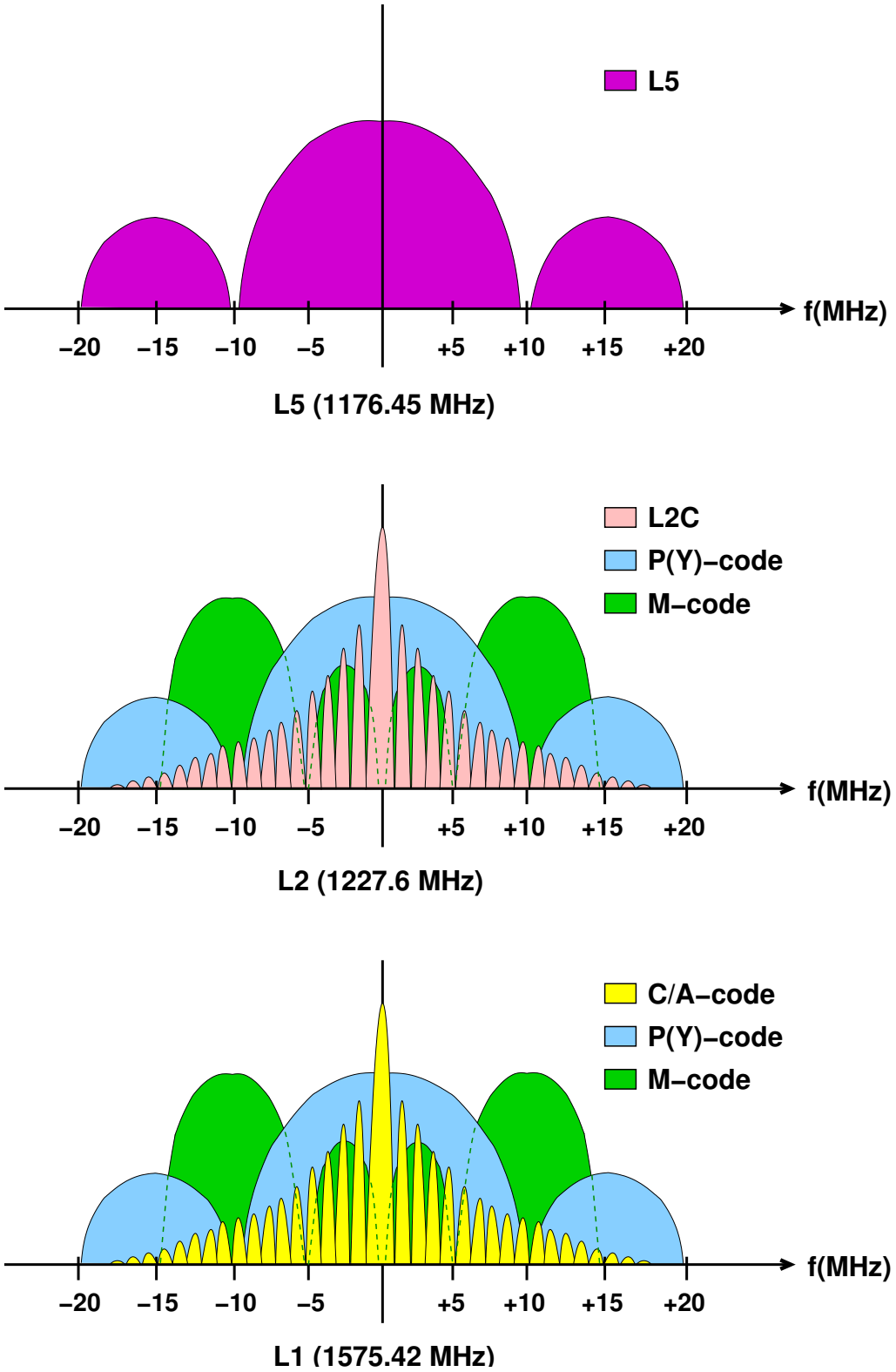

Figure 6.: Spectrum of the GPS signals transmitted by the newest satellites (Block IIF). Satellites from Block IIR-M do not transmit in L5 band and the rest of them (Blocks IIA and IIR) do not either transmit L2C and M-codes.

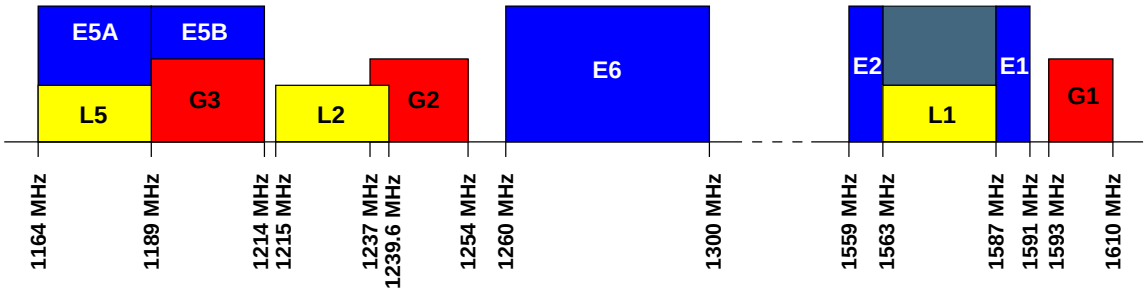

Figure 7.: Frequency allocations for GPS (yellow), GLONASS (red), Galileo and BeiDou-2/Compass (blue) at L-band. The GLONASS' frequency bands are often represented "L#", but here are referred as "G#" to distinguish them from the GPS bands.

Signal	**E5A**	**E5B**	**E6P**	**E6C**	**L1P**	**L1F**
Modulation	BPSK	BPSK	BOC	BPSK	BOC	BOC
Chipping rate	10.23	10.23	5.115	5.115	2.557	1.023
Frequency band	E5A	E5B	E6	E6	E2-L1-E1	E2-L1-E1
Service	Open	Open	Fee-based	Fee-based	Fee-based	Open

Table 3.: Basic characteristics of planned Galileo signals. Chipping rate in Mcps.

there are plans for adding also signals based on CDMA in different frequency bands (G3) with GLONASS-K (Urlichich et al., 2011).

Galileo, a joint initiative of the European Union and the European Space Agency with the participation and investment of other international partners, is planned to be the first civilian commercial GNSS. It means that, in addition to the standard positioning services freely available, there will be enhanced capabilities, including high precision, integrity, service-availability, and robustness against interferences, offered for paying commercial users and *trusted* government agencies (law enforcement, national security, emergency services or military applications) as fee-based services. As a distinctive feature, Galileo will provide a unique global search-and-rescue function, consisting on relying distress signals from users towards the ground segment stations (in contact with rescue coordination centres) by means of onboard transponders and dedicated UHF channels, providing at the same time feedback acknowledgments to these users. With 4 In-Orbit Validation (IOV) space vehicles already launched, the full completion of the 30 satellites' constellation (27 operational + 3 active spares) is expected by 2019 (ESA, 2013; EC, 2013). Galileo navigation signals are to be transmitted in four frequency bands (E5A, E5B, E6 and E2-L1-E1) using CDMA technique. Six types of signals (characterized in Table 3) are planned, some of them modulated with the *newer* binary offset carrier (BOC) method, which splits the spectrum in two parts in order to reduce the interference with a BPSK-modulated signal in the same frequency band (note the GPS-compatibility purpose here).

BeiDou-2/Compass is the Chinese contribution to the GNSS *world*. The Government started its development from the experience acquired with BeiDou-1, an experimental regional navigation system consisting of 3 operational satellites (plus 1 spare). This system has been offering navigation services, mainly for customers in China and neighboring regions, since 2000. The BeiDou-2/Compass Space Segment will consist of a constellation of 35 satellites, which include 5 Geostationary Orbit (GEO) satellites; 3 in Inclined Geosynchronous Orbit (IGSO); and 27 in Medium Earth Orbit (MEO), whose orbital pa-

Signal	**B1(I)**	**B1(Q)**	**B2(I)**	**B2(Q)**	**B3**
Modulation	QPSK	QPSK	QPSK	QPSK	QPSK
Chipping rate	2.046	2.046	2.046	10.23	10.23
Frequency band	E2	E2	E5B	E5B	E6
Service	Open	Authorized	Open	Authorized	Authorized

Table 4.: Basic characteristics of BeiDou-2/Compass transmitted signals. Chipping rate in Mcps.

rameters are listed in Table 2. During 2012, 5 additional satellites were launched increasing to 14 (5 GEO, 5 IGO and 4 MEO) the number of satellites of the constellation, which is expected to be completed and provide global navigation services by 2020 (BeiDou, 2013). The ranging signals are based also on the CDMA principle and have complex structure similar to Galileo or modernized GPS. Like in the other GNSS, there will be two levels of positioning service: open and restricted (military). Frequencies for BeiDou-2/Compass are allocated in four bands: E1 (not yet employed), E2, E5B, and E6; overlapping with Galileo. Table 4 provides the main characteristics of currently transmitted signals.

Finally, with respect to compatibility and interoperability of GPS, GLONASS, Galileo and BeiDou-2/Compass, the first condition is achieved with the use of orthogonal frequency bands (GLONASS) or smart modulation approaches when sharing the same frequency resources (BOC in Galileo). About the second aspect, it is required that transformations between their coordinate frames and time scales to be known. However, current GPS + GLONASS receivers have already dealt with this issue. It is expected an improvement in real-time positioning accuracy from the combined use of GNSS systems in the near future, as well as in terms of robustness and integrity of service. Therefore, regarding GPS-R to GNSS-R extrapolation, there is no reason for expecting major troubles (it is less restrictive than positioning interoperability), and the potential benefits are the increase of the number of transmitter satellites and the modernization of the signal structures (with new high chip-rate civil codes available and higher transmitted powers).

2.1.2 RADAR FUNDAMENTALS

Essentially, a radar system (derived from **ra**dio **d**etection **a**nd **r**anging) consists of a transmitting source of electromagnetic energy radiated towards a given target, and a receiver that collects the energy that bounces off from it. Therefore, the GNSS-R concept could be visualized as an standard radar system that employs the signals transmitted by the navigation satellites for remote sensing purposes. Such configuration, where transmitter and receiver are placed at different locations, is usually referred as *bistatic radar* or even *multi-static radar*, when multiple transmitters can be employed at the same time by a single receiver (as in the GNSS-R case displayed in Figure 2).

The expression that relates the power delivered by the transmitter with the signal-to-noise ratio (SNR) at the detector after interaction with a single point target is usually known as **radar equation**, and for the bistatic geometry is given by:

$$SNR = \frac{P_r}{KTB} = \left(\frac{P_t G_t}{4\pi R_1^2}\right) \sigma_b \left(\frac{A_{eff}}{4\pi R_2^2}\right) \frac{1}{L} \left(\frac{1}{KTB}\right) = \frac{P_t G_t \sigma_b G_r \lambda^2}{(4\pi)^3 R_1^2 R_2^2 L K T B} \tag{2}$$

where:

- P_r = Power sensed by the receiver antenna
- P_t = Power transmitted
- G_t = Transmitter antenna gain (directivity)
- R_1 = Distance from transmitter to target
- σ_b = Bistatic radar cross-section
- A_{eff} = Effective area of receiver antenna
- R_2 = Distance from target to receiver
- L = Non-modeled losses (e.g. atmospheric loss)
- K = Boltzmann's constant
- T = Receiver temperature (antenna + thermal noise)
- B = Receiver bandwidth
- G_r = Receiver antenna gain (directivity)
- λ = Signal wavelength

While the right end side of Equation (2) represents a more compact expression, the central part clusters the terms into groups (in brackets) sequentially ordered to illustrate where they come from: first group provides the power density at the target; secondly, by definition, σ_b is the ratio between the power re-radiated by the target towards the receiver and the power density at its location, which in spite of having dimensions of area, depends on several aspects of the target (e.g. geometric area, dielectric characteristics, roughness); the third group then transforms the power re-radiated by the target into the power sensed at the receiver antenna; finally, L accounts for non-modeled losses, such as atmospheric loss or polarization decoupling, and the last group gives the noise power (inverted).

The previous expression would be valid for the simplest case of bistatic radar, where the transmitted signal is a rectangular pulse of duration τ_0 seconds (known as pulsed radar). Under such characteristics, the optimal receiver bandwidth is given by $B = 1/\tau_0$ (compression factor of 1). Therefore, assuming that the single point target does not modify its original shape, the resultant signal at the output of the receiver filter can be approximated by a triangular pulse with a width at the base of $2\tau_0$ (a convolution between two rectangular pulses of duration τ_0). Then, in order to be able for the radar to distinguish the response from two different targets, the relative delay of arrival among them has to be bigger than τ_0 (in this academic case). By converting this term into the spatial domain (by multiplying it by the speed of light), we can obtain what in radar terminology is known as *range resolution*, a key parameter that defines the performance of this type of systems.

A proper way to enhance SNR and range resolution in a radar system is achieved by modulating the transmitted pulses in phase or frequency. This signal processing technique is usually referred as *pulse compression* and basically consists in improving the autocorrelation properties of the transmitted signal. In order to maximize the SNR, the

optimal filter at the receiver is determined by the transmitted signal's baseband equivalent (matched filter (North, 1963)), so the output of such filter can be computed as the cross-correlation of the received signal against a clean replica of the transmitted signal (both in baseband). Among the different approaches used for pulse compression available in the literature, the most typical ones are based on linear frequency modulation, or *chirping*, and phase modulation by means of Barker and Frank codes. The election of the proper technique will depend on the capabilities required (e.g. high compression factor, low complexity, robustness against frequency changes due to Doppler effect...). All these pulse-compression modulations are characterized by what is known as Woodward Ambiguity Function (WAF) (Woodward, 1953) χ, which is defined as:

$$\chi(\tau,\kappa) = \int_{-\infty}^{\infty} s(t)s^*(t-\tau)e^{-i2\pi\kappa t}dt \tag{3}$$

where $s(t)$ is the transmitted complex pulse at baseband (already modulated). Basically, the function χ is a a two-dimensional function of time delay τ and Doppler frequency κ showing the distortion of a returned pulse due to the receiver matched filter and affected by a Doppler shift induced by a moving target, based only on the properties of $s(t)$.

Finally, in order to obtain a more realistic expression of the radar equation, it is important to take into account that typical targets are morphologically more complex than a single point. Therefore, the effect of the bistatic radar cross section in Equation (2) has to be integrated along the reflecting surface (i.e. the section of the surface that re-radiates towards the receiver) of the target, as a results of multiple scattered contributions ($\sigma_b \Rightarrow \sigma^0_{pq}(\vec{r})$). Then, considering a volumetric target with a given surface ($surf$) interface off which the signal rebounds, and the use of a pulse compression technique characterized by its WAF function χ, we can convert Equation (2) into a more general expression:

$$SNR(\tau,\kappa) = \frac{P_t\lambda^2}{(4\pi)^3 LKTB}\int_{surf}\frac{G_t(\vec{r})G_r(\vec{r})\sigma^0_{pq}(\vec{r})}{R_1^2(\vec{r})R_2^2(\vec{r})}\chi^2\left[\tau+\delta\tau(\vec{r}),\kappa+\delta\kappa(\vec{r})\right]d^2r \tag{4}$$

which displays the SNR corresponding to selected delay (τ) and frequency (κ) offsets as the contribution from the scattering points $\vec{r}$ along the target's reflecting surface.

2.1.2.1 *Radar equation using GPS L1 C/A signal*

The modulation produced by the C/A-code behaves like a radar pulse compression technique (see autocorrelation of C/A-code in Figure 4), as deduced from the characteristics of the GPS L1 C/A signals given in Section 2.1.1.1. Then, to adapt Equation (4) into a GNSS-R scenario employing GPS L1 C/A signals is nearly straightforward, since it simply requires to compute the function χ for the C/A-code. Note that the phase variations produced by the navigation data message (D in Equation (1)) are not accounted because they have a rather longer period than the typical integration time T_i of 1 msec. On the other hand, the effect of the P(Y)-code signal (sharing L1 band) can be neglected due to the cross-correlation properties of this type of sequences.

As done by Zavorotny and Voronovich (2000), we will assume a simple approximation for the computation of $\chi_{C/A}(\tau,\kappa)$ based on its analytical behavior along the temporal and

frequency axes. For the temporal case, we obtain the autocorrelation of the C/A-code already shown in Figure 4:

$$\begin{aligned}\Lambda_{C/A}(\tau) \equiv \chi_{C/A}(\tau,0) &= \frac{1}{T_i}\int_0^{T_i} C_{C/A}(t)C^*_{C/A}(t-\tau)dt \\ &\approx \begin{cases} 1-|\tau|/\tau_{\mathrm{C/A}} & \text{for } |\tau| < \tau_{\mathrm{C/A}} \\ 0 & \text{otherwise} \end{cases}\end{aligned} \tag{5}$$

where $C_{C/A}(t)$ is a given C/A-code sequence in order to keep the same notation as in Equation (1). Note that the integral limits from Equation (3) have been replaced by its normalized limited-duration equivalent (with integration time T_i), and the last approximation is valid given that $T_i \gg \tau_{\mathrm{C/A}}$.

Given that $C_{C/A}(t)$ is a binary sequence, then $C^2_{C/A}(t) = 1$ and $\chi_{C/A}(\tau,\kappa)$ can be easily resolved along the frequency axis:

$$S_{C/A}(\kappa) \equiv \chi_{C/A}(0,\kappa) = \frac{1}{T_i}\int_0^{T_i} e^{-i2\pi\kappa t}dt = \frac{\sin(\pi\kappa T_i)}{\pi\kappa T_i}e^{-i\pi\kappa T_i} \tag{6}$$

whose absolute amplitude would result in a |sinc| function with maximum at $\kappa = 0$ and zeros at each multiple of $1/T_i$.

Finally, $\chi_{C/A}(\tau,\kappa)$ is approximated by the following factorized form:

$$\chi_{C/A}(\tau,\kappa) \approx \Lambda_{C/A}(\tau)S_{C/A}(\kappa) \tag{7}$$

which properly describes the behavior of this function around its maximal values.

As a last comment, note that the expressions obtained here would be also valid for any binary pseudo-random sequence (replacing $\tau_{\mathrm{C/A}}$ in Equation (5) by a given $\tau_{\mathrm{chip}} \ll T_i$) phase-modulating the transmitted signal.

2.1.3 SCATTERING MODEL: KIRCHHOFF APPROXIMATION UNDER GEOMETRIC OPTICS OVER A GAUSSIAN SURFACE

Section 2.1.2 has shown a first step to characterize the *SNR* obtained in a GPS-based radar. The target in a standard GNSS-R architecture corresponds to an area over the Earth surface whose limits are imposed, at least, by the smallest antenna footprint of the radar system (we will see later how this area is typically reduced due to other factors). The goal of the present section is then to provide a simple expression for the bistatic radar cross-section of the reflecting surface, σ^0_{pq}, in order to later obtain a manageable formulation of the radar equation presented in previous Section 2.1.2 and applicable to GNSS-R. Given that it is not the purpose of this study to develop sophisticated electromagnetic models for signal scattering, the analysis will be based on the well-known Kirchhoff approximation under Geometric Optics (KGO) applied over a surface with a Gaussian height probability distribution. This approach has been widely used for different applications, including GNSS-R techniques (Zavorotny and Voronovich, 2000; Belmonte et al., 2009; Cardellach et al., 2003; Lowe et al., 2002a). The main advantage of the KGO is its simplicity, since it describes the surface cross-section from the dielectric properties of the medium and a single statistical roughness parameter, the mean square slope (*MSS*). Until the end of this section, just a few hints of the process for obtaining σ^0_{pq} will be pointed

out to remark the approximations and assumptions needed. For those readers interested in the intermediate steps behind, the whole process is comprehensively described in Cardellach (2002) (a similar analysis can be found in Zavorotny and Voronovich (2000) and Belmonte-Rivas (2007)).

The scattering coefficient σ^0_{pq} is, by definition, the ratio between the scattered power per unit area and the incident power density:

$$\sigma^0_{pq} = \frac{\mathcal{R}e\left\{\frac{<||\vec{E}^s_{pq}||^2>}{\nu}\right\}/A_0}{\mathcal{R}e\left\{\frac{E_0^2}{\nu^*}\right\}/4\pi R_0^2} \tag{8}$$

where $\vec{E}^s_{pq}$ is the scattered field in the pq polarization state; E_0 is the maximum amplitude of the incident field; ν is the intrinsic impedance of the medium; A_0 is the illuminated area and R_0 the distance from the point of observation (typically the receiver) to the center of A_0.

The first step consists on obtaining an expression for the scattered field. For doing so, the Kirchhoff method (KM) is based on the vector second Green's theorem, computing then the scattered field only from the field components tangential to the reflecting surface. As a result, the total scattered field at any point on the surface is calculated as if an incident wave was striking an infinite plane (or facet) tangent to the point. Therefore, the application of such method is restricted to surfaces with large undulations in terms of λ (a surface approximated by a combination of several and superimposed big plane facets).

The next simplifying assumption made is known as *Stationary-Phase* approximation or *Geometric Optics*, which particularizes the KGO from the more general KM. The reason behind this second terminology is the consideration that only those facets from the reflecting surface that allow local specular reflection will contribute to the scattered field, thus excluding local diffraction effects. The resultant expression for the scattered field is given by:

$$\vec{E}^s_{pq} = \frac{-ike^{-i(kR_0-\omega t)}}{4\pi R_0}\Re_{pq}E_0\int e^{ik\vec{q}\cdot\vec{r}'}d^2r' \tag{9}$$

where k is the wavenumber; ω is the angular frequency; $\Re_{pq}$ is the local Fresnel coefficient; $\vec{q}$ is the scattering vector, which is defined as $\vec{q} \equiv k(\hat{n}_s - \hat{n}_i)$ (being $\hat{n}_{s,i}$ the unitary scattered and incident vectors) and is perpendicular to the local tangent plane due to the approximations made; and $\vec{r}'$ is the spatial vector under integration across the reflecting surface.

Finally, the evaluation of the scattering cross-section coefficient in Equation (8) requires the computation of $< \vec{E}^s_{pq} \cdot \vec{E}^{s*}_{pq} >$. By defining the integral factor in Equation (9) as I, we can see that the major complexity of this computation lies on the resolution of $< ||I||^2 >$. A statistical description of the surface is required to continue from this point. The assumption made here is to consider a two-dimensional Gaussian height distribution of zero mean ($< z(x,y) >= 0$) and variance σ_h^2, with a given transversal autocorrelation function $\varrho(x_{corr}, y_{corr})$ and under isotropic conditions (i.e. rotational invariance of statistics). A further approximation is needed, consisting on neglecting those cases where the condition $(q_z\sigma_h)^2 \gg 1$ is not met (a large Rayleigh parameter is required). During

the process, the variance of the surface slopes (i.e. the one-dimensional mean square slope, *mss*) is taken, which is determined by the second derivative of the autocorrelation function evaluated at the origin (Belmonte-Rivas, 2007):

$$mss = -\frac{\partial^2 \varrho(r_{corr})}{\partial r_{corr}^2}\bigg|_{r_{corr}=0} \tag{10}$$

Note that the variables (x_{corr}, y_{corr}) from ϱ have been replaced by:

$$r_{corr} = \sqrt{x_{corr}^2 + y_{corr}^2} \tag{11}$$

due to the isotropic conditions assumed.

In addition, for Gaussian correlated surfaces, *mss* is related to the transversal correlation length of the surface, L_{corr}, by means of (Belmonte-Rivas, 2007):

$$mss = 2(\sigma_h / L_{corr})^2 \tag{12}$$

It is important to mention here that during the data analysis made in the present study, instead of *mss*, we will use the two-dimensional mean square slope (or simply referred as mean square slope), *MSS*, which for Gaussian correlated surfaces is computed as (Belmonte-Rivas, 2007):

$$MSS = 2\ mss \tag{13}$$

The expression finally obtained for the scattering cross-section coefficient is given by:

$$\sigma_{pq}^0 = \pi |\Re_{pq}|^2 \left(\frac{q}{q_z}\right)^4 P\left(-\frac{\vec{q}_\perp}{q_z}\right) \tag{14}$$

where $\vec{q}_\perp = (q_x, q_y)$ and P is the Probability Density Function of the surface slopes for a Gaussian isotropic surface spectrum:

$$P\left(-\frac{\vec{q}_\perp}{q_z}\right) = \frac{1}{2\pi\ mss} e^{-\frac{(q_\perp/q_z)^2}{2mss}} \tag{15}$$

Therefore, we can see how, in addition to the other geometrical and dielectric aspects, σ_{pq}^0 depends on the probability of the reflecting surface to have facets oriented in such a way that a mirror-like reflection would forward the field to the receiver.

As a last comment, the approximations made under the KGO approach limit its domain of applicability. Basically, they reduce the KM's domain with the restriction imposed by the requirement of a large Rayleigh parameter ($(q_z\sigma_h)^2 \gg 1$), which implies that in case of smooth surfaces (low σ_h^2), only nadir incidences (high q_z^2) can be applied. There are different approaches that cover other domains or even that overcome further limitations. While the Kirchhoff method (the generalization of the KGO) describes well near-specular scattering from smooth and large slopes (large-scale roughness), the Small Perturbation Method (SPM) covers non-specular mechanisms, such as diffraction and Bragg resonance, scattering from a small-scale roughness surface. Their combination, known as Two-Scale Composite Model (2SCM), adds both contributions, but is is inaccurate for grazing angles (as their predecessors). Another strategy that covers both regimes is the Small Slope Approximation (SSA) (Voronovich, 1985), which is valid for arbitrary

values of surface roughness height. However, all these methods require a more comprehensive description of the reflecting surface (e.g. the full autocorrelation function) and high computational cost to run their implementation. The large amount of data acquired during the experimental campaigns analyzed in the present dissertation and the lack of a proper in-situ surface and dielectrical characterization, imposed the application of the KGO.

2.1.3.1 *Dielectric and roughness aspects of different types of reflecting surfaces at L-band*

From the expression for the scattering cross-section obtained by the KGO approach given in Equation (14), we can see that, for a given geometry, σ^0_{pq} basically depends on a Fresnel component ($\Re_{pq}$) and a roughness factor (MSS). Considering the use of GPS signals, which are transmitted in RHCP (Section 2.1.1), we will focus the computation of $\Re_{pq}$ to the case of circular polarizations:

$$\Re_{co} = \Re_{RR} = \Re_{LL} = \frac{1}{2}(\Re_{VV} + \Re_{HH}) \tag{16}$$

$$\Re_{cross} = \Re_{RL} = \Re_{RL} = \frac{1}{2}(\Re_{VV} - \Re_{HH}) \tag{17}$$

where

$$\Re_{VV} = \frac{\epsilon\cos\theta - \sqrt{\epsilon - \sin^2\theta}}{\epsilon\cos\theta + \sqrt{\epsilon - \sin^2\theta}} \tag{18}$$

$$\Re_{HH} = \frac{\cos\theta - \sqrt{\epsilon - \sin^2\theta}}{\cos\theta + \sqrt{\epsilon - \sin^2\theta}} \tag{19}$$

and ϵ is the complex relative permittivity of the reflecting medium, and θ is the local incidence angle. Equations 18 and 19 are valid when considering the air as the propagation medium ($\epsilon_{air} = 1$). Therefore, according to the assumptions taken (Gaussian isotropic surfaces within the KGO domain), the reflecting surface can be then characterized by just two factors (ϵ and MSS). Let's see below several aspects and the expected range of values of these two terms for the different types of surfaces (reflecting media) which are relevant to the present study: sea water, sea ice, and dry/wet snow masses.

The relative permittivity ($\epsilon = \epsilon' + i\epsilon''$) is a complex number that characterizes the electrical properties of the media. This parameter basically depends on the internal components of the medium and their distribution, and it is a function of the electromagnetic wavelength. The real part of ϵ is referred as *dielectric constant* and is related to the speed of propagation, whereas the imaginary part (ϵ'') is named *dielectric loss factor* and controls the rate of attenuation of electromagnetic energy flow. Theoretical models are available in the literature to estimate ϵ for some of the cases studied here for remote sensing of the cryosphere. Most of the expressions and considerations given from this point are extracted from Ulaby et al. (1990a).

In spite of not being part of the cryosphere, it is important to know the dielectric properties of **sea water** due to their continuous interaction with the former. Typical L-band values of ϵ'_{sw} range from 70 to 80, and from 30 to 60 for ϵ''_{sw}. These values are computed from the water temperature and its salinity content.

The case of **sea ice** is rather complicated. By being a heterogeneous mixture of liquid brine (water with high salinity content) and air bubbles within a pure ice medium, the relative permittivity of sea ice (ϵ_{si}) depends on the dielectric properties, concentration, shape and orientation of each of its components. Most of these characteristics are governed by the growth rate of the ice layer, so different values of ϵ_{si} can be obtained depending on its stage of development. We will consider four main categories of sea ice on the basis of age: *new ice*, with thickness below 10 cm; *young ice*, up to 30 cm thick; *first-year ice*, whose thickness usually is between 30 cm and 2 m; and *multi-year ice*, usually exceeding 2 m of thickness. Further subdivisions and classifications can be found in WMO (1989). Numerical expressions obtained from real measurements at 1 GHz and valid for the thicker types of sea ice (first- and multi-year ice), are given (Hallikainen and Winebrenner, 1992) by:

$$\epsilon'_{si} = 3.12 + 0.009\, V_b \tag{20}$$

$$\epsilon''_{si} = 0.04 + 0.005\, V_b \tag{21}$$

where V_b is the relative brine volume (in ‰) and $V_b \leq 70‰$. On the other hand, new and young sea ice are characterized by a high-fractional brine volume and an effective dielectric constant that, while considerably smaller than that for sea water, is large compared with the results obtained for thicker categories (Hallikainen and Winebrenner, 1992). In absence of a consolidated model, we will take the average $|\epsilon_{si}| = 10$ measured in Belmonte et al. (2009) at L-band (actually using GPS-R at L1) over this type of sea ice as a reference value.

Another important component of the cryosphere lies in the form of **dry snow**, as in the case of the extensive snow accumulations located in the Antarctic Plateau. The term *dry* denotes the total absence of liquid water, thus persistent low temperatures (below the freezing mark) are required for the formation and conservation of this type of snow. Regarding its dielectric properties, ϵ_{ds} can be computed as a function of the relative permittivity of pure ice (ϵ_{ice}) and the volume fraction of ice in the mixture (ν_i):

$$\epsilon'_{ds} = (1 + 0.47\,\nu_i)^3 \tag{22}$$

$$\epsilon''_{ds} = 3\,\nu_i\,\epsilon''_{ice}\frac{\epsilon'^2_{ds}(2\epsilon'_{ds}+1)}{(\epsilon'_{ice}+2\epsilon'_{ds})(\epsilon'_{ice}+2\epsilon'^2_{ds})} \tag{23}$$

where $\epsilon'_{ice} = 2.95$, $\epsilon''_{ice} = 0.001$ and the volume fraction ν_i is related to the snow density (ρ_s) through $\nu_i = \rho_s/0.916$ (0.916 gr/cm^3 is the density of pure ice). However, when the temperature is in the proximity of 0°C, as in the case of warm seasons in coastal Polar environments, snow can support water in liquid form. This type of snow mixture is usually referred as **wet snow**, and its dielectric properties are strongly affected by the presence of liquid water, with high relative permittivity. In this case, ϵ_{ws} can be computed as (Fung, 1994):

$$\epsilon'_{ws} = (1.0 + 1.83\rho_s + 0.02 m_v^{1.015}) + \frac{0.073\, m_v^{1.31}}{1 + (f/f_0)^2} \tag{24}$$

$$\epsilon''_{ws} = \frac{0.073(f/f_0) m_v^{1.31}}{1 + (f/f_0)^2} \tag{25}$$

where m_v is the volume fraction of liquid water in the snow mixture, ρ_s is the snow density, f is the electromagnetic frequency and $f_0 = 9.07$ GHz. The valid range of values for m_v is restricted to 1-12%.

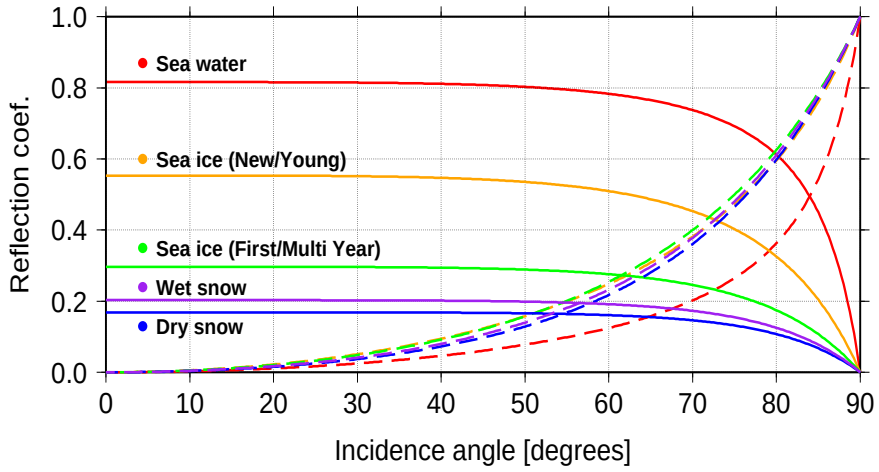

Figure 8.: Reflectivity Fresnel components (solid lines for $\Re_{cross}$ and dashed lines for $\Re_{co}$) for representative examples of sea water, sea ice and snow with circular polarizations at L-band: in red, sea water with Temp $= 5°$C and sal $= 35$ psu; in orange, new/young sea ice with $|\epsilon| = 10$; in green, First/Multi-Year sea ice with $V_b = 30‰$; in purple, dry snow with $m_v = 8\%$ and $\rho_s = 0.5$ gr/cm^3; and finally, in blue, dry snow with $\rho_s = 0.5$ gr/cm^3.

Several representative values of relative permittivity for the different types of media considered here are compiled in Table 5. The resultant Fresnel reflection coefficients for circular polarizations ($\Re_{co}$ and $\Re_{cross}$) using some of those examples are displayed in Figure 8. By checking the values of $\Re_{cross}$, we can see how the increase of liquid water and salinity enhances the reflecting capabilities of the media. The electromagnetic energy not reflected is thus transmitted into the medium, where it suffers attenuation given by the *attenuation constant* (α) (Ulaby et al., 1990b), which depends on the imaginary part of the relative permittivity as:

$$\alpha = \frac{2\pi}{\lambda}|\mathcal{I}m\{\sqrt{\epsilon}\}| \tag{26}$$

This coefficient relates the total amplitude of the field after traveling certain length z across the medium, with an exponential decay given by $e^{-\alpha z}$. Then, if z is the direction normal to the surface, the maximum depth of the medium that potentially contributes to the backscattered signal, known as *penetration depth* (δ_p), can be approximated by:

$$\delta_p = \frac{1}{2\alpha} \tag{27}$$

Table 5 contains the corresponding δ_p for each case. It is specially significant the case of dry snow, where large penetration depths, more than 100 m, might be reached due to the effect of the internal air voids of this type of medium (when comparing with pure ice) and its absence of liquid water.

Finally, the surface roughness at L-band scales of such type of media typically depends on external factors and is not restricted to a small range of values. Considering the case of sea water in open ocean scenarios, the surface roughness can be modeled as a function of the wind speed (Apel, 1994; Elfouhaily et al., 1997), with typical MSS variations between 0.007 (calm conditions) and 0.03 (high winds). Experiments done using GPS-L1 reflected signals show good agreement with these models (Komjathy et al., 2000b; Garrison et al.,

Medium	**Characteristics**	ϵ'	ϵ''	δ_p **[m]**
Sea water	Temp. = 15°C, sal. = 35 psu	73.423	56.067	0.005
	Temp. = 5°C, sal. = 35 psu	75.543	48.266	0.006
	Temp. = 5°C, sal. = 20 psu	79.024	33.726	0.008
Sea ice New/Young	$\lvert\epsilon_{si}\rvert = 10$ (Belmonte et al., 2009)	7.071	7.071	0.012
		9.806	1.961	0.048
		9.950	0.995	0.095
Sea ice FY/MY	$V_b = 0‰$	3.120	0.040	1.337
	$V_b = 5‰$	3.165	0.065	0.829
	$V_b = 10‰$	3.210	0.090	0.603
	$V_b = 30‰$	3.390	0.190	0.294
	$V_b = 70‰$	3.750	0.390	0.151
Pure ice	-	2.950	0.001	52.018
Dry snow	$\rho_s = 0.3$ gr/cm^3	1.533	0.0002	183.833
	$\rho_s = 0.4$ gr/cm^3	1.745	0.0003	130.030
	$\rho_s = 0.5$ gr/cm^3	1.977	0.0004	99.839
	$\rho_s = 0.6$ gr/cm^3	2.228	0.0005	81.015
Wet snow	$m_v = 3\%$, $\rho_s = 0.3$ gr/cm^3	1.909	0.052	0.806
	$m_v = 3\%$, $\rho_s = 0.5$ gr/cm^3	2.275	0.052	0.880
	$m_v = 8\%$, $\rho_s = 0.3$ gr/cm^3	2.794	0.188	0.270
	$m_v = 8\%$, $\rho_s = 0.5$ gr/cm^3	3.160	0.188	0.287

Table 5.: Relative permittivity values (real –ϵ'– and imaginary –ϵ''– parts) and penetration depths for different types of media at L-band.

2002; Cardellach et al., 2003). For the case of sea ice, the surface roughness mainly depends on the deformation and erosion processes in the ice pack, and for that reason, early stages of development tend to be smoother than older ones (Tucker et al., 1992). The roughness measurements obtained in Belmonte et al. (2009) using GPS-L1 reflected signals range from the model's lower threshold at $MSS = 0.004$ until $MSS \approx 0.03$ for the thicker categories of sea ice (first- and multi-year ice), and up to $MSS \approx 0.01$ for the thinner types (new and young ice). Lastly, in the case of dry/wet snow, the surface roughness is mainly influenced by wind and other large-scale processes like snowdrifts, snowfall and snowmelt (Fassnacht et al., 2009; Lacroix et al., 2008a). Examples of in situ measurements from different locations provide σ_h and L_{corr} values that, once applying Equation (12), result in MSS ranges of 0.002–0.012 (Svalbard (Lacroix et al., 2008b)) and 0.0025–0.0064 (Antarctica (Lacroix et al., 2008a)).

2.1.4 GNSS-R OBSERVABLES

From the contributions of the previous sections, we are able at this point to construct a tractable expression for the received SNR in a GNSS-R scenario where GSP L1 C/A-code signals are employed. By adding Equations (7) and (14) to (4), we obtain:

$$\begin{aligned} SNR(\tau,\kappa) &= \frac{P_t\lambda^2\pi}{(4\pi)^3 LKTB}\int_{surf}\frac{G_t(\vec{r})G_r(\vec{r})|\Re_{pq}(\vec{r})|^2}{R_1^2(\vec{r})R_2^2(\vec{r})}\Lambda^2_{C/A}(\tau+\delta\tau(\vec{r}))\cdot \\ &\quad \cdot|S_{C/A}(\kappa+\delta\kappa(\vec{r}))|^2\left(\frac{q(\vec{r})}{q_z(\vec{r})}\right)^4 P\left(-\frac{\vec{q}_\perp(\vec{r})}{q_z(\vec{r})}\right)\mathrm{d}^2r \end{aligned} \tag{28}$$

One can replace the constant terms before the integral by the square of the integration time, T_i^2, in order to get the equivalent expression for the normalized received power given in Zavorotny and Voronovich (2000). Considering that GPS is designed to equally illuminate the Earth surface (constant P_tG_t) and significant variations of incidence angle and permittivity are not typically expected around the reflecting surface (nearly constant $\Re_{pq}$), the main contribution to the integral in Equation (28) comes from the intersection of four spatial areas. The first area is given by G_r and corresponds to the receiver antenna footprint. The function $\Lambda^2_{C/A}$ marks the limits of the iso-delay annuli (centered at the specular point), which, for a given code, depend on the bistatic geometry (basically receiver's height and elevation angle). On the other hand, the function $|S_{C/A}|^2$ defines a set of iso-Doppler lines, whose locations are given by the relative velocity (projected over the surface) between receiver and transmitter, and their contribution depends on the integration time, as defined in Equation (6). Finally, the probability density function P of surface slopes delimits what is known as *glistening zone*, the area with facets properly oriented for direct reflection, whose size is proportional to the roughness conditions. By assuming a constant G_r (an omnidirectional antenna or a main beam covering the observation area), Figure 9 illustrates the impact of the latter three zones on the received signal's power, whose representation in the delay and Doppler domains is known as **Delay Doppler Map** (DDM). Examples of DDM's from real data are shown in Figure 10, where the top panel corresponds to a day with rougher conditions on the sea surface (provoked by high winds) and the bottom panel shows the results obtained under a

calm sea. Note how a rougher surface further spreads the power distribution across the DDM's area, whereas a smoother surface concentrates it around the specular point.

A partial representation of the DDM consists in taking a slice at $\Delta f_D = 0$ (κ equal to average Doppler shift and $\delta\kappa = 0$ in Equation (28)), to obtain what is known as **Delay Map** (DM) or simply **waveform**. This type of representation is the one that will be considered in this work due to the static conditions of the experimental setups later described in Chapter 3. In such case, the received power will be given by the interaction between $\Lambda^2_{C/A}$ and σ^0 (dominated by P), as displayed in Figure 11. We can see how, for rougher surface conditions, the waveform shape is expanded in the delay domain. On the other hand, a change in permittivity (under the same geometry) would simply behave as a scaling factor. Examples of waveforms obtained with real data are shown in Figure 12, where the comparison between both panels illustrates the spreading effect due to roughness.

The representation given by Equation (28) refers to power waveforms. However, dedicated GNSS-R receivers (Nogués-Correig et al., 2007; Helm et al., 2007) typically decompose the measurements in complex In-phase and Quadrature (I&Q) pairs of accumulated correlation units at the output of the matched filter, thus containing phase information, which is also considered a GNSS-R observable in the present work. These receivers then compute the I&Q components after a *coherent integration* time T_i on the order of a few milliseconds. In addition, the power waveform (the square value of the amplitude from the I&Q phasor) can be sequentially averaged up to several seconds, a process which is known as *incoherent integration*. These two type of integrations follow different purposes, as illustrated in Figure 13. The coherent integration raises the peak of the signal from the noise floor during the correlation process until its maximum level. The optimal duration of this integration is a tradeoff between the needed duration for exploiting the compression capabilities of the pseudo-random sequence employed (1 ms for the C/A-code) and the coherence properties of the reflected signal, which are dominated by the receiver's motion through the scattered signal's far field, as described by the van Citter-Zernike theorem, or by the dynamics –temporal variability– of the reflecting surface in the case of static (or nearly static) receivers. On the other hand, the incoherent integration filters out the remaining random fluctuations along the waveform produced –mainly– by what is known as *speckle/fading noise*. The source of such type of noise is the effect of the non-modeled instantaneous contributions into the reflected signal. Note that function P in Equation (28) essentially describes the average impact of the surface according to its roughness statistics, but not a particular realization of the surface. Then, as a result of the incoherent integration, the averaged waveform assembles better the model and therefore, it improves the latter extraction of geophysical information based on such modeling. The price paid is a loss of spatial resolution, since more observations are needed along the ground track to obtain a single retrieval (the integrated waveform). A more detailed analysis on the effect of coherent and incoherent averaging can be found in Cardellach (2002).

Finally, depending on the application sought, only determined characteristics of the previous observables (DDM's and waveforms) are actually needed, such as the peak value and its position over averaged waveforms, the width of a DDM or the phase variations in a complex (without incoherent averaging) waveform. These type of measurements are usually referred as *secondary observables*. They require some additional

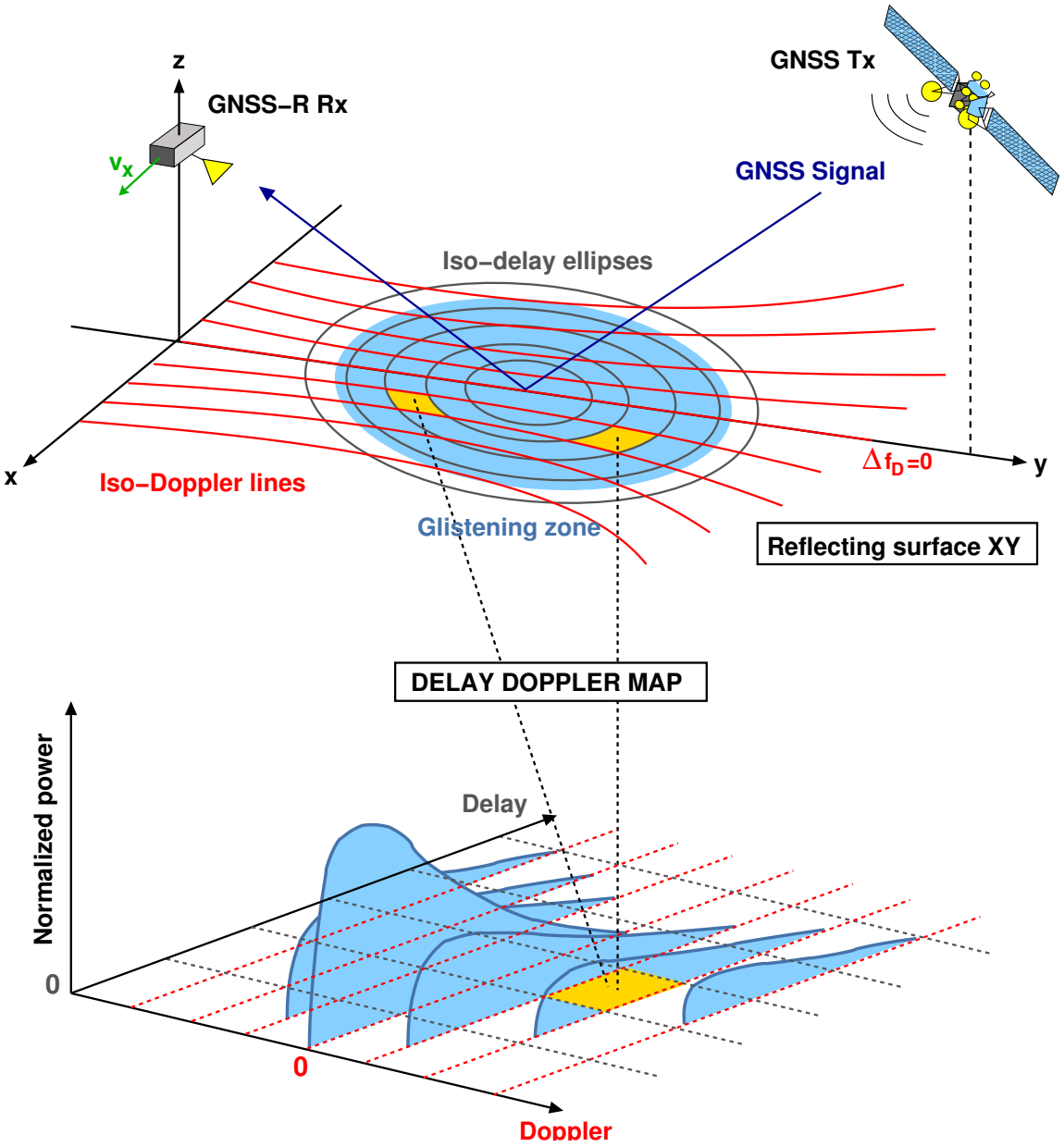

Figure 9.: Impact of the main contributors in a Delay Doppler Map (assuming a constant antenna gain over the observed area): the received power can be split in different components, each one coming from different cells on the reflecting surface. The cells are characterized by its relative delay with respect the specular point ray path and the relative Doppler shift. The size of the glistening zone (proportional to the roughness conditions) determines the spreading of the total power.

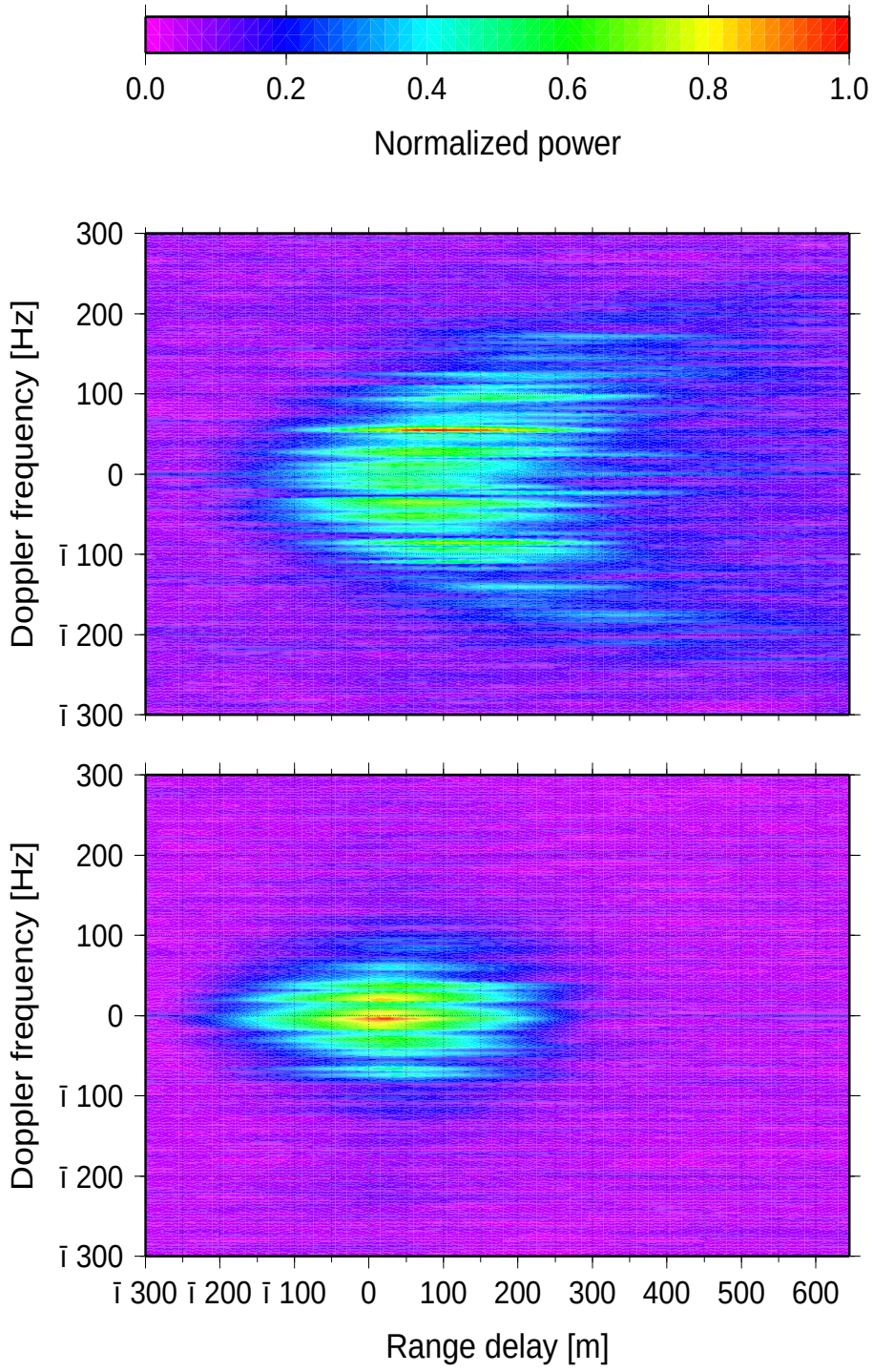

Figure 10.: Examples of DDM's obtained with real data from two different sea surface states during ESA's CoSMOS-OS 2006 at the North Sea. Both observables were taken with ICE/IEEC-CSIC's GOLD-RTR receiver, onboard an aircraft flying around 3.3 km high at 90 m/s over the same area. [Top] April 22, SoD = 80101, PRN 9 at 83° of elevation. Estimated $MSS = 0.036$. [Bottom] April 29, SoD = 71201, PRN 26 at 78° of elevation. Estimated $MSS = 0.005$. Data available at the web server described in Appendix B.

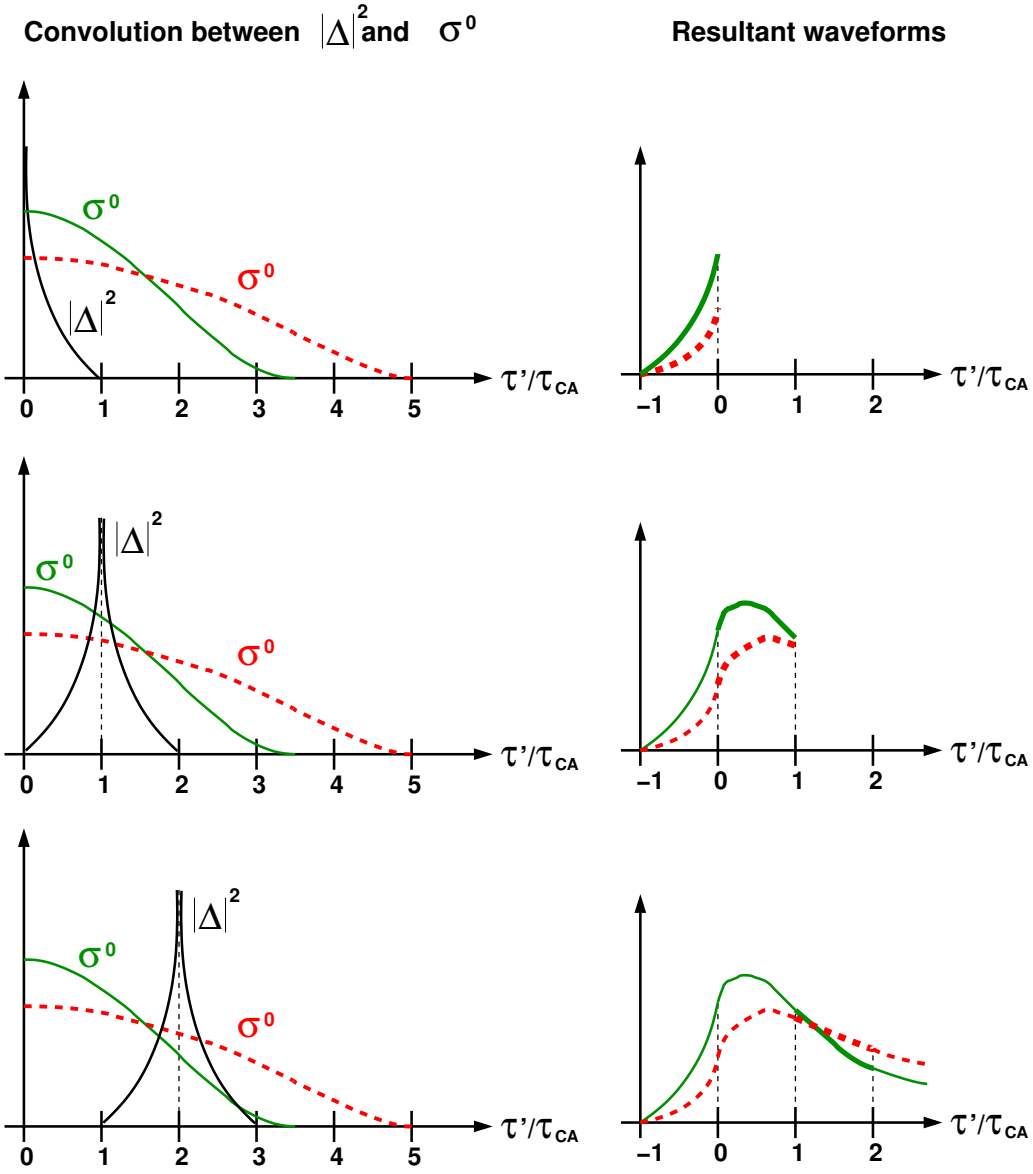

Figure 11.: Evolution of the received reflected power for two types of surfaces (green-smoother and red-rougher) and neglecting Doppler and antenna diagram effects. The rougher surface spreads the power of the received signals along the delay domain.

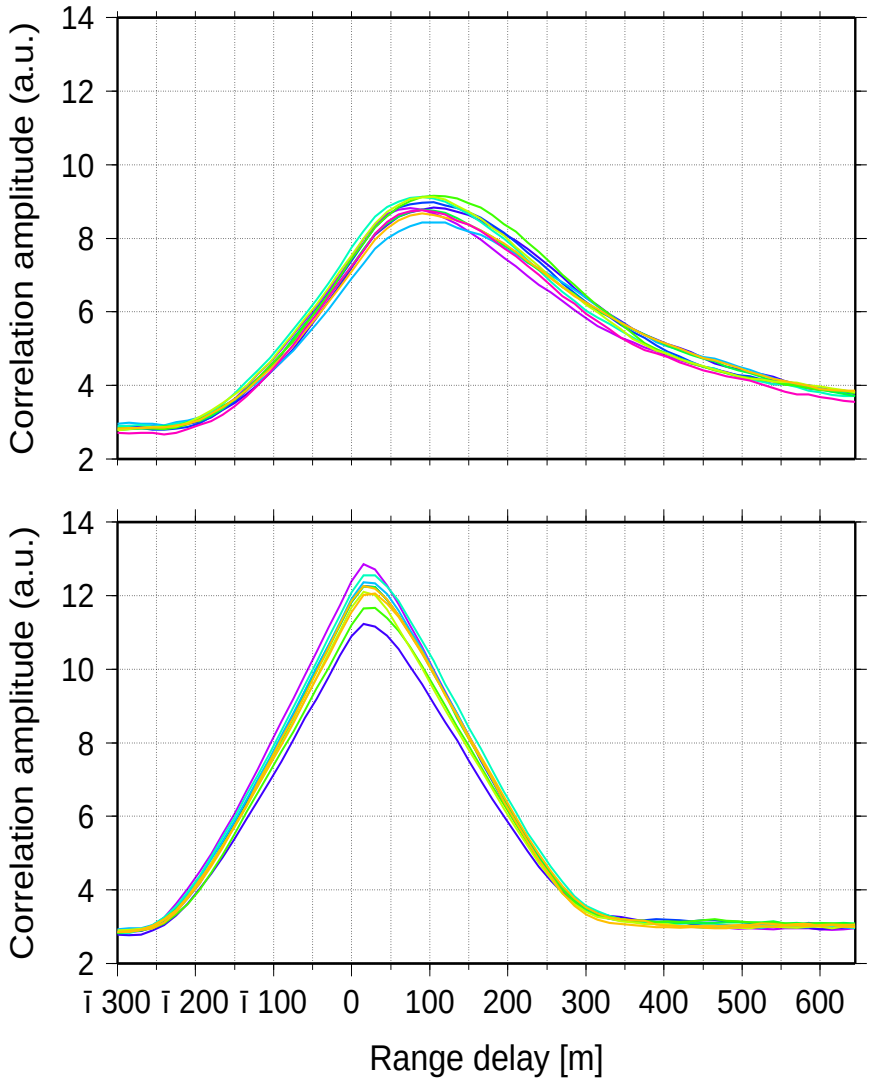

Figure 12.: Examples of waveforms obtained with real data from two different sea surface states during ESA's CoSMOS-OS 2006 at the North Sea (same characteristics as in Figure 10). Both sets of 10 consecutive observables (1 sec integration) were taken with ICE/IEEC-CSIC's GOLD-RTR receiver, onboard an aircraft flying around 3.3 km high at 90 m/s over the same area. [Top] April 22, SoD = 80101-80110, PRN 9 at 83° of elevation. Estimated $MSS = 0.036$. [Bottom] April 29, SoD = 71201-71210, PRN 26 at 78° of elevation. Estimated $MSS = 0.005$. Data available at the web server described in Appendix B.

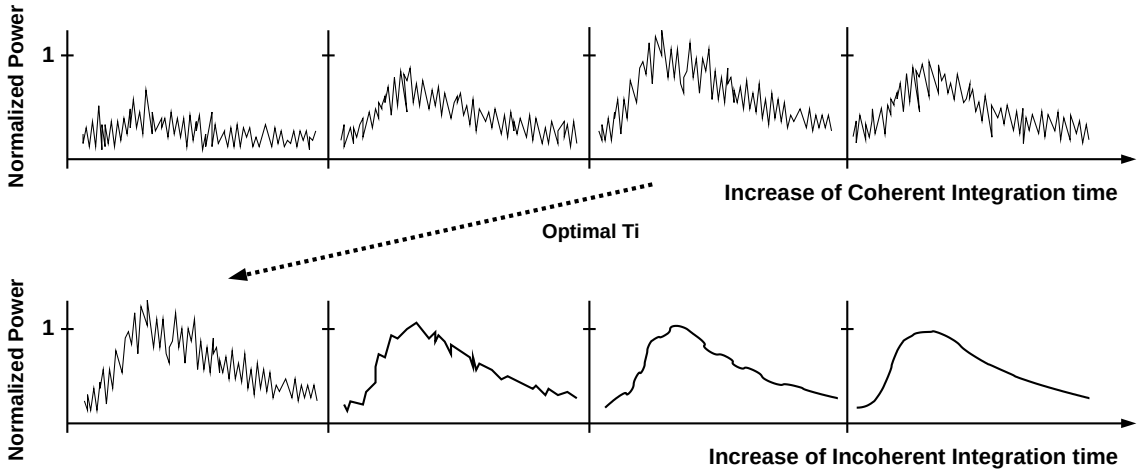

Figure 13.: Scheme of the effect of coherent (top) and incoherent (bottom) integration.

post-processing and are supposed to embed geophysical information. A comprehensive compilation of applications using a wide variety of secondary observables from reflected GNSS signals can be found in Cardellach et al. (2011). Chapters 4 and 5 will later introduce the secondary observables considered in the present work for remote sensing of sea ice and dry snow respectively.

2.2 REMOTE SENSING OF POLAR ENVIRONMENTS: STATE OF THE ART

Given the severe conditions that characterize polar environments, i.e. vast unpopulated extensions of ice sheets with continuous periods of extremely low temperatures, the most convenient way for their monitorization is the use of remote sensing instruments onboard satellites following polar orbits. A compilation of spaceborne sensors that were operational during the period of this work is given in Tables 6 (*active* approaches) and 7 (*passive* approaches). In the first group we have altimeters, scatterometers and the higher resolution synthetic aperture radars (SAR), which essentially use electromagnetic pulses at low microwave frequencies (with the exception of laser altimeters) to excite the Earth's surface and then to analyze the backscattered signal. On the other hand, the second group is conformed by a wide variety of radiometers, which basically measure thermal emissivity, radiance or reflectance of the Earth's surface, depending on whether observations are made in the microwave, infrared or visible frequency band. Note that the GNSS-R concept, in spite of being usually referred as *passive* because it employs the signals transmitted by an *external* system (the GNSS constellation), would belong to the family of *active* approaches in this classification.

The frequency band employed plays a key role on the applicability of a remote sensing instrument. Generally speaking, the smaller the wavelength, the better the resolution that can be achieved, but at the same time, the major the number of effects that scatter or attenuate the electromagnetic signal (more power-demanding). As a result from this trade-off, microwave instruments are typically preferred for monitoring the cryosphere, which contrary to visible or near-infrared sensors, can operate at night and for all weather conditions (clouds and precipitations have non/weak impact). Similarly, transmitted signals at the lower frequency bands of the microwave electromagnetic spectrum can penetrate into the surface snow cover in order to retrieve information from the ice layers beneath. Therefore, the convenience of using a determined spaceborne sensor will mainly depend on the application sought. Table 8 provides the main cryospheric retrievals from each type of system. In practice, the full characterization of cryospheric extensions is usually done by combining the measurements from different instruments (including local observations) in order to overcome their single limitations (Cavalieri et al., 1999; Andersen et al., 2006; Dedrick et al., 2001). A clear example is the elaboration of sea ice chart products (NSIDC, 2010; PV-DMI, 2013) employed in climatology.

The Global Terrestrial Observing System (GTOS), Global Climate Observing System (GCOS), World Meteorological Organization (WMO), and Committee on Earth Observation Satellites (CEOS) all support consistent global observations and measurements. To accomplish this goal, a set of Essential Climate Variables (ECV) have been defined as measurements of atmosphere, oceans, and land that are technically and economically feasible for systematic observation and that are needed to meet the United Nations Framework Convention on Climate Change and requirements of the Intergovernmental Panel on Climate Change (Stitt et al., 2011). Sea ice, now cover, and ice sheets are ECVs for which long-term, global-scale, accurate, timely and consistent measurements are required, and GCOS (2009) states that sea ice and snow cover are ECVs largely dependent upon satellite observations.

Instrument	Mission	Launch	End	Inclination	Repeat interval	Swath	Frequency band	Spatial resolution
ALTIMETER								
RA	ERS-2	Apr 1995	July 2011	98.52°	35 days	20 km	Ku (13.575 GHz)	400 m intervals (8 km)
RA-2	Envisat	March 2002	May 2012	98.6°	35 days	20 km	Ku (13.575 GHz) S (3.2 GHz)	400 m intervals (8 km)
GLAS	ICESat	Jan 2003	Oct 2009	94.0°	91 days	70 m	Infrared (λ = 1064nm) green light (λ = 532nm)	170 m intervals
SIRAL	Cryosat-2	Apr 2010	–	92.0°	369 days	250 m	Ku (13.7 GHz)	250 m intervals
SCATTEROMETER								
SeaWinds	QuikSCAT	June 1999	Nov 2009	98.6°	100.93 min*	1800 km	Ku (13.4 GHz)	25 km
WS	ERS-2	Apr 1995	July 2011	98.52°	35 days	500 km	C (5.3 GHz)	25 km
ASCAT	MetOp	Oct 2006 (A), Sept 2012 (B)	–	98.7°	29 days	2x500 km	C (5.255 GHz)	25 km
SYNTHETIC APERTURE RADAR								
SAR	ERS-2	Apr 1995	July 2011	98.52°	35 days	100 km	C (5.3 GHz)	30 m
ASAR	Envisat	March 2002	May 2012	98.6°	35 days	5/100/400 km	C (5.3 GHz)	30 to 1000 m
PALSAR	ALOS	Jan 2006	Apr 2011	98.16°	46 days	30/70/250-360 km	L (1.27 GHz)	10-100 m
SAR	RADARSAT-1	Nov 1995	–	98.6°	24 days	45-500 km	C (5.3 GHz)	8-100 m
SAR	RADARSAT-2	Dec 2007	–	98.6°	24 days	18-500 km	C (5.405 GHz)	3-100 m
SAR/I	TerraSAR-X, TanDEM-X	June 2007, June 2011	–	97.44°	11 days	10/30/100 km	X (9.65 GHz)	<12 m
SIRAL	Cryosat-2	Apr 2010	–	92.0°	369 days	250 m	Ku (13.7 GHz)	250 m

Table 6.: Operational spaceborne active sensors monitoring polar environments between 2008/2012. (*) Orbital period instead of repeat interval.

Instrument	Mission	Launch	End	Inclination	Orbital period	Swath	Frequency band	Spatial resolution
MICROWAVE RADIOMETER								
AMSU-A	POES	May 1998 (NOAA-15 until NOAA-19)	–	98.5°-99.0°	101.1-102.14 min	1650 km	15 bands: 23.8-89 GHz	40 km
	Aqua	May 2002	–	98.14°	98.8 min	1650 km		40 km
	MetOp	Oct 2006 (A), Sept 2012 (B)	–	98.7°	101 min	2074 km		48 km
AMSR-E	Aqua	May 2002	–	98.14°	98.8 min	1445 km	6 bands: 6.9-89 GHz	4-75 km
SSM/I	DMSP	June 1987 (F8 until F15)	–	97.6°-98.8°	96.86-101.9 min	1400 km	4 bands: 19.35-85.5 GHz	15-69 km
SSMI/S	DMSP	Oct 2003 (F16 until F18)	–	98.8°-98.9°	101.9-102.0 min	1707 km	15 bands: 19-183 GHz	14-73 km
WindSat	Coriolis	Jan 2003	–	98.7°	102.6 min	1000 km	5 bands: 6.8-39 GHz	13-71 km
MIRAS	SMOS	Nov 2009	–	98.44°	23 days*	1000 km	L (1.4 GHz)	35 km
OPTICAL/NEAR-INFRARED RADIOMETER								
AVHRR	POES	May 1998 (NOAA-15 until NOAA-19)	–	98.5°-99.0°	101.1-102.14 min	2500 km	6 λ: 0.58-12.5 μm	1.09 km
	MetOp	Oct 2006 (A), Sept 2012 (B)	–	98.7°	101 min	3000 km		1.09 km
MODIS	Terra	Dec 1999	–	98.2°	98.8 min	2230 km	36 λ: 0.4-14 μm	250/500/1000 m
	Aqua	May 2002	–	98.14°				
ETM+	Landsat	Apr 1999 (7)	–	98.2°	16 days*	183 km	8 λ: 0.45-12.5 μm	15/30/60 m
ALI	EOS-1	Nov 2000	–	98.2°	16 days*	37 km	10 λ: 0.433-2.35 μm	10/30 m

Table 7.: Operational spaceborne passive sensors monitoring polar environments between 2008/2012. (*) Repeat interval instead of orbital period.

ALTIMETERS
Sea ice type and concentration (Fetterer et al., 1992)
Sea ice thickness (Zwally et al., 2008)
Monitorization of ice sheet mass balance (Rémy and Parouty, 2009)
Glacier topography (Rémy and Parouty, 2009)
SCATTEROMETERS
Sea ice mapping (Onstott, 1992; Remund and Long, 1999; Anderson and Long, 2005; Belmonte-Rivas and Stoffelen, 2011)
Sea ice classification (Onstott, 1992)
Snow accumulation (Drinkwater et al., 2001)
SYNTHETIC APERTURE RADAR
Sea ice concentration (Onstott, 1992; Onstott and Shuchman, 2004)
Sea ice classification (Onstott, 1992; Onstott and Shuchman, 2004; Partington et al., 2010; Ochilov and Clausi, 2012)
Sea ice thickness (Onstott, 1992; Onstott and Shuchman, 2004)
Snow mapping (Koskinen et al., 1997; Nagler and Rott, 2000)
Monitorization of ice sheet dynamics (Shuchman et al., 2004; Rignot et al., 1995; Mouginot et al., 2012)
MICROWAVE RADIOMETERS
Sea ice concentration (Eppler et al., 1992; Kwok, 2002; Comiso et al., 2003)
Sea ice classification (Eppler et al., 1992)
Thin sea ice thickness (Kaleschke et al., 2012)
Snow mapping (Amlien, 2008)
Snow depth and water equivalent (Amlien, 2008)
OPTICAL/NEAR-INFRARED RADIOMETERS
Sea ice surface temperature (Key and Haefliger, 1992; Hall et al., 2004)
Sea ice concentration (Burns et al., 1992; Drüe and Heinemann, 2004)
Thin sea ice thickness (Yu and Rothrock, 1999)
Snow mapping (Hall et al., 2002)
Snow grain size (Lyapustin et al., 2009)

Table 8.: Cryospheric retrievals from current spaceborne sensors.

Despite the long list of observing systems listed in Table 8, sea ice, snow cover and ice sheet ECVs present data gaps. For instance, snow cover data from many sources need to be blended to obtain globally applicable data. Standard methods are needed to validate and quantify the accuracy of satellite-based passive microwave retrieval algorithms. Snow-cloud discrimination needs to be improved while avoiding sensor saturation. Errors associated with not detecting snow cover under forest canopy need to be quantified and techniques developed to adjust for these errors (Stitt et al., 2011). Moreover, as summarized in Uppala et al. (2011), there are a set of ECVs the provision of which needs to be secured at European and global scale. Among them: snow cover, glaciers and ice caps, sea ice, and ice sheets.

2.2.1 GNSS-R OVER SEA ICE AND DRY SNOW: POTENTIAL BENEFITS AND PREVIOUS/CURRENT WORK

Limited by the weak power of the transmitted signals (which were specially designed for navigation purposes), a GNSS-R system could rarely improve by itself the main characteristics of any dedicated sensor (e.g. the single-shot accuracy of a Ku-band radar altimeter or the spatial resolution of a SAR image); but, on the other hand, it would represent a low-cost source of opportunity to augment the existing observation techniques, thus providing more continuity to the on-going missions that monitor Polar environments. Moreover, the fact of having multiple transmitters available at the same time (multi-static concept) increases the effective swath of observation when comparing GNSS-R against any other radar altimetric approach (with whom shares more similarities), and therefore it enables the possibility of obtaining mesoscale measurements (Martín-Neira, 1993). Previous Figure 2 illustrates this property. In addition, Figures 14 and 15 show the comparison in terms of daily Polar coverage between a nadir-looking altimetric radar and a GNSS-R receiver working only with GPS signals, as obtained by simulation assuming a spaceborne platform with the orbital characteristics from the MetOp mission.

Regarding GNSS-R over sea ice, Komjathy et al. (2000a) first showed correlation between the peak power of GPS returns and RADARSAT backscattered measurements over this type of surfaces. More recently, similar results have been achieved from space (Gleason, 2010). In Belmonte et al. (2009), permittivity and roughness retrievals are obtained from the analysis of the shape of GPS waveforms reflected off different types of sea ice. These measurements are compared against polarimetric microwave emissions, RADARSAT backscatter, MODIS imagery and a LIDAR profiler. The results obtained conclude that GPS-R retrievals (and thus GNSS-R) are helpful in the interpretation of signatures observed by the more traditional sensors, in particular, *for the detection of surface glaze effects in microwave emission and the breaking of the salinity/roughness ambiguity in radar backscatter*. In addition, the large GPS wavelength avoids volume effects from snow and ice internal inhomogeneities. This property is also related to ice thickness retrieval, which is one of the most important features in the determination of sea ice development stage (Onstott, 1989). This parameter can be estimated from the measurement of the normal distance between the floating line and the ice surface (freeboard level) with accurate laser altimetry (Zwally et al., 2008). However, the snow loading plays a key role in this estimation and the accuracy of its determination with other instruments affects the final result. The use of L-band GNSS-R signals for precise altimetry, with snow penetration

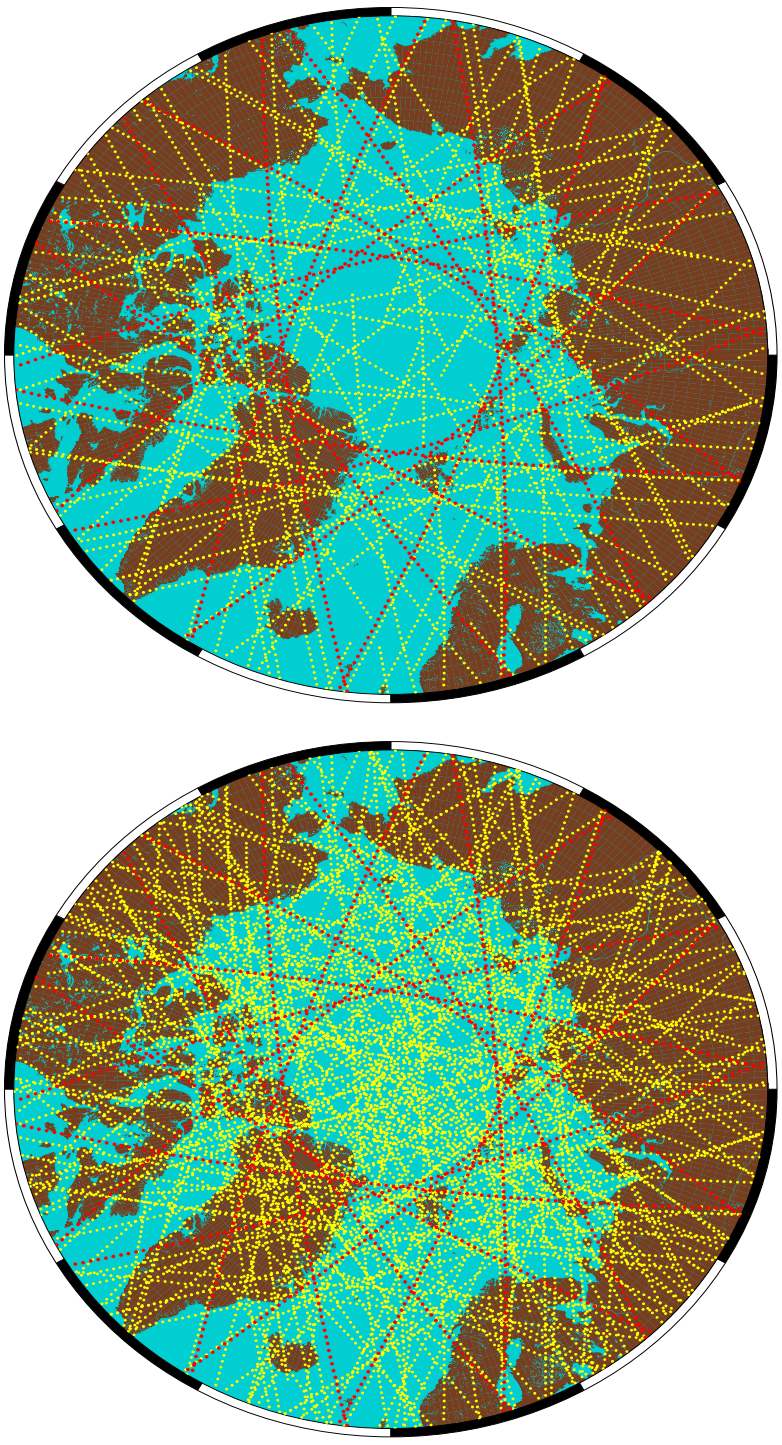

Figure 14.: Simulated daily coverage at the North Pole of a nadir-looking altimetric radar (red footprints) and a GNSS-R receiver (yellow footprints) working with GPS-L1 signal. The orbital characteristics of the MetOp platform have been taken. Two different thresholds for the minimum elevation angle on the GNSS-R signals are considered: [Top] 30° and [Bottom] 5°.

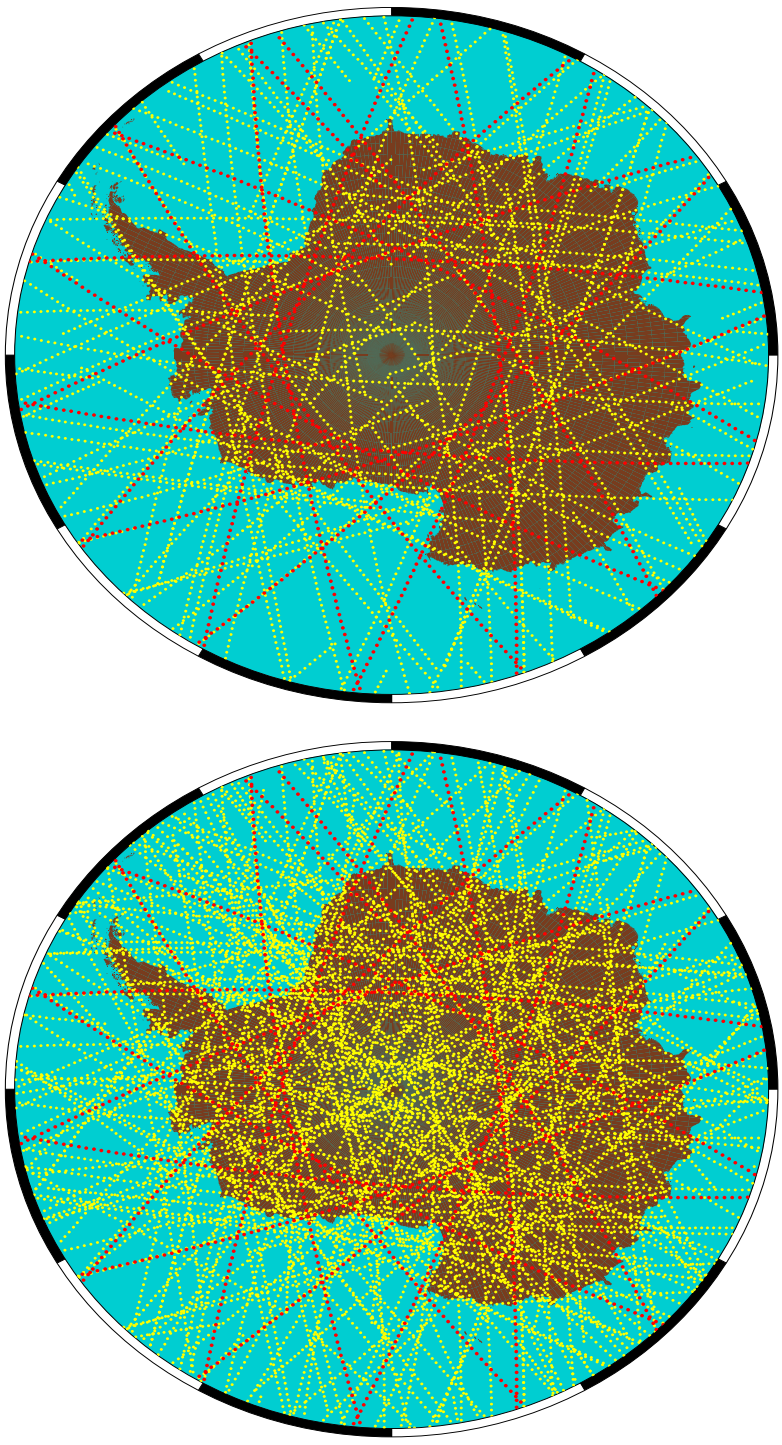

Figure 15.: Simulated daily coverage at the South Pole of a nadir-looking altimetric radar (red footprints) and a GNSS-R receiver (yellow footprints) working with GPS-L1 signal. The orbital characteristics of the MetOp platform have been taken. Two different thresholds for the minimum elevation angle on the GNSS-R signals are considered: [Top] 30° and [Bottom] 5°.

depths ranging from ∼1 meter to more than 100 meters (as shown in Table 5 from Section 2.1.3.1), would overcome this limitation, providing additional means and knowledge towards a better sea ice classification.

Finally, the monitorization of large ice sheet extensions, such the Antarctic plateau, might also be benefited by the aforementioned transparency of snow for L-band GNSS-R signals. The results obtained with dual-frequency radar altimeters confirmed that signals from the lower band of the microwave spectrum might be used as a sounding radar in this type of environments (Rémy and Parouty, 2009). This approach could be then employed to attempt the retrieval of the internal layering from large ice sheets extensions, which is related to the accumulation rate (Eisen et al., 2008). In this sense, theoretical models developed by Wiehl et al. (2003), which represent the first and only work –until the present study– of GNSS-R over thick –several meters– dry snow masses, suggest the potential of inferring snow surface roughness and firnpack parameters like accumulation rates from GNSS-R measurements. Other works employing GNSS signals for snow observation exploit the interference pattern experienced by the direct signal's power along different elevation angles, that can be measured with geodetic GPS receivers located near the ground level. In Larson et al. (2009), this pattern is modeled by the impact of a signal reflected off a snow cover, which is a function of the vertical distance between the receiver and the surface point of reflection. The thickness of the snow layer is then retrieved from the estimated height variations during snowy seasons (at the order of several centimeters). Similarly, Jacobson (2010) studies the impact produced by a signal reflected off a soil surface beneath a snow cover, which is a function of this layer's thickness and the dielectric characteristics of the different mediums involved, to retrieve snow depth and snow water equivalent from this single and thin –several centimeters– snow layer. Similar results are also obtained in Rodriguez-Alvarez et al. (2011) with a dedicated GNSS-R receiver that works with linear polarizations and exploiting the same type of approach.

Table 9 summarizes the main contributions in GNSS-R for remote sensing of the cryosphere which are previous or contemporary to the work presented in this thesis.

PUBLICATION	DESCRIPTION
Komjathy et al. (2000a)	**Sea ice** detection after comparing the peak power of GPS reflections received by airborne instruments, with RADARSAT backscattered.
Belmonte-Rivas (2007); Belmonte et al. (2009)	**Sea ice** permittivity and roughness retrieved from the analysis of the shape of GPS-R waveforms received by airborne instruments. Potential characterization of different stages of **sea ice** after comparison with other remote sensing techniques.
Gleason (2010)	**Sea ice** detection after comparing the peak power of GPS reflections collected onboard a satellite, with ice concentration measurements obtained with AMSR-E and ice charts.
Wiehl et al. (2003)	Theoretical model for GNSS-R over thick –several meters– **dry snow** masses. Potential of inferring snow surface roughness and firnpack parameters like accumulation rates.
Larson et al. (2009)	**Snow** thickness variations (at the order of several centimeters) retrieved from the interference pattern measured with a geodetic GPS receiver on ground. The approach models the pattern by the contribution of a signal reflected off the snow surface level.
Jacobson (2010)	**Snow** depth and snow water equivalent retrieved from the interference pattern measured with a geodetic GPS receiver on ground. The approach models the pattern by the contribution of a signal reflected off a soil surface beneath a thin –several centimeters– and single snow layer.
Rodriguez-Alvarez et al. (2011)	**Snow** thickness retrieved from the interference pattern measured with a dedicated GNSS-R receiver located near the ground level. The approach models the pattern by the contribution of a signal reflected off the snow surface considering the internal properties of a thin –several centimeters– and single snow layer.

Table 9.: Main contributions in GNSS-R for remote sensing of the cryosphere which are previous or contemporary to this work.

3

GNSS-R EXPERIMENTAL SYSTEM ANALYSIS

This Chapter gives details about the technical aspects of the experimental campaigns which are especially relevant for the analysis made in this work. Section 3.1 shows the characteristics of the instrumentation employed. Sections 3.2 and 3.3 provide a basic description of the campaign's scenario and the main observables studied for the remote sensing of sea ice and dry snow, respectively.

3.1 THE EXPERIMENTAL SETUP

We have seen in Chapter 2 that a common GNSS-R system basically requires a means for gathering direct and reflected signals, to later obtain the waveforms by cross-correlating these received signals against a clean replica. These elements can be distinguished in the scheme of the experimental setup shown in Figure 16. A zenith-looking antenna collects direct GPS signals in their original polarization (RHCP), while a horizon-looking antenna gathers reflections in two circular polarizations (Left- and Right-handed). Both antennas are active (internal low noise amplifier) and have a near-hemispherical beamwidth. Their outputs are connected to the receivers' front ends through long coaxial cables (type LMR-400). The direct signal is shared between the main instrument (a GNSS-R receiver) and a Geodetic receiver with a power splitter. These two instruments are in charge to process the GPS signals in order to get the main inputs (waveforms and positioning respectively). A terminal unit controls their configuration and manages the proper storage of data using Ethernet connections. By means of a router, the computer can be controlled remotely through Internet or a local area network. In addition, a set of jacks that supply power to the system can be accessed in the same way, offering the possibility of forcing a restart of any component of the equipment. Under this architecture, an operator is able to download data, upload configurations files and monitor the whole system in real time with the appropriate software tools from a remote location. Further details of the complete system's architecture developed at ICE towards these purposes and dedicated for these experimental campaigns are given in Appendix C.

An estimation of the gain of the setup and its noise figure is presented as follows, which demonstrates that the signal quality of the different GPS receivers is the appropriate one to obtain good measurements. To perform the estimations the model of Figure 17 has been used.

The antenna gain (directivity) and the gain of its built-in low noise amplifier are $G_a \approx$ 5dB, $G_{LNA} \approx$ 33dB. The attenuation of the cable is 4.2dB, where a 25m long LMR-400 (16.8dB/100m) is employed. We can add to this attenuation the insertion losses of the power splitter 0.3dB. Thus, $L_c = 4.5$dB. The total gain of the system is the given by

$$G_{eq} = G_a + G_{LNA} - L_c = 33.5\text{dB} \tag{29}$$

The antenna temperature is assumed to be $T_a = 200$K. The equivalent noise temperature of the LNA is obtained from its noise figure $F_{LNA} = 2$dB, being $T_{LNA} \simeq 170$K. The equivalent noise temperature of the cable is $T_c \simeq 527$K, where it has been assumed a physical temperature of 290K. The overall equivalent noise temperature T_{eq} is obtained using Friis' formula (Friis, 1944):

$$T_{eq} = T_a + \frac{T_{LNA}}{G_a} + \frac{T_c}{G_a G_{LNA}} \simeq 254\text{K} \tag{30}$$

From that an equivalent noise figure of the setup F_{eq} of 2.73dB is obtained.

With these values for the gain and noise figure we can assure that the Geodetic Receiver and the GOLD-RTR will have correct signal levels at their input.

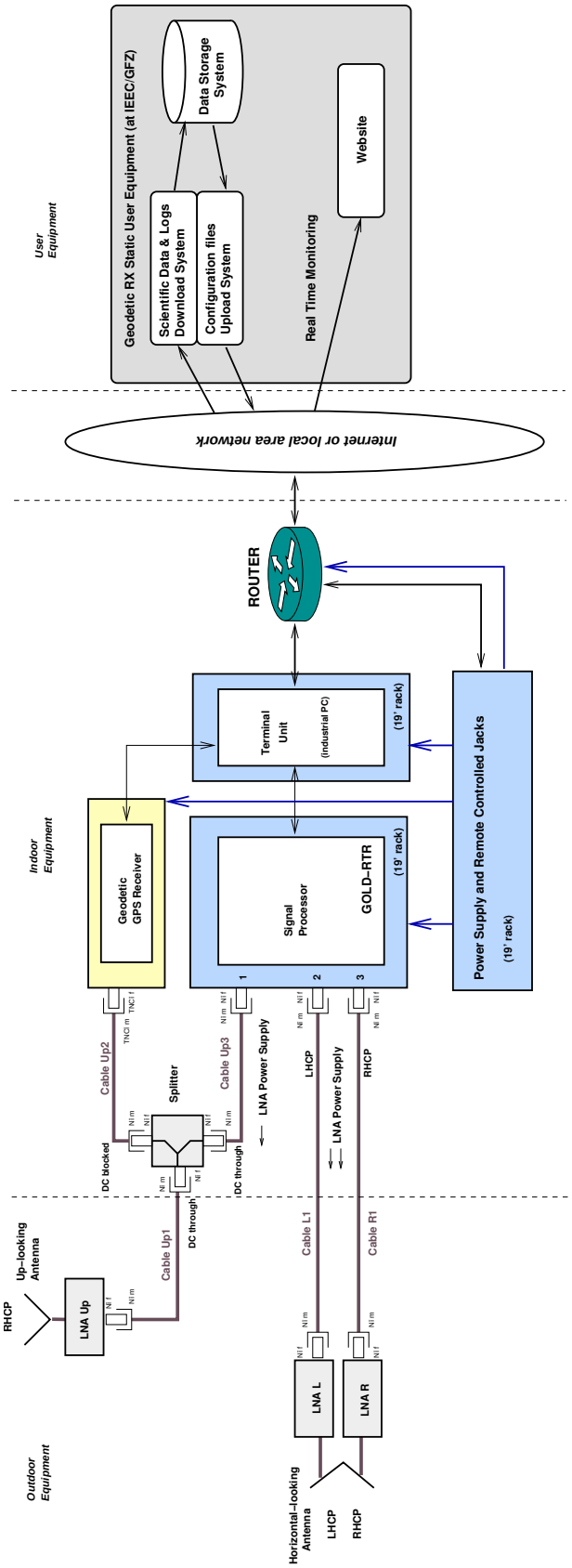

Figure 16.: Block diagram of the experimental setup used during Greenland and Antarctica campaigns.

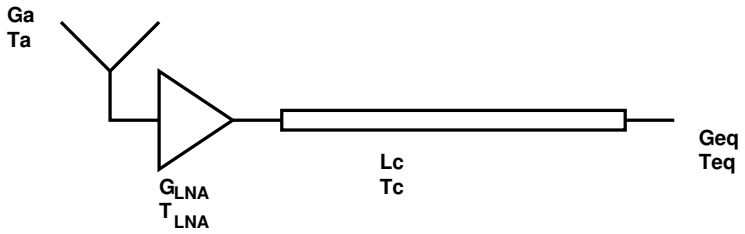

Figure 17.: Model of the setup used to estimate its gain and equivalent noise figure.

3.1.1 THE GNSS-R RECEIVER: GOLD-RTR

The main instrument employed in this study has been the GPS Open Loop Real Time Receiver (GOLD-RTR) (Nogués-Correig et al., 2007), a dedicated GNSS-R receiver that computes real-time waveforms. Three Radio-Frequency (RF) front-ends, here and on referred as Links, perform direct In-phase and Quadrature (I&Q) down-conversion of the GPS C/A L1 signals from RF to baseband. Despite the system's reference oscillator operates at 40 MHz, the effective sampling rate is, by design, 20 MHz (R_{eff}). The down-converted I&Q signals are then converted to 1-bit digital signals (with six comparators performing sign extraction). A digital real-time signal processor, made out of 640 complex correlators organized in 10 configurable channels (64 complex correlators each), compute the I&Q waveforms each millisecond. The flowchart in Figure 18 shows the process described. Then, the GOLD-RTR is able to deliver up to 10 complex waveforms of 64 lags every millisecond. This delivery is made using the User Datagram Protocol (UDP), where data integrity is not guaranteed (some data may be lost) to avoid the overload of such processing at the network interface level, and therefore, is specially suitable for real-time systems. In practice, the amount of data lost due to the UDP protocol can be considered negligible.

The lag-spacing (Δ_{lag}) of the waveforms is given by

$$\Delta_{lag} = \frac{c}{R_{eff}} \approx 15 \text{ m} \approx 0.05 \ \tau_{\text{C/A}} \tag{31}$$

being c the speed of light in the free space. A first approximation of the delay is required to locate them in the space domain. The GOLD-RTR is a **differential** receiver, assisted by a Novatel GPS receiver card inside the GOLD-RTR device. Real-time estimations about the expected delays and Doppler frequencies of the satellites are computed based on information provided by the Novatel card. By default, the signal from Link-1 is shared with this internal GPS receiver. The satellite's selection comes from the configuration files that have to be supplied as an input to the GOLD-RTR. An example of configuration file is given as follows:

```
1660 86400 run 10
 23 1 Up 0 150 0
 23 2 Dw 0 150 0
 23 3 Dw 0 150 0
 12 1 Up 0 0 0
 12 2 Dw 0 0 600
 12 3 Dw 0 0 600
```

```
 31 2 Dw -100 0 0
 31 2 Dw -50 0 0
 31 2 Dw 50 0 0
 31 2 Dw 100 0 0
1660 86401 idle 0
```

The first line tells the receiver to start an experiment at GPS week 1660 (first variable) and second of the week 86400 (second variable), with the 10 channels *running*. The next 10 lines control each of those channels with the different variables along six columns. First column refers for the PRN number of the C/A code replica modeled for the correlation (basically, it chooses a GPS satellite). Second column selects from which Link the real signals will be taken. The third column has two options: *Up* and *Dw*. With the aim of centering the resultant waveform in the observation window (center at lag 32), the receiver makes a first approximation of the delay experimented by a signal reflected over a model of the Earth's surface (ellipsoid WGS84) with respect to the direct one, and may add this parameter to the correlations (*Dw*) or not (*Up*). Therefore, in most cases, *Up* is the appropriate option when tracking direct signals, and *Dw* when looking for reflections. The fourth column is employed for adding additional Doppler frequencies –positive or negative Hz– to obtain DDM's (the "original" Doppler frequency at the specular point from the receiver-to-transmitter relative movement is added by default in the correlations). The fifth column defines the offset range-delay of the waveform –in meters– (used to "move" the waveform away from the center position). The value from the last column only has effect when *Dw* is chosen in the third field by adding a vertical height in meters to the modeled surface level given by ellipsoid WGS84. This parameter is specially needed for most of in-land areas, where the actual value of this vertical distance may reach several hundred of meters. Finally, the last line tells the receiver to finish the experiment (*idle*) at the next second of the week (86401). It is not mandatory to update the configuration of the Channels every second, but this is the minimum time interval for doing it. Therefore, we can assure that the correlation parameters keep constant during each GPS second.

The GOLD-RTR interacts with the computer with a given software application that basically loads the configuration files for managing an experiment, and stores the data delivered in real-time by the receiver. In addition, it enables the possibility of performing further integration of the waveforms from 1 msec (RAW data) to 1 sec (INT data) with the purpose of saving storage capabilities in long term campaigns. However, that saving is not free in the sense that the integration has to be done *incoherently* (sum of amplitudes), and therefore, phase information is lost (which is no needed for certain applications). As a last remark, taking into account the experimental setup considered for this study and previously described, the primary observables obtained by the GOLD-RTR with each data type are summarized in Table 11.

As a last comment, another dedicated GPS reflectometry receiver was employed during the experimental campaign: GNSS Occultation, Reflectometry and Scatterometry space receiver (GORS) (Helm et al., 2007). This instrument, configured and remotely operated by GFZ, collected direct and reflected GPS signals through an additional RHCP antenna, which was tilted 45° from the Horizon (the smaller antenna that appears at the setup's pictures in Figure 20). It provides an output from up to 10 channels with 2 complex correlators (for peak-pairs of direct and reflected signals instead of full wave-

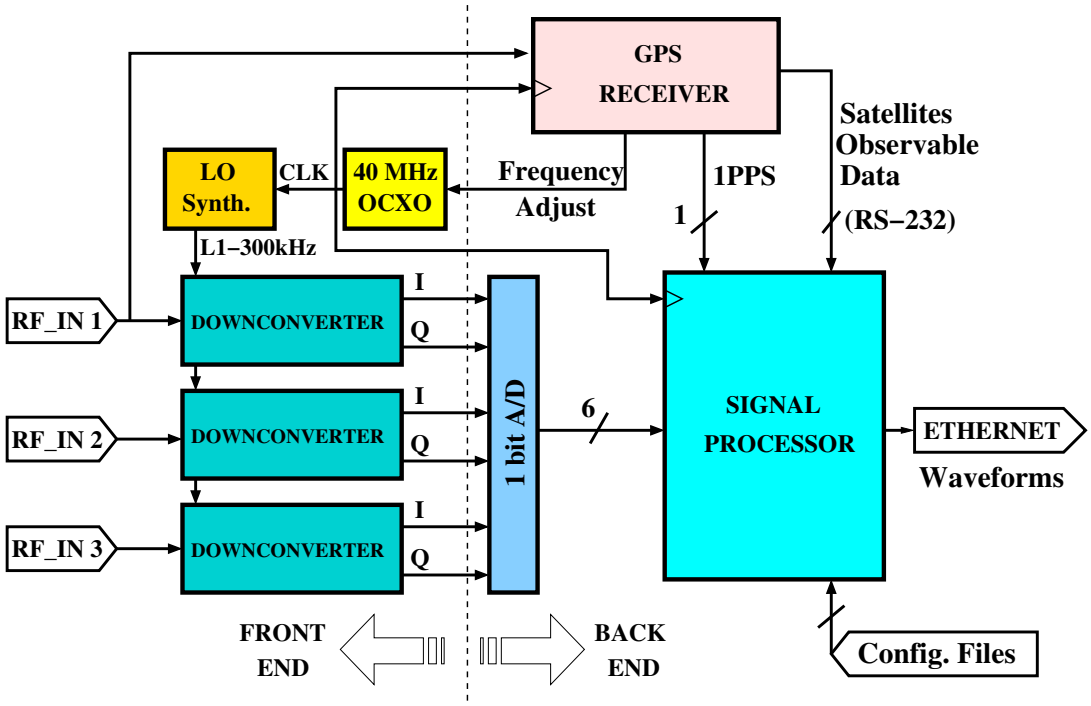

Figure 18.: Block diagram of the GOLD-RTR instrument rack electronics. The GPS signals from the 3 inputs (RF_IN) is first down-converted and digitalized. Then, a signal processor computes the cross-correlation against the models provided by the internal GPS receiver depending on the characteristics given by the configuration files. The resultant waveforms are delivered to the terminal unit through an Ethernet connection. Figure from Nogués-Correig et al. (2007).

Type	Sampling	RF LINK	Observables
INT	1 sec	Zenith-looking RHCP Horizon-looking LHCP Horizon-looking RHCP	64-lag amplitude waveform, 15 m inter-lag space
RAW	1 msec	Zenith-looking RHCP Horizon-looking LHCP Horizon-looking RHCP	64-lag complex (I&Q) waveform, 15 m inter-lag space

Table 11.: Observables collected by the GOLD-RTR during the GPS-SIDS experimental campaigns. INT stands for Integrated Data (1 sec), RAW for Raw Sampling Data (1 msec).

forms), with a rate of 200 Hz and working at two frequencies: GPS L1/L2 with C/A and L2C codes respectively. The results obtained with this instrument during Greenland's campaign, focused on altimetric applications, were presented in Semmling et al. (2011, 2012).

3.2 CAMPAIGN OVER SEA ICE

This section provides a description of the different elements needed for the analysis of GPS reflections over sea ice (later developed along Chapter 4): experimental site and collected GNSS-R data.

3.2.1 SCENARIO: QEQERTARSUAQ, GREENLAND

The experimental campaign took place on the South tip of Disko Island, in the western coast of Greenland. A proper location for sea ice monitoring was found next to the port of Godhavn (Qeqertarsuaq), on the edge of a cliff of approximately 650 meters high above sea level (69.27°N, 53.54°W). The antennas were installed on top of a telecommunications tower (18 meter high), with clear visibility over Disko Bay, as it can be seen on the different pictures in Figures 19 and 20, and looking South, where most of the GPS constellation lies at these latitudes. The rest of the equipment was placed on a shelter near the base of the tower, with available power supply and Internet connection.

The coastline profile limited the maximum angle of elevation (complementary to the angle of incidence) achievable through a reflection from the sea surface to 15°. In order to minimize the tropospheric effects and avoid problems with the tracking of the direct GNSS signals, the minimum satellite elevation accepted by the GOLD-RTR was set to 5°. Under these circumstances, the ground tracks of the reflected GPS signals reaches up to 5 km long, and the first Fresnel zone radius (projected over the surface) ranges from 89.2 to 456.5 meters depending on the elevation angle. A basic scheme of the geometrical aspects of the experimental scenario is illustrated in Figure 21. Starting at the end of October 2008, the complete process of formation and melting of sea ice was continuously monitored until mid May 2009. The collected GNSS-R datasets are publicly available for the scientific community at the web server described in Appendix B.

Figure 19.: [Left] Frontal view of the cliff (Godhavn) where the equipment was placed (location marked with a red dot). [Right] Godhavn's telecommunications tower. Pictures taken in October 2008, during the installation of the equipment for the sea ice campaign.

Figure 20.: Images of the antenna system mounted on the telecommunications tower, overlooking Disko Bay. Pictures taken in October 2008, during the installation of the equipment for the sea ice campaign.

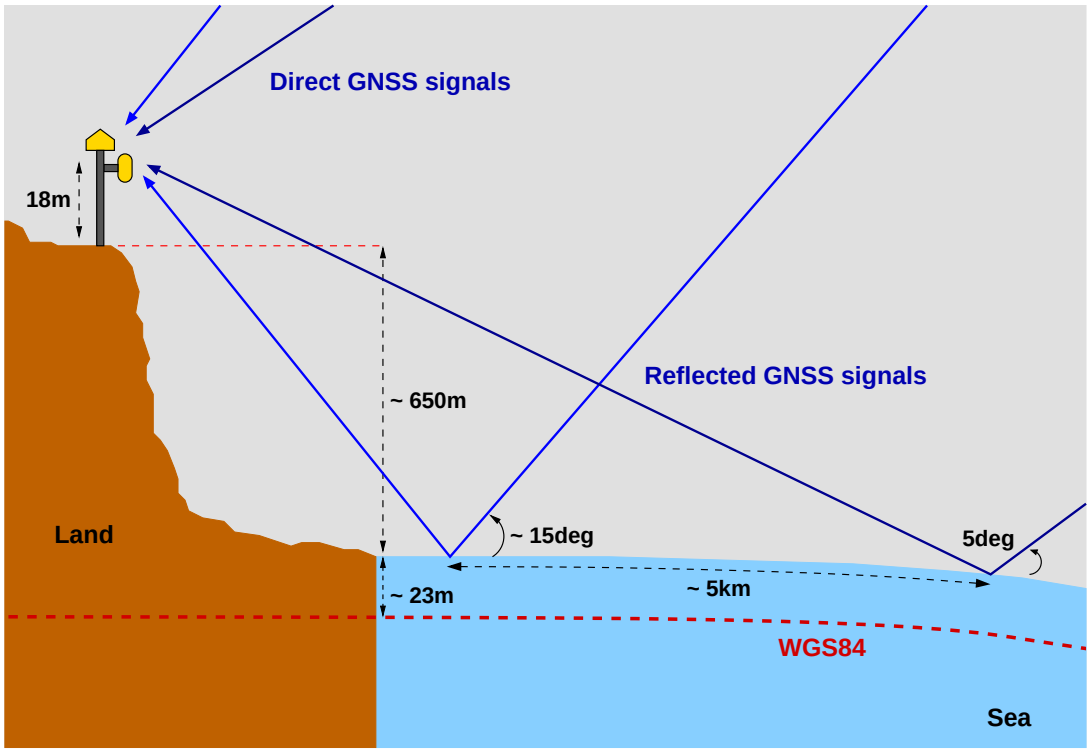

Figure 21.: Sketch of the geometry of the GNSS-R reflections over Disko Bay, Greenland. The equipments were installed on a communications tower, on a hill ∼650 meters high, at 2 to 3 km from the shore. The observations were mostly from the South (satellites towards azimuth South), and taken in the range of 5° to 15° elevation angles.

Location	Disko Bay, Greenland (69.27°N, 53.54°W)
Elevation range	From 5° to 15°
Azimuth range	From 120° to 215°
Height above surface level	$\sim$ 668 m
Ground track max. distance	$\sim$ 5 km
Campaign duration	$\sim$ 7 months (From 28/10/2008 to 16/05/2008)

Table 12.: Main characteristics of experimental campaign for remote sensing of sea ice.

Independent ancillary measurements were needed to verify the link between the GPS retrievals and the sea ice characteristics. These datasets can be taken in-situ or by means of remote sensing instruments, typically onboard a satellite, and may be direct measurements of a given aspect of the sea ice cover or not so directly dependent on it, such as weather condition, but still relevant for the analysis. The compilation of ancillary measurements taken in this experimental campaign is described in Appendix D.

Finally, a summary of the main aspects of this experimental campaign is given in Table 12.

3.2.2 COLLECTED SIGNALS AND ACQUISITION STRATEGY

During the sea ice campaign, the GOLD-RTR was configured to track the signals from up to 3 different GPS satellites in all the 3 Links –connected to Zenith-Looking (RHCP) and Horizon-Looking (LHCP and RHCP) antennas–, plus an additional satellite only through Link-2 –Horizon-Looking (LHCP)– to fulfil the 10 available correlation Channels. Therefore, when there was the appropriate visibility of transmitters, GPS signals coming from three satellites and their reflections over the ocean surface in both circular polarizations were processed in parallel (plus a fourth additional reflection). Since the receiver was in a static position, no Doppler or additional delays were added to the correlators and therefore, the resultant waveforms were centered in the acquisition window (lag 32). Examples of INT and RAW Data primary observables collected at Disko Bay (previously summarized in Table 11) are given in Figures 22 and 23 respectively. With a first look at these waveforms, two peculiarities stand out that will have an important impact on the analysis. The first one is the merging of direct and reflected signals on the resultant waveforms, which is due to the geometry of the scenario, where a complete separation of the C/A code ($2\rho_{\mathrm{C/A}} \simeq 600$ m) in the differential range delay from both signals cannot be achieved. The maximum separation is given by

$$\Delta\rho \simeq 2H_S^R \sin(\varepsilon_{max}) \simeq 346 \text{ meter} \tag{32}$$

with $H_S^R = 668$ m, the approximate vertical distance between the antennas and the ocean surface and $\varepsilon_{max} = 15°$, the maximum elevation angle. Note that the acquisition half-window is 480 meter long, therefore, the leakages of the direct signal captured by the Horizon-looking antenna will always lay within the observation. The use of a more directive antenna for getting reflected signals (properly oriented), would have overcome this problem with the price of limiting also the area of monitorization (in case of using a narrow-beam commercial antenna) or complicating the campaign's technical setup (by

building a dedicated antenna array and beamforming). Finally, it was preferred to use an omni-directional antenna and to dedicate more efforts in post-processing.

The second effect is related to the fluctuation of the reflected signal's peak from waveforms shown in Figure 22. After a comprehensive analysis, this variation revealed a clear dependency on the elevation angle. This type of behavior can be explained by the contribution of a multipath signal coming from a reflector close to the antenna. Assuming this hypothesis, it is possible to infer the nature of this multipath reflection from the resulting fringe pattern. In the case of horizontal planar-reflectors multipath and for a stationary surface, the fading rate ($d\Phi_M/dt$ in rad/s) sensed in the received signal is a function of the height of the antenna above the multipath-reflector (H_M) and the rate-of-change of the elevation angle (ε):

$$\frac{d\Phi_M}{dt} = 2k\frac{dH_M}{dt}\sin(\varepsilon) + 2kH_M\cos(\varepsilon)\frac{d\varepsilon}{dt} = \frac{2\pi}{T_M} \tag{33}$$

with T_M being its period. The fading strength indicates the level of reflection by the obstacle. In Greenland campaign's dataset, after checking several series of peak-power samples with respect to elevation angle from different satellites, an average height H_M of 13 meters was obtained, which approximately corresponds to the vertical distance between the Horizon-looking antenna and the metallic roof of the nearby shelters that can be seen on picture in Figure 19. Therefore, the collected reflections contain a variable component which is not related to any geophysical parameter and has to be taken into account for further analysis.

Finally, is important to mention that the power level sensed through Link-3 is lower than expected. During real-time remote monitorization, a loss of $\sim$6 dB was estimated by comparison with the preliminary results obtained trough Link-2. The reason behind this unexpected behavior was later discovered during the removal of the equipment from the experimental site at the end of the campaign, when it was found that the Horizon-looking antenna's connector for the RHCP output was not properly attached (thus increasing the insertion loss). This failure represents an important drawback for the analysis of the results later described in Chapter 4.

Regarding the acquisition strategy of the GPS reflections, the predicted orbits of the transmitting satellites (sp3 files (IGS, 2013)) were used to determine their visibility at every moment over a stretch of sea in the field of view of the antenna. The determination of the specular point is done by identifying the point over the EGM96 geoid such that the reflected signal fulfills Snell's law (the incidence equals the scattering angle) . Based on this visibility, the PRNs to be collected were selected in the GOLD-RTR's configuration. At the beginning of the campaign, after almost one month collecting data, it was determined that only observations closer to the central beam of the antenna were useful (enough SNR). A visibility mask with azimuth ranging from 110° to 220° and elevation from 30°/18° (depending on coastal line) to 5° was finally applied. The top panel in Figure 24 shows 24-hours of reflection tracks obtained under this configuration. Amplitude waveforms –INT data–, non-coherently integrated for 1 second, are the only data stored for those visible PRNs within the azimuthal mask, continuously 24/24 hours during the whole campaign. The selection procedure was automatically done, to predict the visibility and generate/update the configuration files accordingly to the latest GPS orbit status information.

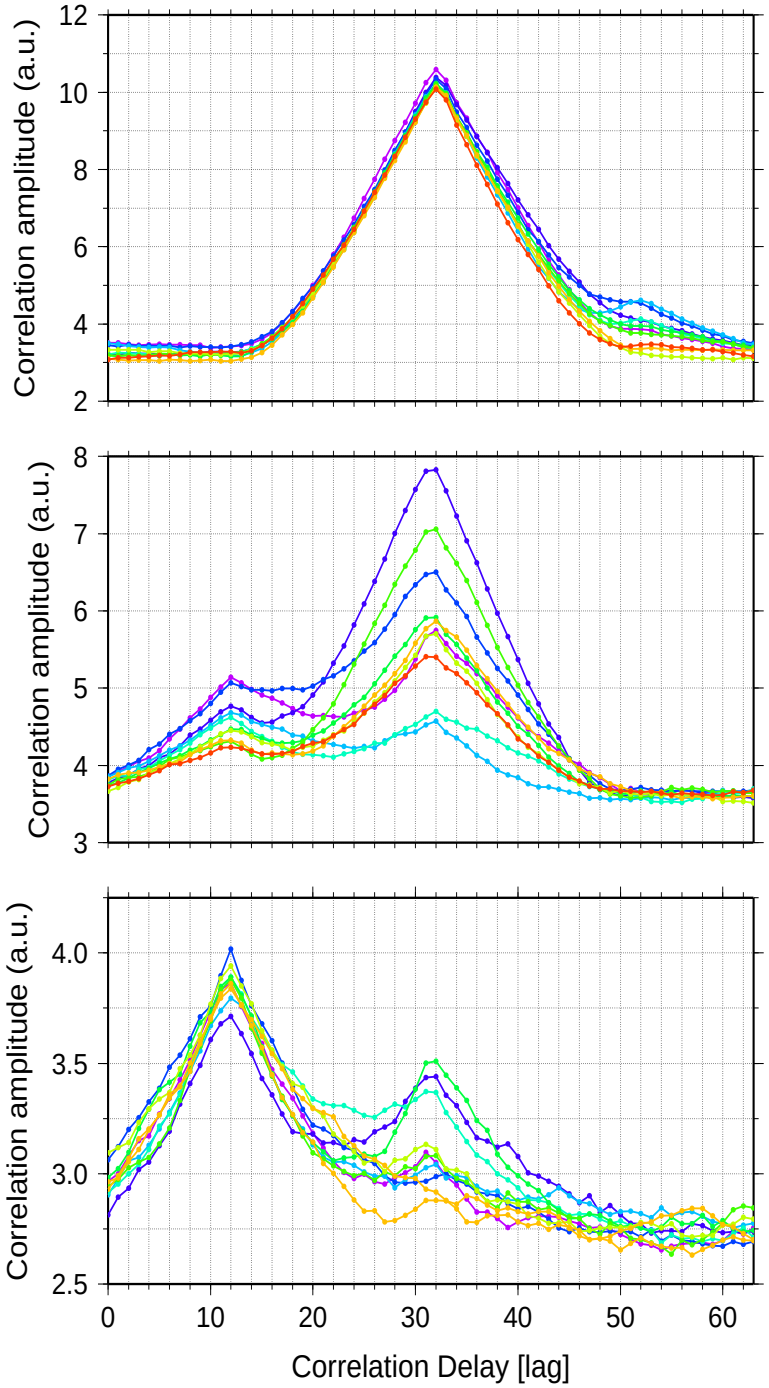

Figure 22.: Example of ten consecutive GOLD-RTR GNSS-R observables (1 sec of incoherent integration), collected during GPS-SIDS sea ice campaign: 64-lag amplitude waveforms for Zenith-looking (top), LHCP Horizon-looking (center), and RHCP Horizon-looking (bottom) links. The direct signal is also captured by the limb-oriented antenna. It corresponds to the early peak in both center and bottom panels. Moreover, the fluctuations provoked by the reflected signal can be also noticed in the top panel around lag 52. Data from PRN02 around $\sin\varepsilon = 0.22$ on March 1st, 2009.

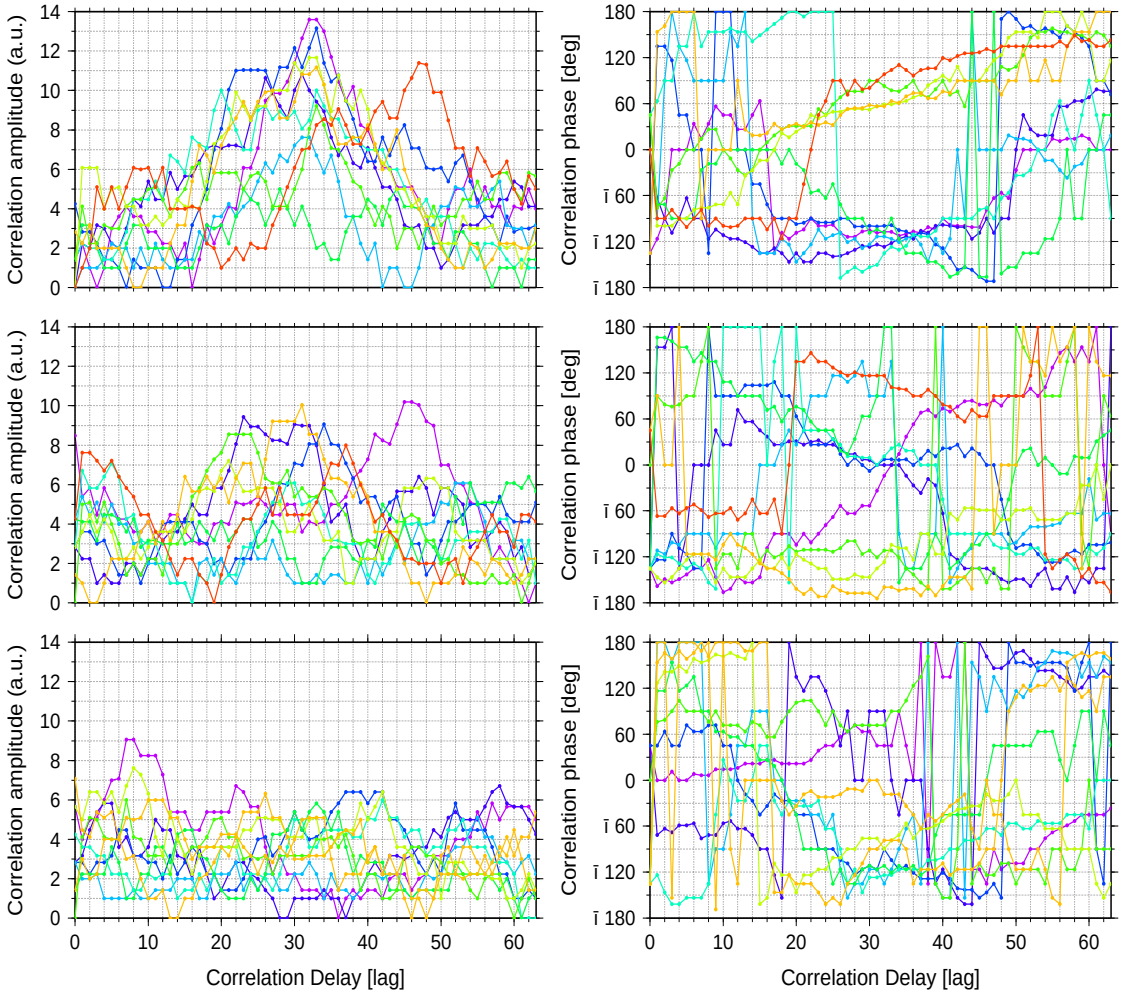

Figure 23.: Example of ten RAW data primary GOLD-RTR GNSS-R observables (1 ms of coherent integration) collected during GPS-SIDS sea ice campaign: 64-lag complex waveforms for Zenith-looking (top), LHCP Horizon-looking (center), and RHCP Horizon-looking (bottom) links. The complex values are given in amplitude (left column) and phase (right column). Data from PRN02 around $\sin\varepsilon = 0.22$ on March 1st, 2009.

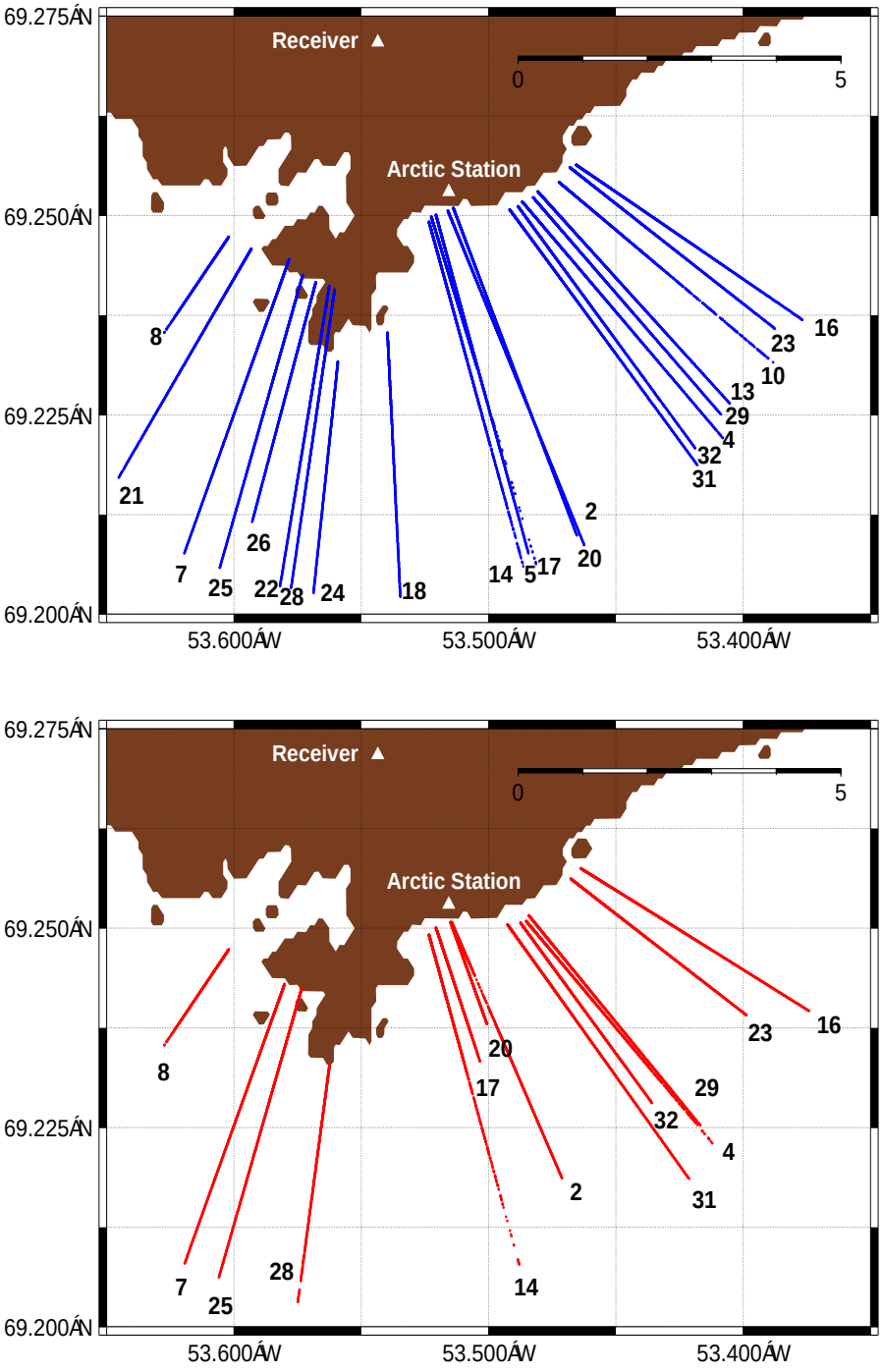

Figure 24.: [Top] Reflection tracks (location of the specular points) accumulated in 24 hours of INT observations (November 28 2008). [Bottom] Accumulated reflection tracks of RAW observations during the whole campaign. PRN numbers are indicated. Between 2-4 of them were collected every day. White triangles mark the location of the GOLD-RTR receiver and the Arctic Weather Station (details given in Appendix D.1).

In addition of this continuous set of 1-second integrated observations, 2 hours of RAW data were also stored every day, 10 to 12 AM GPS Time. This limitation was given by the storage capability of the terminal unit employed (with two hard disk drives of 500 GB –primary and redundant–). Despite of having Internet connection at the local setup, which allowed the real-time monitoring of the experiment, its restricted throughput did not tolerate the downloading of RAW observables. The bottom panel in Figure 24 shows the accumulated ground tracks from this type of data during the whole campaign, which means that only a few of them were visible during a single day. With the ongoing of the campaign it was found the possibility of storing additional RAW data. It was decided that rather than simply increasing the 2-hours time window of acquisition around noon, to directly collect the full visible track of a given GPS satellite for each day. Thus, starting December 22 2008, RAW data from PRN02 were also stored, and from March 5 2009, PRN20 was added. These PRNs have their ground track in the line of sight of the Horizon-looking antenna, achieving then the highest SNR.

As a summary, GPS signals reflected off the ocean surface at the surroundings of the receiver were collected continuously at two polarizations and incoherently integrated at 1-second. In addition a few RAW data tracks with phase information were also recorded at 1 msec rate every day. For a given satellite, the specular point of the reflected signal over the ocean surface travels a path defined as ground track (do not confuse with the projection of the GPS satellite at the Earth's surface). The geophysical information thus contained on that signal will be mainly related to the surface conditions at these points. While in the case of open waters we might consider as homogeneous the whole monitorization area of the experimental site, this assumption does not need to hold over sea ice, where changes in the ice cover can be expected along the 5 km ground tracks.

3.3 CAMPAIGN OVER DRY SNOW

Similarly as in Section 3.2 for the sea ice case, the purpose of this section is to provide a description of the different components required for the analysis of GPS reflectometry over dry snow that will be later developed in Chapter 5: scenario and data overview.

3.3.1 SCENARIO: DOME-C, ANTARCTICA

The experimental campaign was held in the Italian-French base of Concordia (Dome-C), located in the middle of the East Antarctic plateau (75.102°S, 123.395°E). The experience of several past campaigns (e.g. bedrock and snow topography, snow accumulation rate, etc.) as well as the different instruments developed in-situ for continuous atmospheric and snow measurements make this area very attractive for the calibration of any remote sensing mission. The snow surface has no significant topographic changes (near planar horizontal surface), without any obstacle along hundreds of kilometers, as it can be seen at pictures in Figure 25. Regarding L-band signals, a pilot ground experiment called DOMEX was conducted during the Austral summer of 2004-2005 (Macelloni et al., 2006, 2007). This experiment, that included radiometric L- and C-band measurements from a tower at different incidence and azimuth angles and snow measurements, confirmed the spatial uniformity (on a one-kilometer scale) and temporal stability (on a monthly scale) of the snow layers emitting low frequency microwave radiation. Therefore, strong variations in these snow layers that would justify a long-term campaign, with increased costs and technical requirements, were not expected. Our experiment then spanned from 10 to 21 December 2009, during maintenance tasks performed for the continuation of the radiometric experiment previously mentioned (now called DOMEX-2), that was held from December 2008 till December 2010 (Macelloni et al., 2009). The collected GNSS-R datasets are publicly available for the scientific community at the web server described in Appendix B.

The antennas were installed on top of metallic tower called *American tower* at 46 meter above the surface (Figure 26), while the rest of the equipment was placed on a shelter located on its base and in-situ operated by an IFAC member. The Horizon-looking antenna

Figure 25.: [Left] Italian-French base of Concordia (Dome-C), located in the middle of the East Antarctic plateau. [Right] Protected area of pristine snow near Dome-C. Pictures taken in December 2009, during the installation of the dry snow campaign.

Figure 26.: [Left] American tower, at Dome-c. [Right] Antenna system mounted on top of the American tower, overlooking a protected area of pristine snow. Pictures taken in December 2009, during the installation of the dry snow campaign.

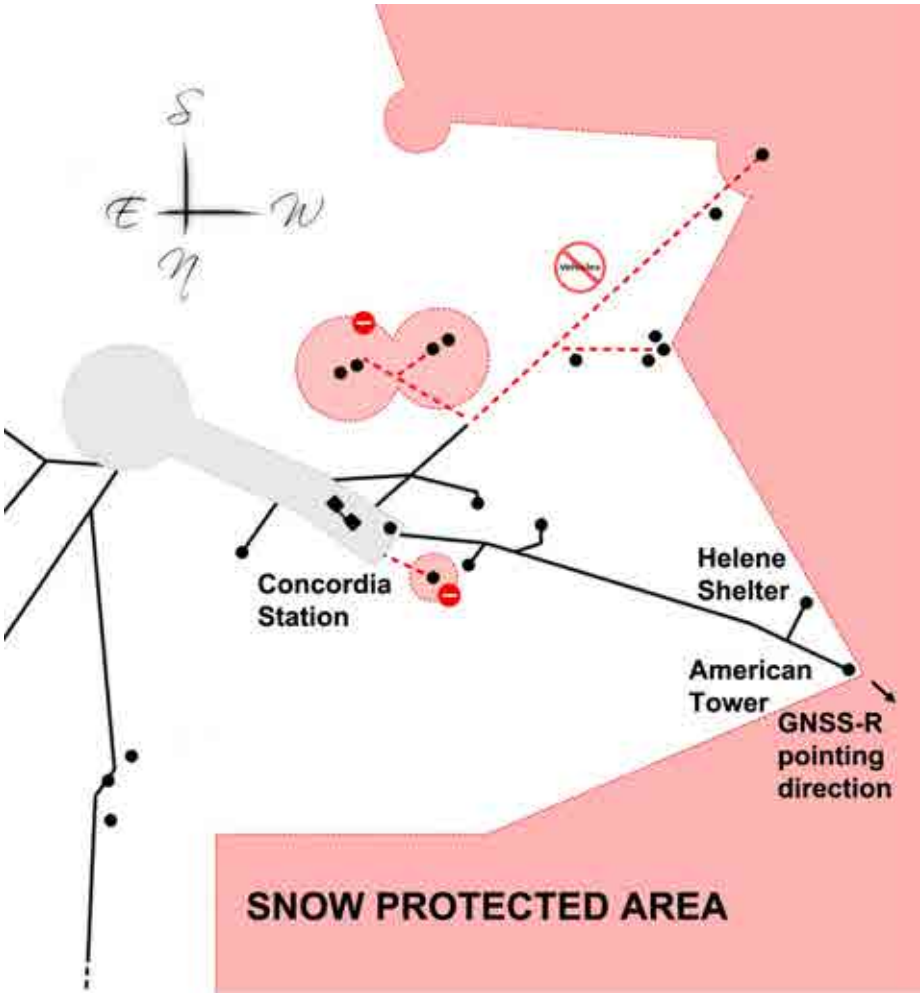

Figure 27.: Map of Concordia Base with American tower's location. The pink color shows the snow protected areas. The distance between Concordia Station and the American tower is 1 km.

was oriented towards North-West, monitoring a protected area (i.e. without human interaction) of pristine snow, as it can be seen on the map in Figure 27. The maximum angle of elevation of the GPS signals at these latitudes is $\sim 65°$. Like in the previous case (sea ice campaign), the minimum satellite elevation accepted by the GOLD-RTR was set to 5°. Under these circumstances, the ground tracks of the reflected signals over the snow surface reached up to 500 meters. A basic scheme of the geometrical aspects of the experimental scenario is illustrated in Figure 28.

Like in the case of sea ice, independent ancillary measurements were needed to verify the link between the GPS retrievals and the dry snow layers' characteristics. In this campaign, however, taking into account the broad experience of Dome-C as a calibration site for remote sensing instruments, all the ancillary dataset were obtained in-situ and are described in Appendix E. In particular, as described in Chapter 2, we know that dry snow is fully characterized by its density, since its real and complex permittivity components might be directly retrieved from this parameter. Therefore, the snow density profile measured from snow pits (first meters) and ice cores, will be the basic ground-truth

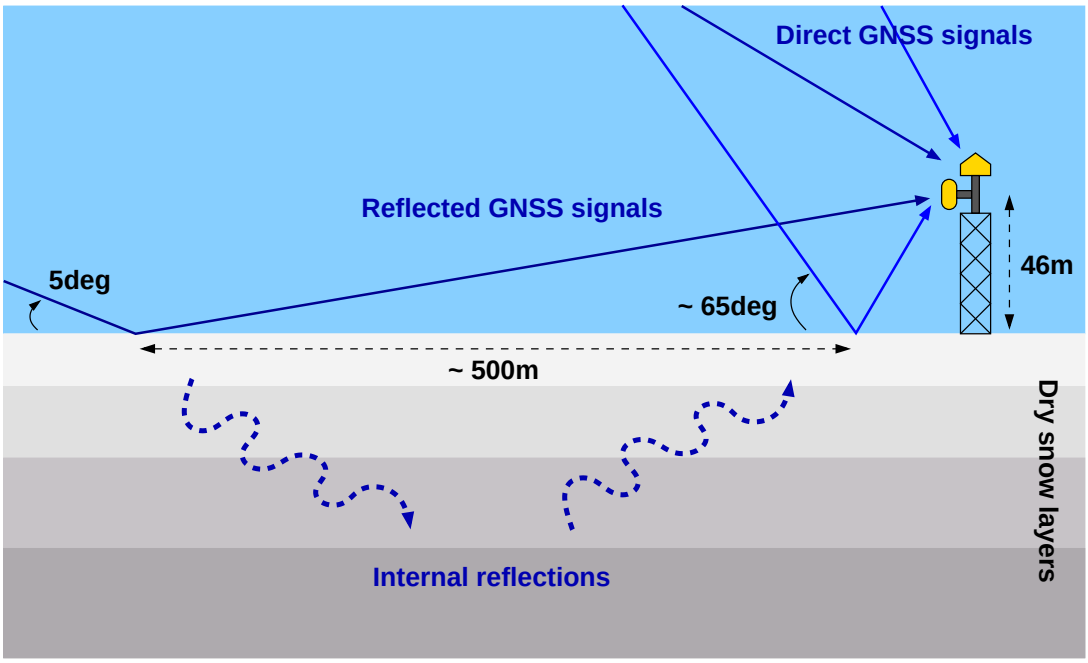

Figure 28.: Sketch of the geometry of the GNSS-R reflections over Dome-C, Antarctica. The antennas were installed on top of the *American tower*, 46 meter high. The observations were from North-West (limb-oriented antennas boresight pointing towards azimuth North-West), and taken in the range of 5° to 65° elevation angles.

Location	Dome-C, Antarctica (75.102°S, 123.395°E)
Elevation range	From 5° to 65°
Azimuth range	From −105° to 30°
Height above surface level	∼ 46 m
Ground track max. distance	∼ 500 m
Campaign duration	11 days (From 10/12/2009 to 21/12/2009)

Table 13.: Main characteristics of experimental campaign for remote sensing of dry snow.

employed for the analysis of GPS reflections later deployed along Chapter 5 (assuming horizontal homogeneity across the GNSS-R observation area). The resulting permittivity profiles, after applying Equations 22 and 23, are shown in Figure 29.

Finally, a summary of the main aspects of this experimental campaign is given in Table 13.

3.3.2 SIGNALS IN THE DATA

The configuration of the GOLD-RTR during the dry snow campaign was quite similar to the one employed in Greenland to obtain reflections over sea ice. Again, the full delay-maps (64 lags at 15 meter inter-lag delay) of the direct link, the reflected LHCP, and reflected RHCP were all simultaneously recorded for each visible satellite (up to three satellites simultaneously). Given the static conditions of the experiment, the Doppler

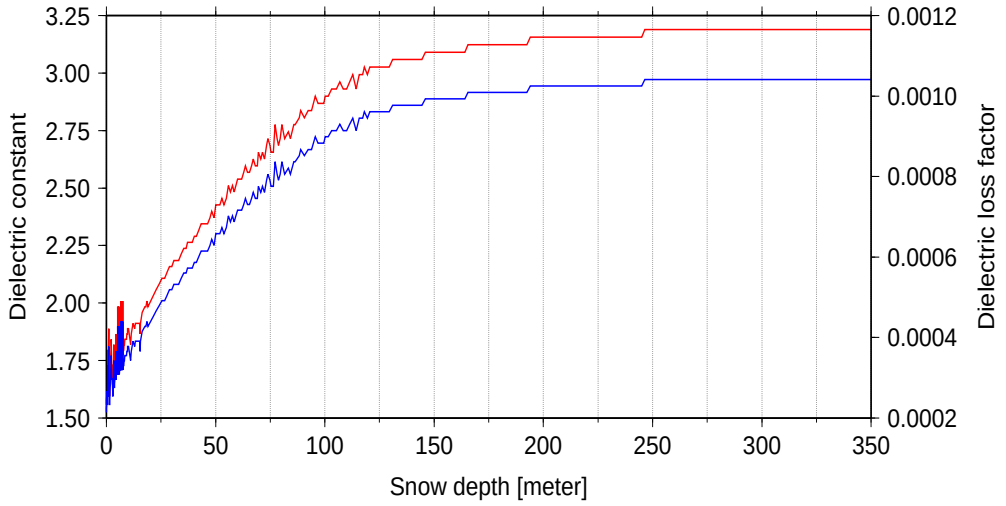

Figure 29.: Permittivity of the snow layers (its real part –dielectric constant– in red, blue for the imaginary one –dielectric loss factor–), based on their densities and the formulation given by Ulaby et al. (1990a).

maps did not give ancillary information, reason why only delay-maps were acquired one more time. In this case, however, given that the vertical distance between receiving antennas and reflective surface was even shorter (from ∼668 meters in Greenland to 46 meters in Dome-C, reducing then the ray-path distance between direct and reflected signals), all the correlators were applying tracking models corresponding to the direct signal (*Up* configuration), even for the reflected ones. An additional delay was applied in order to center the peak of the direct signals' waveform at lag 22 (10 lags prior to the center position, corresponding to 150 meters). By doing this, more room in the acquisition window was left for recording potential reflections from deeper snow layers, which will always arrive after the direct signal (on the right side of the delay-map). Examples of INT and RAW data primary observables collected at Dome-C (previously summarized in Table 11) are given in Figures 30 and 31 respectively. At a first glance, we can observe the presence of the direct signal through the three different links with apparently additional contributions coming not only from the surface level (around lag 27), but also from potential reflectors located at farther distances that, given the characteristics of the scenario (clean area of pristine snow), could only be explained by reflections due to permittivity gradients from deeper snow layers. This will be the main hypothesis of the analysis described in Chapter 5.

With respect to the acquisition strategy, there were no other limitations in the area of visibility rather than the minimum elevation accepted by the internal GPS receiver from GOLD-RTR (5°), the maximum elevation achievable by any GPS satellite at these Latitudes (∼ 65°), and the beamwidth of the Horizon-looking antenna (±60° in Azimuth centered at 315°). Figure 32 shows an example of the daily coverage of GPS reflections observed with our experimental setup at Dome-C. Once again, the predicted orbits of the transmitting satellites were used to determine their visibility and the specular point's location over the snow surface.

As stated in the previous section, the campaign's duration was significantly shorter for the case of Dry Snow: around 10 days. The stability of the snow layers and the high

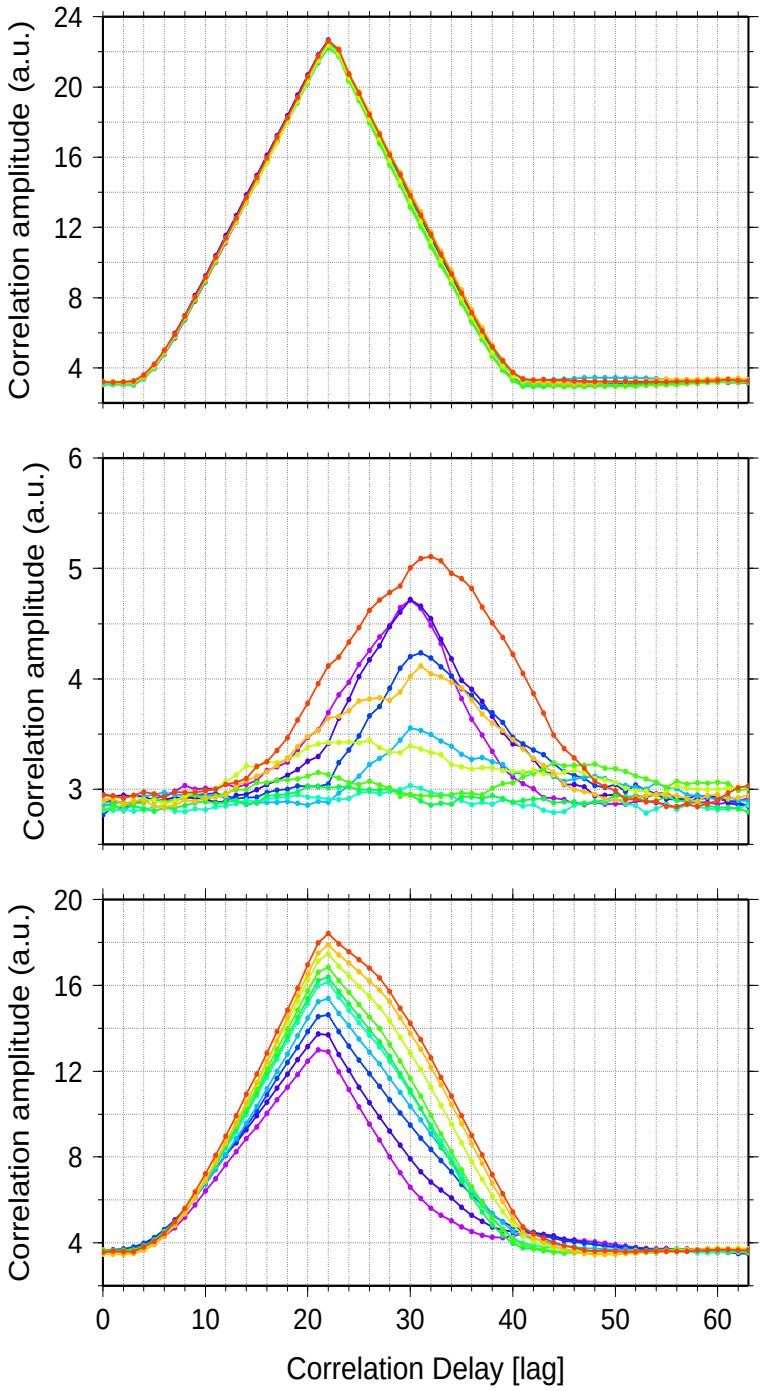

Figure 30.: Example of ten consecutive integrated GOLD-RTR GNSS-R observables (1 sec of incoherent integration) collected during GPS-SIDS dry snow campaign: 64-lag amplitude waveforms for Zenith-looking (top), LHCP Horizon-looking (center), and RHCP Horizon-looking (bottom) links. The direct signal is also captured by the limb-oriented antenna. The peak of the direct signal's waveform is centered at lag 22 in all the cases. Data from PRN19 around 45° on December 18th, 2009.

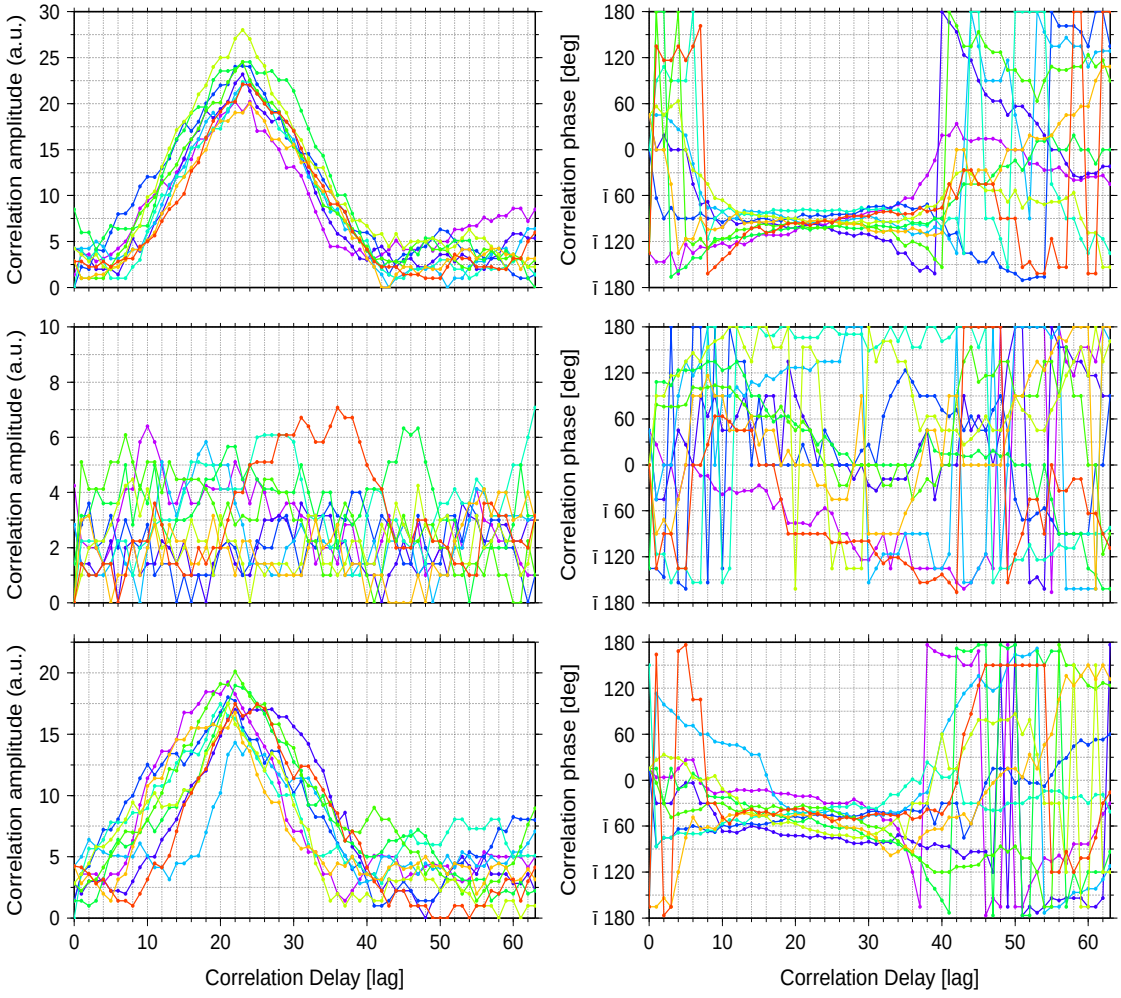

Figure 31.: Example of ten RAW data primary GOLD-RTR GNSS-R observables (1 ms of coherent integration) collected during GPS-SIDS dry snow campaign: 64-lag complex waveforms for Zenith-looking (top), LHCP Horizon-looking (center), and RHCP Horizon-looking (bottom) links. The complex values are given in amplitude (left column) and phase (right column). Data from PRN19 around 45° on December 18th, 2009.

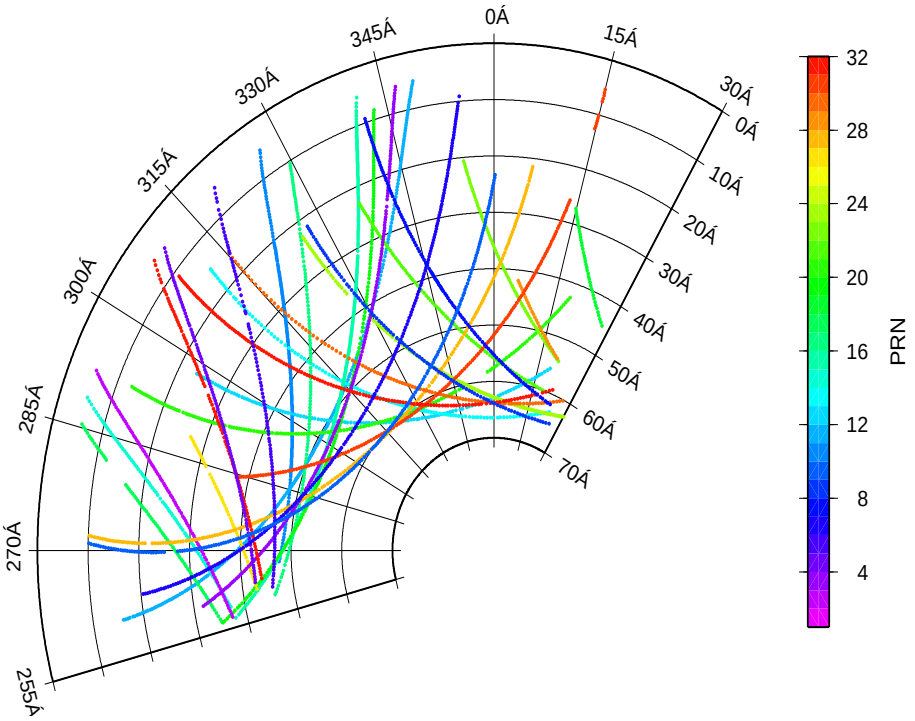

Figure 32.: An example of the daily coverage of GPS observations (location of the specular point) in polar coordinates (azimuth, elevation) at Dome-C, for December 16 2009.

cost for maintaining a long term experiment in Antarctica were behind this decision. In addition, real-time monitoring through Internet connection was not available. The equipment was operated in-situ by an IFAC member with support from ICE/IEEC by means of e-mail conversations (very size-limited) provided by satellite communications. During the first 5 days, the setup was under test in order the check the correctness of the installation and the configuration of the receivers. After that, from 16 until 21 of December, continuous collection of RAW data observables was successfully done.

Finally, as an introduction for the comprehensive analysis that will be later developed in Chapter 5, it is worth showing here how the waveform's amplitude evolved with the geometry. An example for a given satellite is reproduced in Figure 33 for certain delay-lags. The plots show that the amplitude is not homogeneous, but oscillates. The fluctuations build a pattern that repeats every day. General speaking, the main features also repeats for different delay-lags. Given the clean conditions of the installation in terms of nearby-multipath, this consistent variability of the amplitude with respect to the angle of elevation, supports the hypothesis of receiving several contributions reflected from different snow layers (down to more than 100 meters), where the relative phase of each component evolves also with the geometry at a different frequency. It is important to remark this fact because it points out the potential uniqueness of this scenario compared with other GNSS-R experiments, where only a single surface or a composition with just one additional layer is considered.

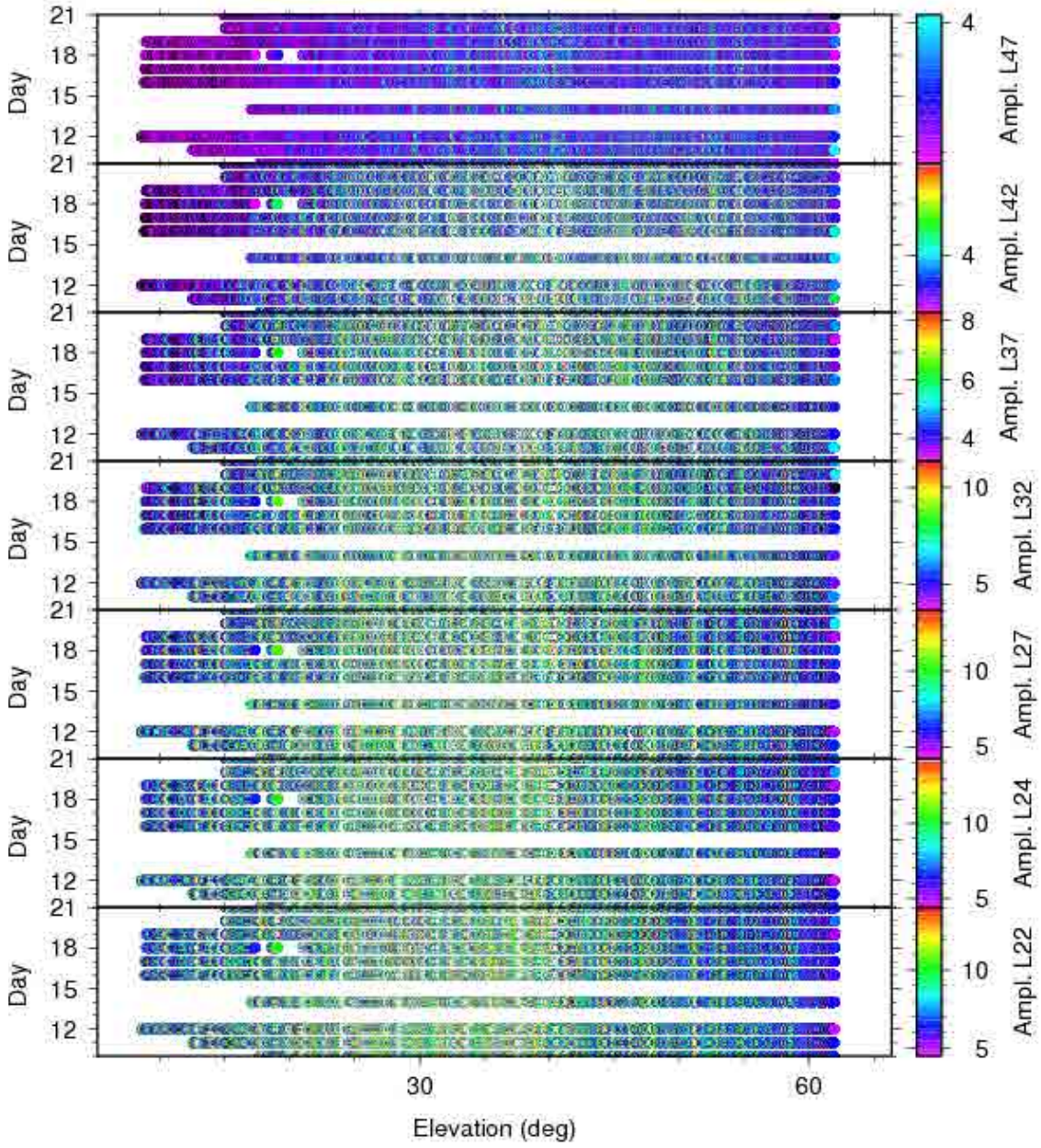

Figure 33.: An example of the evolution of waveform's amplitude for certain delay-lags from PRN07 during dry snow campaign (LHCP Horizon-looking antenna). The X-axis is the elevation angle of observation, the Y-axis is the day of campaign (day in December 2009), and the color scale is for the amplitude power (in GOLD-RTR units, from INT data). A graph is given for each of the following lags (down to up): 22, 24, 27, 32, 37, 42 and 47.

4

REMOTE SENSING OF SEA ICE

This Chapter analyzes the use of GNSS-R for remote sensing of sea ice. Section 4.1 spans the theoretical background presented in Chapter 2, to construct models to be applied in the datasets obtained during an experimental campaign carried on in Greenland. In such activity, GPS reflections were collected over an area of ocean surface where formation, evolution and melting of sea ice were monitored (campaign details given in previous Section 3.2). The applications investigated are: code and phase altimetry; roughness determination; and surface reflectivity. The results finally obtained are then shown in Section 4.2. Table 14 provides a list of publications issued from the study presented along this Chapter.

Most relevant **novelty** with respect to previous GNSS-R studies: **Polarimetric measurements (including phase) over sea ice at grazing angles.**

Title	**Reference**
Sea Ice remote sensing with GNSS Reflections	Fabra et al. (2009)
Monitoring sea ice and dry snow with GNSS reflections	Fabra et al. (2010)
Detection of Arctic Ocean Tides using Interferometric GNSS-R Signals	Semmling et al. (2011)
Phase Altimetry with Dual Polarization GNSS-R over Sea Ice	Fabra et al. (2011b)
GNSS Reflectometry for the remote sensing of sea ice and dry snow	Fabra et al. (2011d)
On the Retrieval of the Specular Reflection in GNSS Carrier Observations for Ocean Altimetry	Semmling et al. (2012)

Table 14.: List of publications arisen from the work presented in this Chapter.

4.1 MODELING AND PROCESSING GNSS-R OVER SEA ICE: POTENTIAL APPLICATIONS

4.1.1 CODE ALTIMETRY

Figure 34 illustrates the altimetric concept applied in Greenland's scenario: the signal transmitted by a GNSS satellite at large distance (typically ∼20000 km) reaches the direct antenna through a ray path which is shorter than the path traveled by the reflected signal. The geometric delay between both ray paths depends on the altitude of the receiving antenna, the offset between the two antennas, and the elevation angle of observation:

$$\rho_{geo} = (2H_S^R + offset)\sin(\varepsilon) \tag{34}$$

The propagation effects suffered at the atmosphere are mostly common on both rays, therefore do not introduce any significant relative delay, except for those effects related to the atmospheric conditions below the altitude of the direct antenna (**differential troposphere** in Figure 34). The later will induce a tropospheric delay of the reflected branch with respect to the direct one. This and other effects that should be taken into account in the altimetric analysis, such as multipath and the Earth's curvature, will be further developed later in Section 4.1.2. For the moment, we will consider that they do not have a significant impact over ρ_{geo}.

In GNSS-R, code altimetry refers to the measurement of ρ_{geo} by means of the shape of the reflected waveforms in the delay-map. It was envisaged as the original application when the GNSS-R concept was first presented in Martín-Neira (1993). Notice that the real challenge here is to accurately determine the specular point of reflection along the waveform itself, since the raw position of the receiver is already known with standard GPS information and a first approximation of the surface level can be taken from models (e.g. EGM96 geoid or WGS84 ellipsoid). A first consideration, therefore, is that the width of the autocorrelation function of the code employed (inversely proportional to its frequency bandwidth) sets a limit to the precision that can be achieved. This property can be visualized by imaging the effect on a triangular function: the narrower the base, the easier to determine its peak's position. In the present work, only the public C/A code was available, with lower resolution than protected P and M codes.

A model of a waveform resulting from a correlation between a GPS signal reflected off an ocean surface and a clean replica of its corresponding C/A code was given in Chapter 2. We will assume that the reflective surface is characterized by its permittivity (ϵ) and roughness (MSS), so we can move from sea water to sea ice by modifying these parameters. If the surface is smooth enough, the shape of the reflected waveform would be the same as the direct waveform but shifted in the delay range, i.e. a triangular function (in amplitude) in the range domain with a base of $2\rho_{C/A}$, centered at the specular point, and affected by thermal noise and the receiver's filters (that basically would smooth the sharp transition around the peak). However, when the surface is rougher, scattered reflections are generated, and the reflected power is spread in the range domain starting at the specular delay.

Typically, altimetric applications using code-delay are based on fitting of a theoretical or empirical model to the whole reflected waveforms. Examples of this methodology can be found in Maus et al. (1998) and Amarouche et al. (2004), for standard radar; and

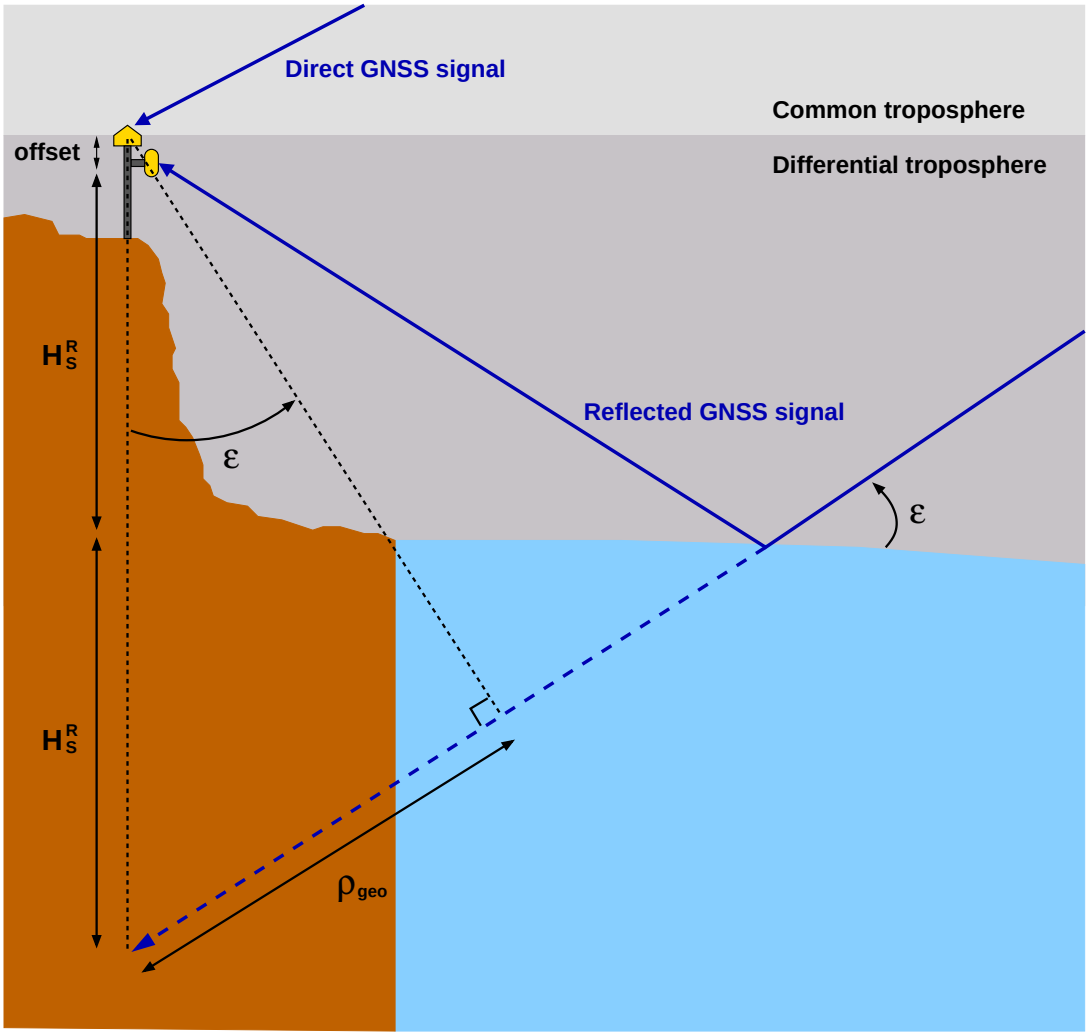

Figure 34.: Sketch of the altimetric concept: besides the geometric delay, given by the altitude of the reflection-antenna above the surface and the angle of elevation, the differential delay is also affected by the offset between the direct and reflected antennas and the troposphere below the direct-antenna. Other effects that may alter the altimetric observables are the multipath and the Earth's curvature.

in Lowe et al. (2002b), for GPS-R where the Zavorotny and Voronovich (2000) model is used. The main drawbacks of this approach are the high computational cost and the dependence on the model employed, which might require surface state –roughness– information (if the model itself is not used to solve this additional unknown). In order to overcome this limitations, the present study follows the approach presented in Rius et al. (2010). By taking the theoretical description of a bistatic system for ocean altimetry using GPS reflections from Hajj and Zuffada (2003) as a conceptual departure point, this paper formalizes the *retracking* of GNSS-R by means of the derivative of their waveforms, showing also algorithms to produce real time altimetric observables and the results obtained with real data from an airborne experiment. The basic idea is depicted in Figure 35 (obtained from Rius et al. (2010)). After considering the case of a waveform built as the limit of an infinite incoherent sum of equal triangles shifted in delay, the specular point (which determines ρ_{geo}) corresponds to the position of the maximum in the first derivative (delay= 0.0). Notice that this property is not achieved by the filtered version of the reflected waveform (thick line). Therefore, a very large bandwidth and high sampling rates are required in the receiver.

4.1.1.1 *Altimetric inversion*

Since code altimetry relies on the shape of the reflected waveforms, the continuously stored INT observables (incoherently integrated during 1 second) can be used for this purpose. The first step consists in locating the specular point along the reflected waveforms. Based on Rius et al. (2010), we assume that the position of the maximum of the first derivative provides this information. However, taking into account the peculiarities of the SI data-set described in Chapter 3, with direct signal contamination and low elevation angles of observation (two properties that impair a proper modeling of the reflected waveform), the position of the maximum in the waveform has also been analyzed for the altimetric purpose.

The integrated waveforms are then interpolated in the lag-space domain using FFT algorithms (zero padding in the transformed domain), and their first and second derivatives are computed using the following Fourier Transform's principle:

$$\mathcal{F}\{f'(x)\} = i2\pi kF(k) \tag{35}$$

After a first approximation of the location of the maximum in the extended waveform and on its first derivative (avoiding positions near the direct signal's peak), a polynomial fit is applied around these points over their respective derivatives (first and second). In order to avoid a discretized solution given by the extended sampling rate, the obtained polynomies are then solved by the Newton-Raphson method to finally get a more accurate location of the maximum in the waveform and on its first derivative as a secondary observables, defined from here as ρ_{MAX} and ρ_{DER} respectively.

From each satellite, time series of ρ_{MAX} and ρ_{DER} are gathered. Altimetry could be directly retrieved from these individual results with the elevation information provided by the internal GPS receiver by using Equation (34) (once corrected the *offset* between the antennas). However they show a rather high dispersion, as it can be seen on the bottom panel in Figure 36. In this example, without taking into account the outliers shown in the top panel, the evolution of the delay measurements follows a regression line with a width

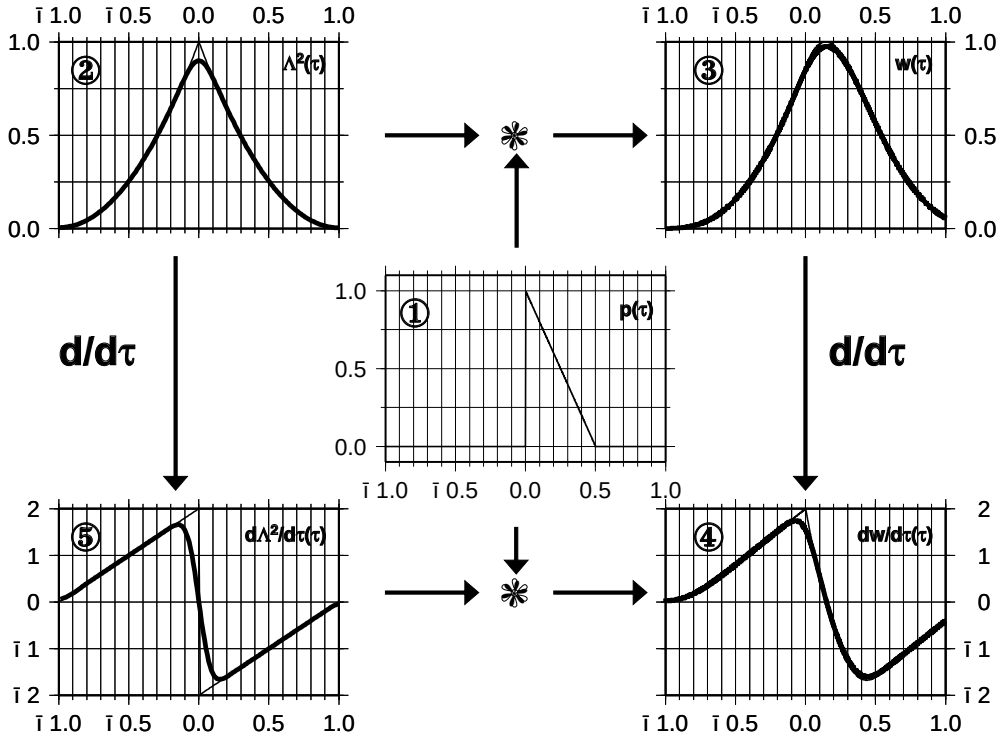

Figure 35.: Panel 1 represents the reflected power as a function of the delay relative to the specular delay (the same role as σ^0). Panel 2 represents the function $\Lambda^2_{C/A}(\tau)$ defined in Equation (5) as a thin line and its filtered version with a thick line. The resultant waveform obtained after convolution of Panel 1 and Panel 2 (similar process shown in Figure 11) is represented in Panel 3. Note that both versions are similar in shape and location of the maximum power. Panel 4 represents the derivative of the obtained waveform. The same results are obtained using the derivative of $\Lambda^2_{C/A}(\tau)$, as indicated in the path that includes Panel 5. Note that while the peak of the derivative for continuous sampling (thin line) corresponds to the location of the first power in Panel 1, the discrete sampling (thick line) slightly affects this retrieval approach. Figure from Rius et al. (2010).

of $\sim$ 10 meters, which in the given elevation range, would be translated into $\sim$ 42 to $\sim$ 112 meters in altimetry, which represents $\sim$ 13 meters of average error (approximating the standard deviation as the sixth of the dispersion's width). An important reason behind this bad behavior could be related to the fluctuations produced by multipath from near reflections and the contribution of the direct signal described in Chapter 3. In order to improve the altimetric retrieval, and especially for effectively decrease the impact of the outliers, the whole daily evolution of ρ_{MAX} and ρ_{DER} for each satellite as a function of $\sin(\varepsilon)$, corresponding to their *ground track* over the sea surface, is employed to get a single height result from the estimation of their slope. This approach is not only more robust against individual fluctuations in the reflected signal, but also against the biases derived from the bandwidth and sampling rate limitations of the receiver which are mentioned in Rius et al. (2010), since it does not rely on absolute values. However, the price paid is a lost of spatial resolution (increase of the footprint over the sea).

Figure 36 shows an example of the strategy finally followed for retrieving code altimetry. The evolution of the secondary observables ρ_{MAX} and ρ_{DER} with respect to elevation is given on the top panel (for one day and satellite). Both variables show a clear linear trend with, apparently, the same slope. The next step consists in subtracting them a model of ρ_{geo} computed from a first approximation of H_S^R. By doing this, the outliers can be easily removed by keeping only those values around a certain distance from their median. After a number of trials, it was found that their standard deviation was a proper choice for this interval. In addition, a quality control is applied by discarding those *outliers-free* data tracks that are too short ($<$ 100 samples) and thus can be strongly affected by multipath, or still have a high dispersion ($RMS > 10$ meters). Finally, a residual height (ΔH) can be obtained by applying a linear fitting to the remaining samples. The bottom panel from the aforementioned figure displays the observables ρ_{MAX} and ρ_{DER} from the top, once subtracted the model of ρ_{geo} and free of outliers, with the results of the linear fit applied. Notice how, by comparing the evolution of both observables, small differences in slope represent several meters in the estimated height for these elevation ranges.

4.1.2 PHASE ALTIMETRY

Sophisticated GPS receivers include carrier phase measurements in order to improve the position's retrieval (Spilker et al., 1996). The concept of phase altimetry with GNSS-R, more robust than the analysis of the envelope of the signal shown in Section 4.1.1, has been already proved from static positions (Treuhaft et al., 2001), and LEO altitudes using GPS radio occultation data from the CHAMP satellite (Cardellach et al., 2004). In addition, observations done by UK-DMC satellite (Gleason, 2005) indicated the potential use of the phase coherence of GPS signals reflected from sea ice.

4.1.2.1 *Estimation of the slope of the interferometric phase*

During RAW acquisition, complex waveforms from each of the three radio-link inputs are gathered for up to three different satellites simultaneously at a millisecond rate. For phase altimetry, only the values at the center lag of the waveform are taken. We call them direct (E_d) and reflected (E_r) fields when obtained from the direct and reflected

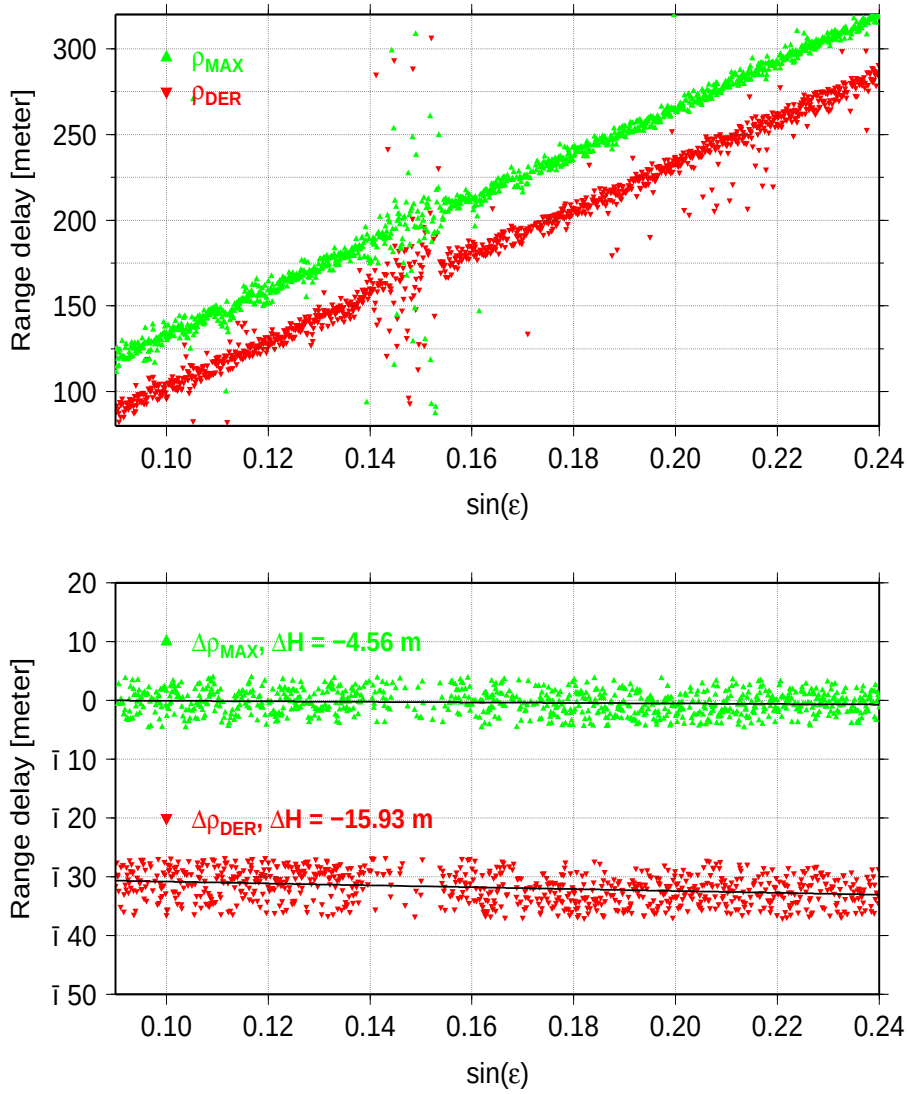

Figure 36.: Evolution of secondary observables for code altimetry as a function of $\sin(\varepsilon)$ from PRN 2 on 30/04/2009: [Top] ρ_{MAX} (green) and ρ_{DER} (red), [Bottom] residual versions of ρ_{MAX} and ρ_{DER} (a model of ρ_{geo} is subtracted and the outliers are removed) with the results of a linear fit applied and their corresponding altimetric inversion (ΔH).

waveforms respectively. The GOLD-RTR was configured to track the peak of the auto-correlation function by computing the delay needed using internal GPS information. At time t for a given satellite, we define the interferometric coherence-field, C_I, as:

$$\begin{aligned} C_I(t,sat) &= E_r(t,sat)\cdot E_d(t,sat)^* \\ &= |E_r(t,sat)||E_d(t,sat)|e^{i\phi_I(t,sat)} \end{aligned} \tag{36}$$

with

$$\phi_I(t,sat) = \phi_0(sat) + \frac{2\pi}{\lambda}\rho_I(t,sat) + \xi_\phi(t,sat) \tag{37}$$

where ϕ_0 is an undetermined and constant phase offset, λ is the electromagnetic wavelength and ξ_ϕ is the total phase error. The term ρ_I stands for the interferometric delay (in space-domain), which is the difference between the electromagnetic path length of the reflected (R_r) and the direct signal (R_d). In our scenario, ρ_I can be expressed as:

$$\begin{aligned} \rho_I(t,sat) &= R_r(t,sat) - R_d(t,sat) \\ &= 2H_S^R\sin(\varepsilon(t,sat)) + \rho_{curve}(t,sat) + \rho_{tropo}(t,sat) + \\ &\quad +\rho_{ant}(t,sat) \end{aligned} \tag{38}$$

where H_S^R is the vertical distance between the receiver and the reflection surface and ε, the elevation angle of the transmitter above the local horizon. Since the first term describes the path delay of a reflection off a flat-Earth surface, a correction for the Earth curvature is given by ρ_{curve}. The third term, ρ_{tropo}, stands for the difference in tropospheric path distance between the reflected and direct signals. No significant ionospheric correction was found in the GNSS-R dual-frequency receiver deployed in the same campaign (Semmling et al., 2011), so it has not been taken into account. Finally, ρ_{ant} refers to a time variable offset due to the projection of the distance between the antennas along the line of sight. Notice that ρ_I has a more realistic expression than its equivalent ρ_{geo} in Equation (34).

Having daily time series of C_I from several satellites as a fundamental observable, the altimetric value H_S^R can be estimated from the evolution of ϕ_I and a first guess of the interferometric delay ($\widehat{\rho_I}$). From their difference we define the residual interferometric phase ($\Delta\phi_I$), which is associated to a constant vertical distance (ΔH) that can be obtained from:

$$\Delta H = \frac{\lambda}{4\pi}\frac{d(\phi_I(t,sat) - \frac{2\pi}{\lambda}\widehat{\rho_I}(t,sat))/dt}{d(\sin(\widehat{\varepsilon}(t,sat)))/dt} \tag{39}$$

$$= \frac{\lambda}{4\pi}\frac{d\Delta\phi_I}{d\sin(\widehat{\varepsilon})} \tag{40}$$

$$\simeq H_S^R - \widehat{H_S^R} + \xi_{mod} + \xi_{phase} \pm \sigma_{\Delta H} \tag{41}$$

where $\widehat{\varepsilon}$ is the model of the elevation angle. In particular, $\widehat{\rho_I}$ is computed using Equation (38) with models of the different terms and $\widehat{H_S^R}$, which is a first approximation of H_S^R. The residual height estimate ΔH is extracted from the derivative of $\Delta\phi_I$ with respect to the sinus of the elevation angle, which is numerically determined using a standard least squares linear fitting approach (Press et al., 2007) over an extended segment of the ground track. Two error contributions impair the direct retrieval of H_S^R from ΔH. The first term, ξ_{mod}, accounts for the mismodeling of the time-dependent components of $\widehat{\rho_I}$,

whereas ξ_{phase} is the propagation of ξ_ϕ from Equation (37) into the linear fitting. The last term, $\sigma_{\Delta H}$, refers to the standard deviation of ΔH obtained at the linear fitting and gives a measure of the formal precision of the estimation.

Since the sensitivity of height retrievals lies in the determination of the slope of $\Delta\phi_I$, long and continuous interferometric phase series (ϕ_I) are needed. In addition, the impact of ξ_{mod} and ξ_{phase} has to be minimized. The first case requires a proper modeling of $\widehat{\rho_I}$ to be addressed in more detail in Section 4.1.2.2. For the second case we can define the contributions to ξ_ϕ as:

$$\xi_\phi(t, sat) = \xi_{fad/coh}(t, sat) + \xi_{mpath}(t, sat) + \xi_N(t, sat) \tag{42}$$

In Equation (42), $\xi_{fad/coh}$ accounts for the impact of fading and loss of coherence into the received signal. Fading effects introduce random phase departures in ϕ_I that will adversely affect the estimation of the derivative of $\Delta\phi_I$ over the ground track. The term ξ_{mpath} refers to the distortion of the signal due to multipath. The first data analysis showed a continuous multipath signal in ϕ_I with a mean period (called hereafter T_M) of ~ 70 seconds, which corresponds to a potential multipath reflector located about 13 meters under the antenna (matching with the telecommunication tower's height with respect to the metallic roof of the nearby shelters). The variable phase departures introduced by this multipath signal, which is present for the whole dataset, also corrupts the slope's retrieval. Finally, ξ_N accounts for the error due to instrumental noise. The data processing steps followed to reduce the impact of the different error terms from in Equation (42) are shown in Section 4.1.2.3.

As a last remark, notice that polarization effects in the phase, given by the dielectric properties of the reflection surface, do not have dedicated terms in Equations (37) and (42). In principle, we are assuming the same sea ice conditions for a single data track. Using expressions from Ulaby et al. (1990b) and experimental values of sea ice permittivity from Hallikainen and Winebrenner (1992), we obtain that the phase of the Fresnel coefficients for circular polarizations remains constant for our range of elevations. Therefore, ϕ_0 in Equation (37) contains this effect and will not have an impact on phase altimetry, which does not rely on absolute values. Moreover, this Fresnel phase does not change significantly for the different values of sea ice permittivity tested (< 0.15 rad). Then, small variations in the dielectric properties of the ice cover along the phase data track can be neglected in the altimetric retrieval. On the other hand, a sudden change due to a transition between thick sea ice and ocean water will have an effect that can be included in $\xi_{fad/coh}$.

4.1.2.2 *Delay model determination*

This Section describes the modeling of the different terms in Equation (38) required to compute $\widehat{\rho_I}$. The correct determination of this parameter reduces the effect of ξ_{mod} in Equation (41) for a correct altimetric retrieval.

1) Geometric delay

We estimate the geometrical characteristics of our system with the Cartesian coordinates of the transmitter, the receiver and a model of the Earth's surface. The GPS satellite's position was obtained from orbit and clock data provided by the International

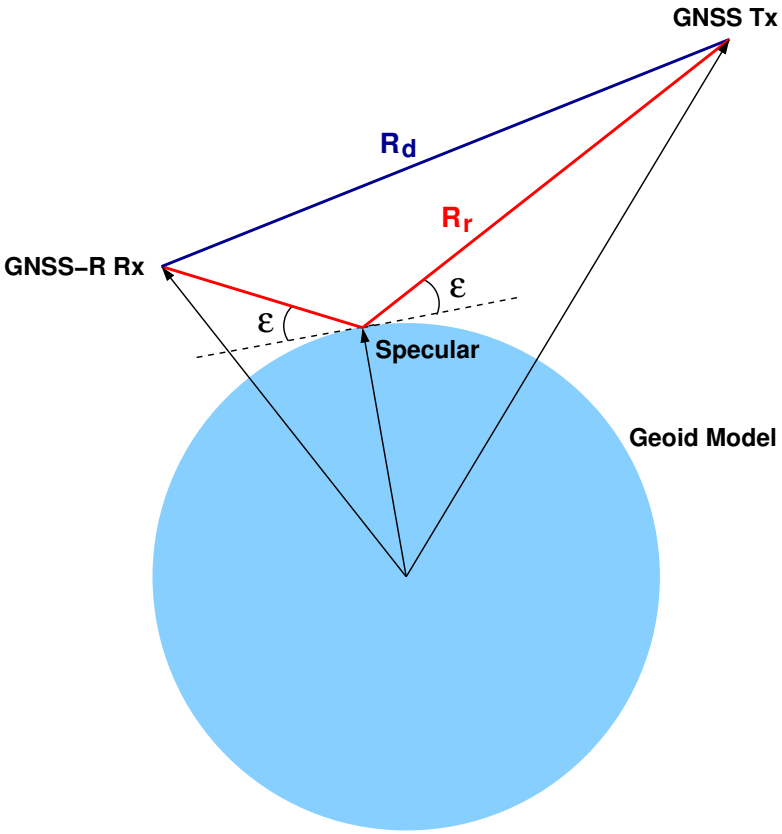

Figure 37.: The geometric model algorithm uses the position of the transmitter and the receiver to search for the point over the reference geoid (EGM96) in which the reflected signal would fulfill the Snell law (same incident and scattering angles). Once the specular point is found, the distance from the transmitter to the receiver (R_d) is subtracted from the sum of the distances between the transmitter-specular and specular-receiver (R_r) to obtain the geometric delay.

GNSS Service (IGS), whereas the precise receiver's location was computed by GFZ. We take the geoid EGM96 as a reference surface. After identifying the point over the geoid (specular point) such that the reflected signal fulfills Snell's law (the incidence equals the scattering angle), we compute the difference between the modeled direct and reflected paths, as depicted in Figure 37. Notice that, since the geoid takes into account the Earth's curvature, this is equivalent to estimate the first two terms in Equation (38), being $\widehat{H_S^R}$ equal to the vertical distance between the receiver and the specular point in a flat-Earth local system.

2) Offset delay

The offset delay $\widehat{\rho_{ant}}$ is computed as the projection of the real inter-antenna baseline distance $\vec{b}$ into the reflected path as a function of elevation and azimuth of the transmitter. A basic scheme is depicted in Figure 136. The experience from aircraft experimental campaigns, where, in addition, the different rotations in the local body frame (*roll*, *pitch* and *yaw* angles) have to be taken into account, allowed us to develop suitable algorithms to solve this problem. The general case is explained in Appendix F.

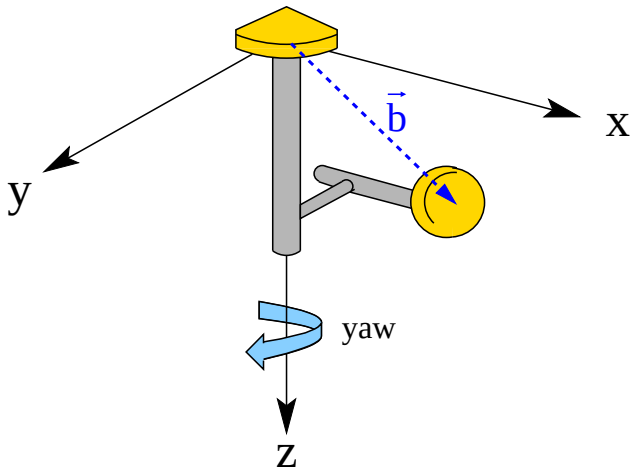

Figure 38.: Receiver body frame.

In Greenland's scenario, since the receiver is placed at a fixed position, the computation of $\widehat{\rho_{ant}}$ is simpler. Similarly to the aircraft body frame, we define a receiver body frame (Figure 38) centered at the reference antenna and with 1-axis pointing forward in the direction of the horizontal antenna, 3-axis pointing down and 2-axis forming a direct system. By using this, the same algorithms can be applied. In this situation, *roll* and *pitch* rotation angles are equal to 0, whereas *yaw* has a constant value given by the angle from North to the pointing direction of the horizontal antenna ($\psi_{BF} = 160.8°$). Local azimuth β and elevation ε of the transmitter are obtained from the satellite's position. Therefore the distance correction is computed as

$$\widehat{\rho_{ant}} = [e]^{T}_{\{XYU\}} \cdot Rot_z(\beta) \cdot T^{NED}_{ENU} \cdot Rot_z(\psi_{BF}) \cdot [b]_{\{xyz\}} \tag{43}$$

where Rot_z is a rotation matrix around z-axis in the local body-frame; T^{NED}_{ENU}, a transformation matrix from a East-North-Up to a North-East-Down system; and $\vec{e}$ a unit vector that depends on the elevation angle (all these terms are defined at Appendix F). The relative distance between the antennas was measured in-situ (values in meters):

$$[b]_{\{xyz\}} = \begin{bmatrix} 0.35 \\ -0.15 \\ 1.30 \end{bmatrix}$$

3) Tropospheric delay

The part of the atmosphere that lies above the reception antennas produces a delay which is common to both direct and reflected signals and cancels out. Assuming that the atmosphere has spherical symmetry, the differential tropospheric delay $\widehat{\rho_{tropo}}$ is twice the delay experienced between the specular point S and the reception antenna R.

$$\widehat{\rho_{tropo}} = 2(\rho^{S}_{tropo} - \rho^{R}_{tropo}) \tag{44}$$

An approximation of the approach used in VLBI and GPS geodesy is employed, where the tropospheric delay at a given position (P) is computed using the model (IERS, 2003):

$$\widehat{\rho_{tropo}}^{P} = m_{hz} \cdot D^{P}_{hz} + m_{wz} \cdot D^{P}_{wz} \tag{45}$$

where m_{hz} and m_{wz} are the hydrostatic and the wet mapping functions and D_{hz} and D_{wz} the zenith hydrostatic and wet delays. The term D_{hz} could be computed with high accuracy as a function of the atmospheric pressure at the receiver position, while the Total Zenith Delay (TZD, $D_z = D_{hz} + D_{wz}$) could be estimated from the standard geodetic process of the GPS data. With both measurements we could separate the wet and dry delay components and then compute the tropospheric delay $\widehat{\rho_{tropo}}$. However, in the present experiment , the Total Zenith Delay was computed above the receiver's location, D_z^R, and the available atmospheric pressure was measured near the sea level, from the Arctic Weather Station (both datasets detailed in Sections D.2 and D.1 from Appendix D). Therefore, the indicated separation between D_{hz} and D_{wz} was not possible. In the present analysis we thus need to assume that $m_{hz} \simeq m_{wz}$ and the atmospheric model reduces to:

$$\rho_{tropo}^P \simeq m_{hz} \cdot D_z^P \tag{46}$$

The hydrostatic Global Mapping Function (GMF) described by Niell (1996) has been initially used to calculate m_{hz}, a numerical function of the sinus of the elevation, the geographical coordinates of the receiver, and the day of the year. As a first approximation it behaves as $1/\sin(\varepsilon)$.

Finally, in order to compute ρ_{tropo}^S, an estimation of D_z^S is needed because there is no access to a GPS receiver at the specular point. To do so, it has been assumed that the variation of the total zenith delay goes with the altitude h as:

$$D_z(h) = D_z(0) \cdot e^{-(h/h_{scale})} \tag{47}$$

where h_{scale} is the scale height of the troposphere. In the present study, $h_{scale} = 7160$ meters has been taken. Finally, from Equations (44), (46) and (47); we can obtain an approximation to the differential tropospheric delay:

$$\widehat{\rho_{tropo}} = 2m_{hz}D_z^R \left(e^{\widehat{H_S^R}/h_{scale}} - 1 \right) \tag{48}$$

4.1.2.3 *Data processing*

This Section describes the signal processing steps to minimize the impact of ξ_{phase} in (41) and to infer an altimetric solution from the observables.

Once obtained the complex interferometric field (C_I), the first step consists in counter-rotating the 1-msec series of C_I with $\widehat{\rho_I}$ to bring the interferometric phase closer to base-band, which is equivalent to computing $\Delta\phi_I$ from Equations (39) to (40). Figure 39 shows an example of the evolution of the phase from the original direct and reflected fields, until the differential interferometric phase $\Delta\phi_I$ is obtained. After that, a coherent integration of 1 second is applied to raise the SNR, attenuating then the term ξ_N in Equation (42). In order to reduce $\xi_{fad/coh}$, the samples affected by fading and coherence loss need to be removed from the integrated field tracks. To do so, we compute the root mean square of the complex field's phase (RMS_ϕ) using a sliding window of length equal to the mean multipath period, T_M. Considering that fading effects introduce large random departures in the interferometric phase, we remove those samples with RMS_ϕ above a threshold given by:

$$min\left\{ \frac{2\pi}{6}, \overline{RMS_\phi} + (\overline{RMS_\phi} - min(RMS_\phi)) \right\} \tag{49}$$

where $\overline{RMS_\phi}$ and $min(RMS_\phi)$ account for the median and the minimum value of the RMS_ϕ track. This expression was obtained empirically after a number of trials. Finally, a box filter with a period of the multipath signature, T_M, is applied to the remaining series of complex samples to reduce the impact of the multipath (ξ_{mpath}).

The altimetric solution is inferred from the phase of the resultant complex series and the modeled geometry. Standard approaches are used to unwrap the whole track of phase samples and then to estimate the slope of each of its continuous intervals. For a N-samples interval:

$$\Delta\vec{\phi}_I = \begin{bmatrix} \Delta\phi_{I,1} \\ \Delta\phi_{I,2} \\ \vdots \\ \Delta\phi_{I,N} \end{bmatrix} = \begin{bmatrix} 1 & \sin(\widehat{\varepsilon})_1 \\ 1 & \sin(\widehat{\varepsilon})_2 \\ \vdots & \vdots \\ 1 & \sin(\widehat{\varepsilon})_N \end{bmatrix} \cdot \begin{bmatrix} a \\ m \end{bmatrix} = A \cdot \vec{x} \tag{50}$$

where $\vec{x}$ is the solution vector, which includes a constant bias a (no physical mean) and the slope $m = \Delta H(4\pi/\lambda)$. That would be equivalent to compute the derivative of $\Delta\phi_I(\sin(\widehat{\varepsilon}))$ in Equation (40). The parameter ΔH is then obtained for each interval and satellite. We compute the height of the surface with respect to the reference ellipsoid WGS84 (ellipsoidal height, H^S_{ellip}) as:

$$H^S_{ellip} \simeq \widehat{H^S_{ellip}} - \Delta H \pm \sigma_{\Delta H} \tag{51}$$

where $\widehat{H^S_{ellip}}$ is the vertical distance between the reference surface used in Section 4.1.2.2 for the modeling of $\widehat{\rho_I}$ (geoid EGM96) and the reference ellipsoid at the specular point of reflection. Notice that this expression derives from Equation (41) neglecting the error terms and knowing that the difference between the actual height and its model, defined from R to S, goes in the opposite sense than when defined from S to the ellipsoid:

$$(H^R_S - \widehat{H^R_S}) = -(H^S_{ellip} - \widehat{H^S_{ellip}}) \tag{52}$$

4.1.2.4 *Systematic effects: troposphere and multipath*

The systematic errors of the height estimations are given by ξ_{mod} and ξ_{phase} in Equation (41). For the first term, we will assume that the most significant contribution comes from uncertainties in the TZD, ξ_{TZD}, when computing the tropospheric correction, $\widehat{\rho_{tropo}}$. By taking Equation (48) with $D^R_z = \xi_{TZD}$ and $m_{hz} \simeq 1/\sin(\varepsilon)$, which is an upper bound of the used m_{hz} in terms of rate (as later illustrated in Figure 42), we can obtain the following approximation for ξ_{mod}:

$$\xi_{mod} \simeq \frac{1}{2}\frac{d\widehat{\rho_{tropo}}}{d\sin(\varepsilon)} = 2\frac{\xi_{TZD}}{\sin(\varepsilon)^2}(1 - e^{+(\widehat{H^R_S}/h_{scale})}) \tag{53}$$

From (53), it can be found that a typical error in the TZD estimates at low elevations of the order of 0.5 cm produces systematic errors in the estimated heights between 1 and 5 cm. Notice that this would correspond to an error in the TZD affecting as a constant (homogeneously) the entire differential tropospheric layer during one segment of data, therefore it would not affect the altimetric retrieval (absorbed in parameter a in

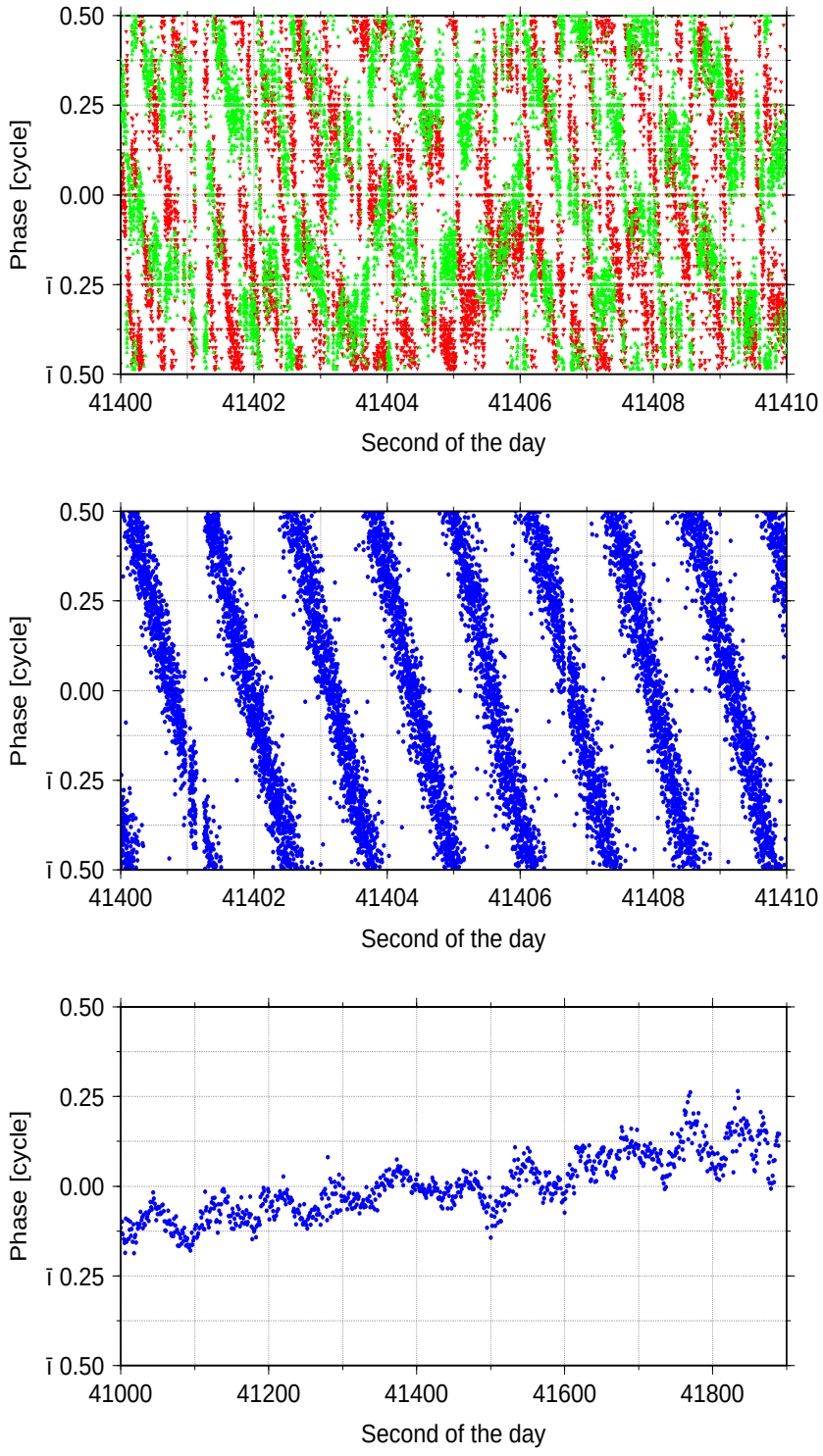

Figure 39.: [Top] 10 seconds of phase from the reflected (red) and direct (green) complex fields (E_r and E_d respectively), from time series of PRN07, January 25 2009. [Center] Phase of the interferometric field (ϕ_I) for the same batch of data. [Bottom] Resultant differential interferometric phase $\Delta\phi_I$ after counter-rotating the 1-msec series of complex fields C_I with $\widehat{\rho_I}$, and coherently integrating them up to 1 second. The time-axis is expanded to the whole track's duration. Notice the clear fluctuations produced by the multipath signal.

Equation (50)). However, inhomogeneities or time-evolution of the TZD will affect the results in the same way as the variations in height difference previously commented.

To quantify the impact of ξ_{phase}, we will assume that, after processing, this term is mainly dominated by the propagation of ξ_{mpath} from Equation (42). The period of the box filter used to minimize the effect of multipath, T_M, depends on the vertical distance between the receiver and the reflector level, H_M, as derived from Equation (33). The height of the telecommunication tower with respect to the metallic roof of the nearby shelters (13 m) was taken as a reference H_M. However, other multipath signals were also present in the data, especially at the lowest elevations and with longer periodicity. Due to this mismatch between periods, a residual multipath signal remains after the filtering step, which leads to systematic errors in the height results. In order to know their magnitude, we have modeled a multipath signal (in the phase domain) as:

$$\widehat{\xi_{mpath}}[t] = A_M \sin(2\pi t/T_M + 2\pi n/T_M) \tag{54}$$

with A_M and T_M the multipath's amplitude and period, and n the phase offset step. We have simulated then the height retrieval by summing $\widehat{\xi_{mpath}}$ to a straight line with a known slope and applying the processing steps described in Section 4.1.2.3. This simulation process has been repeated by modifying T_M from 50 to 90 seconds, and n from 1 to T_M for each period in steps of 1 second. Figure 40 shows the maximum systematic error, obtained by this academic exercise, for each interval of data simulated (with 1-sec of resolution) and for two values of A_M. The first value (1.485 rad) corresponds to the maximum amplitude allowed to get $RMS_\phi = 2\pi/6$ rad (the upper limit in Equation (49)), whereas $A_M = 0.84$ rad is computed from an average value of RMS_ϕ taken from the dataset (0.6 rad). Notice that this last value is still overestimated, since it assumes that RMS_ϕ is entirely driven by the multipath, while other sources might also contribute, as it will be discussed in Section 4.1.3.2. Nevertheless, as it can be seen in the previous figure, more than 320 samples are needed to keep the multipath-induced systematic error under 3 cm, which corresponds to a ground track of $\sim$ 1 km in our scenario.

4.1.2.5 *Experimental correction of the tropospheric delay*

A first analysis using ρ_{tropo} showed a clear dependency of the altimetric retrievals with respect to $\sin(\varepsilon)$, with an average decay of 1 meter in the final ellipsoidal height estimates within the range of elevations, as it can bee seen in Figure 41. This result is unrealistic result for the taken scenario. The several assumptions made for its computation along Section 4.1.2.2 suggest that ρ_{tropo} is the source of that error. Since a detailed tropospheric delay computation was out of the scope of this work, this residual dependency is removed by estimating an empirical correction to the mapping function from the dataset.

To do so, a polynomial fit over the first set of averaged height estimates is extrapolated to obtain a correction function for ρ_{tropo} depending on the elevation angle. The application of this function would be equivalent to using an empirical global mapping function. Fig. 42 shows a comparison between the hydrostatic GMF from Niell and the corrected empirical version required to overcome the limitations of the tropospheric delay modeling.

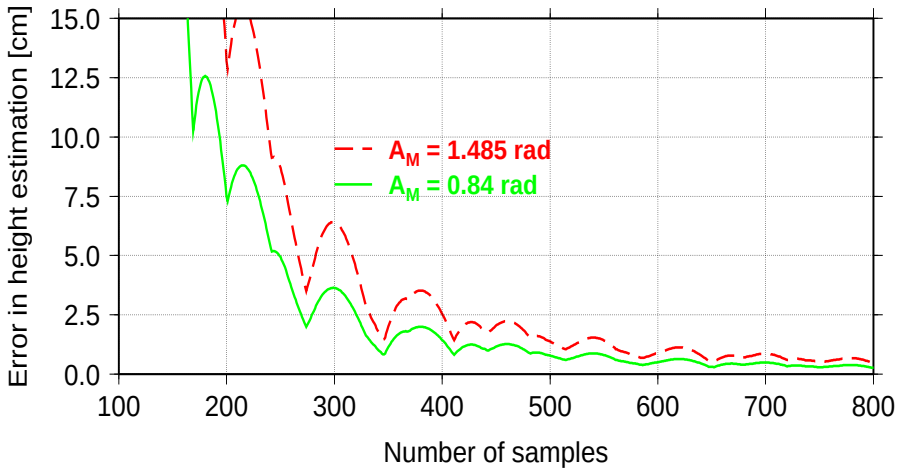

Figure 40.: Systematic error of the height estimations due to multipath with respect to the length of the data segment. Two multipath amplitudes (A_M) are simulated: 1.485 (red) and 0.84 (green) radians. Periods from 50 to 90 seconds in steps of 1 second have been used. Figure from Fabra et al. (2011b).

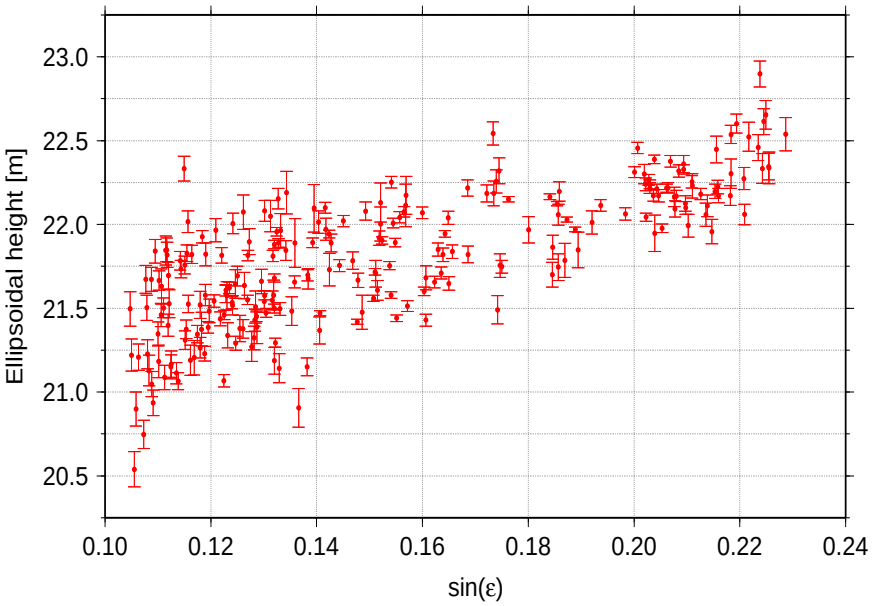

Figure 41.: First ellipsoidal height results obtained without empirical tropospheric correction as a function of $\sin(\varepsilon)$. A clear decay with the elevation angle can be noticed.

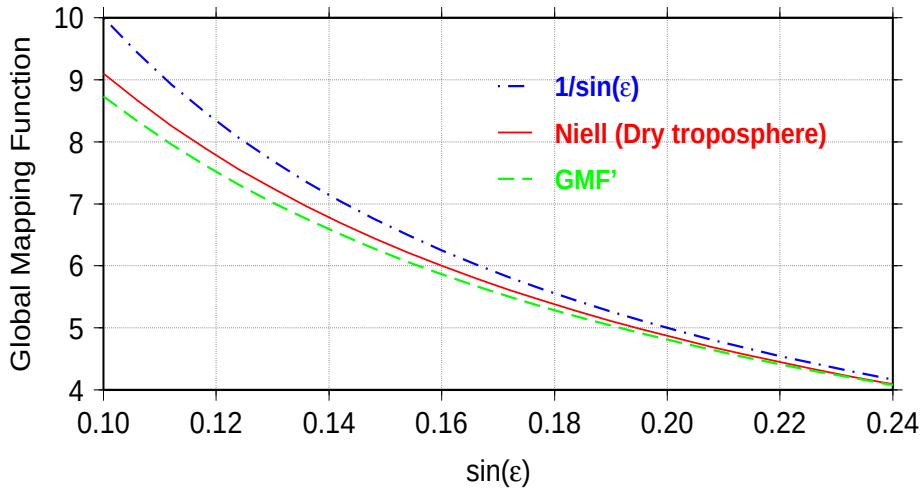

Figure 42.: Comparison of Niell's hydrostatic Global Mapping Function, $1/\sin(\varepsilon)$, and the empirical model employed (GMF') for a given date and location. The correction is needed to compensate the limitations in the computation of ρ_{tropo}. Figure from Fabra et al. (2011b).

4.1.3 ROUGHNESS DETERMINATION OF THE ICE COVER

From Chapter 2, we know that the reflection off a rough surface scatters the signals in a variety of directions, which reduces the power received at the specular direction (direction pointing towards the receiver, from the surface specular point). This, in turn, reduces the maximum power/amplitude of the waveform (weaker peak). This effect can be visualized as a redistribution of the power in both Delay and Doppler domains. Similarly, different surface dielectric conditions change the capability of the surface to reflect and absorb the incoming signal, also changing the peak power. This effect will be later analyzed in Section 4.1.4.

The use of GPS reflected signals for sea surface state determination has been widely studied (Komjathy et al., 2000b; Garrison et al., 2002; Cardellach et al., 2003), whose results include wind speed and wind direction (with some ambiguity) retrieval by means of theoretical models (Apel, 1994; Elfouhaily et al., 1997). The case of GPS roughness signatures towards sea ice remote sensing was presented in Belmonte et al. (2009). In this work, the GPS retrievals shown good agreement with measurements obtained with a LIDAR profiler, showing that these retrievals constituted a good indicator of the degree of structural roughening caused by deformation and erosion processes in the ice cover.

Similarly to the case of code altimetry described in Section 4.1.1, the typical procedure to retrieve roughness information is based on fitting a model of the waveform's shape to the data acquired. Again for this case, two different approaches with lower computational cost and focused on just a few delay-samples instead of whole waveforms will be analyzed in sections 4.1.3.1 and 4.1.3.2, which were specially motivated by the characteristics of the reflected signals received in our experimental scenario, with strong multipath and direct signal contamination, that impairs a proper waveform modeling.

4.1.3.1 *Scatterometric delay analysis*

The scattering on rough surfaces shift the delay of the peak power, induced by the contributions reflected off facets located around and away from the specular area. The ray path traveled by those contributions are always longer than the specular one, and as a consequence, the shift in delay induced by them is always positive (peak more delayed than a reflection off the specular point). We call this offset the *scatterometric delay*, ρ_{scatt}. Good agreement between roughness retrievals obtained with this observable and wind speed measurements was already shown in Nogués-Correig et al. (2007).

In the GPS-SI data-set, the scatterometric delay is obtained from the INT waveforms as:

$$\rho_{scatt} = \rho_{MAX} - \rho_{DER} \tag{55}$$

where ρ_{MAX} and ρ_{DER} are the positions of the maximum on the waveform and the maximum on its first derivative as described in Section 4.1.1.1 for code altimetry, including the quality control for removing outliers and noise filtering (just before the altimetric inversion).

Typically, in aircraft experimental campaigns using the GOLD-RTR, ρ_{scatt} is employed to invert the mean square slopes of the sea surface, an statistical parameter that characterizes the Probability Density Function of the slopes. This is done using the KGO model, which shows general good agreement with the results provided by more realistic and

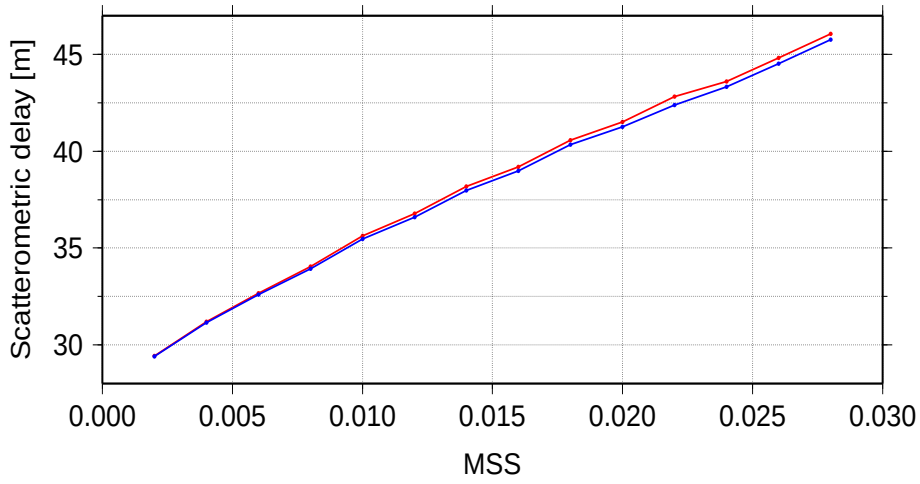

Figure 43.: Scatterometric delay ρ_{scatt} obtained from synthetic waveforms as a function of the roughness parameter MSS. Geometrical conditions as in Greenland's setup, but setting $\sin(\varepsilon) = 0.5$ and two dielectric cases: (red) sea water with T=5 and psu=35, (blue) sea ice with $\epsilon_{si} = 3.4 + i0.2$. The relationship between ρ_{scatt} and MSS is nearly linear. Given the small differences obtained when changing these permittivity values, the election of sea or sea ice in the waveform's modelling has no significant impact on the inversion of MSS from ρ_{scatt}.

complex models like KA and SSA for high angles of elevation. The inversion assumes that for a given geometry and dielectric properties of the surface, the scatterometric delay behaves linearly with the MSS. This is a fair approximation, as depicted in Figure 43, generated from modelled waveforms. The inversion procedure is as follows:

- For a given t time batch (usually between 1 and 10 seconds), the scatterometric delay of the INT waveform $\rho_{scatt}(t)$ is extracted.
- Geometric information corresponding to that batch-observation is injected into the model.
- A-priori dielectric properties have to be assumed (estimations or ancillary measurements), to set the permittivity in the model.
- The model is run three times for every time-batch: using an a-priori roughness parameter MSS_0, and a given MSS-increment ($MSS_0 - \Delta MSS$ and $MSS_0 + \Delta MSS$).
- Scatterometric delays from each synthetic waveform are then extracted: $\rho_{scatt}^{MSS_0}(t)$, $\rho_{scatt}^{MSS_0-\Delta MSS}(t)$, and $\rho_{scatt}^{MSS_0+\Delta MSS}(t)$.
- Finally, the linear inversion is conducted as:

$$MSS(t) = MSS_0 + \frac{\rho_{scatt}(t) - \rho_{scatt}^{MSS_0}(t)}{\frac{\rho_{scatt}^{MSS_0+\Delta MSS}(t) - \rho_{scatt}^{MSS_0-\Delta MSS}(t)}{2\Delta MSS}} \tag{56}$$

The main concern that impairs the application of the same methodology to Greenland's scenario is the lack of validity of our scattering models at such low angles of

elevation. Despite our algorithms are based on the KGO approximation (as in Belmonte et al. (2009)), more sophisticated models such as SSA (Voronovich, 1985) seem to have similar problems (Voronovich and Zavorotny, 2000). Therefore, we need to find an empirical way to perform a realistic roughness estimation of the sea/sea-ice surface from the observables gathered (ρ_{scatt}). The first step, then, consists in analyzing how the data behaves for different angles of observation. The top panel from Figure 44 shows the measurements of ρ_{scatt} obtained during the whole campaign from different GPS-R ground tracks around the line-of-sight of the Horizon-looking antenna. A clear dependency with the elevation can be noticed. To better illustrate this effect, a regression line is plotted, which has been computed using a standard linear fitting approach resulting in a slope of 15.13 meters ($\sin(\varepsilon)$ has no units). The bottom panel shows a normalized histogram of these results, once corrected with their linear regression, displaying a clear Gaussian distribution. If we assume that when decreasing the angle of elevation to its limit, reflected signals become nearly coherent (i.e. waveforms with more triangular shape), the term ρ_{scatt} should also tend to a minimum value (depending on the receiver's bandwidth and sampling rate); which is consistent with the preliminary results obtained.

Figure 45 shows the obtained evolution of ρ_{scatt} along with the models ($\widehat{\rho_{scatt}}$) computed using the KGO approximation for several roughness cases and under the same geometry (but increasing the elevation range). Only LHCP is considered. A proper election of roughness values is made to cover the wide variety of possibilities that can be expected in our scenario during the campaign's period, going from the minimum $MSS = 0.002$ (bottom solid line) measured in Belmonte et al. (2009) for new ice, until $MSS = 0.028$ (upper solid line), which, by means of the study provided in Elfouhaily et al. (1997), is related to maximums of wind speed of $\sim$17 m/s measured by QuikSCAT in absence of sea ice. We can see how this scattering model fails at lower elevations, where the estimated values of $\widehat{\rho_{scatt}}$ follow a rising pattern when approaching to zero degrees, which is opposite to the expected behavior. On the other hand, for elevations higher than $\sim 30^{\circ}$, the model enters into what we could define as "stable region", where the variation of $\widehat{\rho_{scatt}}$ is rather limited and KGO works well. This was shown in previous aircraft experiments using the GOLD-RTR over open ocean scenarios and the MSS could be properly inverted from the ρ_{scatt} in this region ($\varepsilon > 30^{\circ}$), achieving also good agreement with more sophisticated algorithms based in KA or SSA (provided by IFREMER). Two peculiarities stand out when comparing the real measurements taken in Greenland's campaign against the models in the "stable region": first, the cloud of delay-data values lies at a lower average level (around 5 m), and second, their slope trend does not correspond with the smooth variations of the model (almost planar). The question that remains then, is how to extrapolate the preliminary results obtained to the valid region provided by the scattering model, in order to perform a realistic roughness inversion. The chosen option is depicted with green dashed lines in the same figure. These lines represent, with respect to the real measurements of ρ_{scatt}, the positions of 0.1- and 99.9-th percentiles from their histogram (Figure 44), once added to their linear regression previously computed and extended until $\sin(\varepsilon) = 0.5$, where they remain constant. Notice how the levels marked within the "stable region" are consistent with the limits given by the expected range of roughness values provided by the model. A new "corrected scattering model" can be built up assuming the following hypothesis: for $\sin(\varepsilon) < 0.5$ and a given MSS, the parameter ρ_{scatt} decreases with the elevation at the rate obtained from the

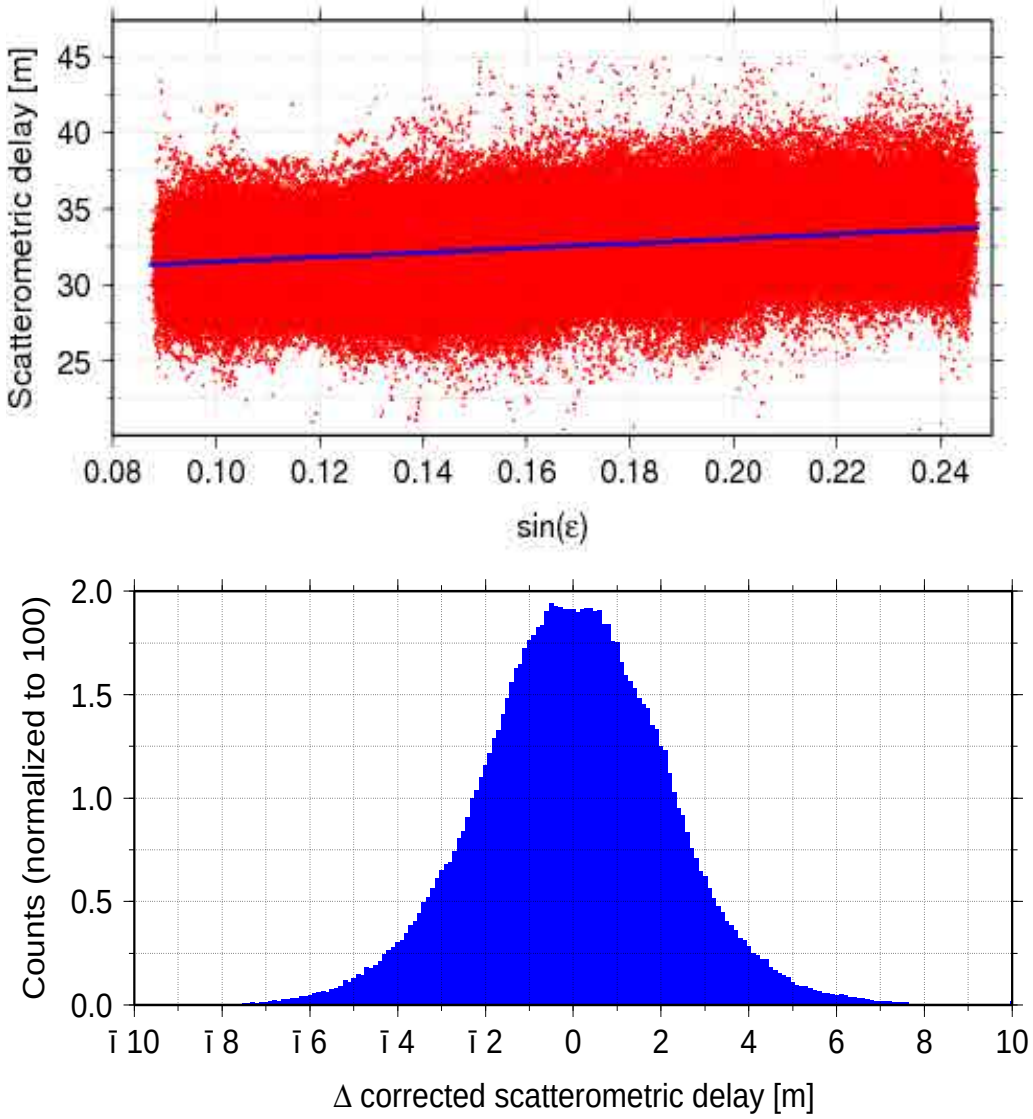

Figure 44.: [Top] Evolution of real measurements of ρ_{scatt} with respect to $\sin(\varepsilon)$ for the whole campaign's period. Only satellites with trajectories close to the line-of-sight of the Horizon-looking antenna are taken (PRN's 14, 5, 17, 20, 2 and 31). The linear regression of the results is plotted with a blue solid line. [Bottom] Normalized histogram of the results once corrected with their linear regression.

preliminary results, while it remains nearly constant at the "stable region" as estimated from the standard KGO-based scattering model. This correction provides a means for roughness inversion from Greenland's data-set using the procedure previously described. As a last comment, the expected variation of permittivity values in our scenario (from sea to sea ice) barely affect the results, as it has been already shown in Figure 43; therefore, the election of the a-priori dielectric properties of the sea surface is not critical.

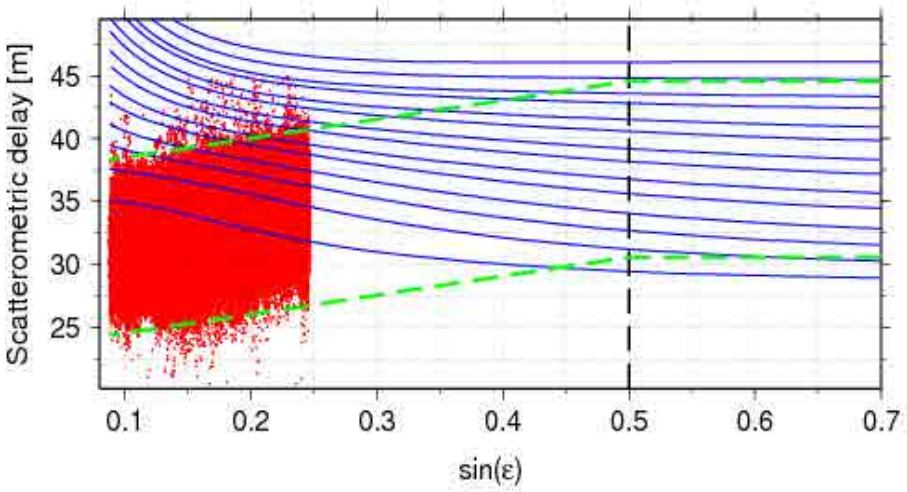

Figure 45.: Evolution of different delay variables with respect to $\sin(\varepsilon)$: real measurements of ρ_{scatt} (red dots), standard implementation of a KGO-based model (blue solid lines) and empirical correction obtained from the linear regression of the data for $\sin(\varepsilon) < 0.5$ (green dashed lines). For the KGO-based model, each line represents a roughness value (MSS), ranging from 0.002 (bottom) until 0.028 (top) in steps of 0.002, which correspond to the expected possibilities that may occur in the experimental scenario during the whole campaigns' period. The levels of the empirical correction are obtained from the positions of 0.1- and 99.9-th percentiles from the measurements' histogram shown in right panel from Figure 44.

4.1.3.2 *Dispersion of the interferometric phase*

The roughness of a surface can be measured also as the dispersion (e.g. RMS value) of its height level. Section 4.1.2 has described the theory behind and the processing steps employed to retrieve phase altimetry with the GPS-SI data-set. The altimetric technique consisted in subtracting height information contained in the interferometric phase (difference between direct and reflected signals) from RAW observables. In order to improve robustness and avoid the determination of instrumental and unknown phase offsets, the methodology retrieved the solution from the evolution of this interferometric phase ($\phi_I(t, sat)$) with respect to elevation (estimation of its slope) along continuous data tracks. However, the individual measurements are still directly related to altimetry. From Equations (37) and (38), we can obtain:

$$\phi_I(t, sat) = \phi_0(sat) + \frac{2\pi}{\lambda}(2H_S^R \sin(\varepsilon(t, sat)) + \rho_{corr}(t, sat)) + \xi_\phi(t, sat) \tag{57}$$

where ρ_{corr} is the sum of the different correction terms in Equation (38). Even though the term H_S^R is considered a constant, a more realistic definition would be a stochastic variable with a mean component ($\overline{H_S^R}$) and a standard deviation (σ_H) related to roughness of the surface. For the phase altimetric process, this second term is a source of noise. However, it might be a source of information of surface roughness.

Similarly to the process described in Section 4.1.2.3, we compute the root mean square of the interferometric phase ($RMS_\phi(t, sat)$) using a sliding window of length equal to the mean multipath period, T_M, once counter-rotated by a model computed from the solution obtained for H_S^R during the altimetric process (instead of a first approximation). The reason for doing so is twofold: –first– to remove the contribution of ρ_{corr}, and –second– to reduce the impact of the small variation of $\sin(\varepsilon)$ multiplied by the mean value $\overline{H_S^R}$ during the window's interval; or, in other words, to assure that the dispersion in the phase given by the interferometric delay terms from Equation (57) is only related to σ_H (or at least other contributions are minimized). Then, the relationship between RMS_ϕ and the RMS of this zero-mean residual height (RMS_H) is given by:

$$\begin{aligned} RMS_\phi^2(t, sat) \simeq & \left(\frac{2\pi}{\lambda} 2\, RMS_H \sin(\varepsilon(t, sat))\right)^2 + RMS_{fad/coh}^2(t, sat) + \\ & + RMS_{mpath}^2 + RMS_N^2 \end{aligned} \tag{58}$$

where there is a quadratic sum of RMS terms from several statistically independent –uncorrelated– factors. From Equation (57), we can see how ϕ_0 has no effect for being a constant; the altimetric part gets a similar expression, where RMS_H comes from the residual height (H_S^R minus its estimation) and ρ_{corr} is cancelled during the counter-rotation previously mentioned; and finally, three RMS terms result from ξ_ϕ corresponding to its components given in Equation (42). From these last terms, $RMS_{fad/coh}$ accounts for the impact of the random phase departures produced by fading and coherence loss, substantially increasing the value of RMS_ϕ when this happens. Note that this might depend on roughness (high values) as well. For the retrieval of RMS_H, values over the expected range will be considered affected by $RMS_{fad/coh}$ and will be filtered out. The term RMS_{mpath} refers to the distortion of the phase due to multipath. As it has been shown in Section 4.1.2.4, the multipath signal can be modeled as a sinusoid with period T_M and amplitude A_M. Therefore, RMS_{mpath} can be set to $A_M/\sqrt{2}$. After checking the whole dataset, it was found that $A_M \simeq \pi/8$ on average (it can be noticed on the bottom panel from Figure 39), so $RMS_{mpath} \simeq 0.278$ rad. Finally, RMS_N accounts for the error due to instrumental noise, which can be approximated as $|\arctan(1/SNR)|$, where SNR stands for the signal to noise ratio of the counter-rotated interferometric phasor C_I –in amplitude dimensions– after its long coherent integration (up to 1 second). We will assume that enough SNR is achieved with this process to make RMS_N nearly irrelevant for RMS_ϕ (for high values of SNR, $|\arctan(1/SNR)| \simeq 1/SNR$ rad). Notice that a high rough surface would also impair the benefits of a coherent integration, then rising the value of RMS_N. However, under these circumstances, RMS_H will be also high enough, then bringing RMS_ϕ to its upper bound (there is coherence loss). The analysis of the results will show how valid this statement is.

An important drawback of working with phase-based dispersion terms is that their domain of validity is determined by the single phase samples' range of values: $[0 : 2\pi)$. The top panel from Figure 46 shows the histogram of RMS_ϕ for the whole set of

measurements. An upper bound of $\sim \pi/2$ rad can be clearly distinguished. Actually, the histogram's shape shows a small increase of the population after ~ 1.4 rad breaking the decreasing tendency, marking the dispersion level where we can consider that there is coherence loss. In addition, the lower limit is in good agreement with the estimation made for RMS_{mpath} (from those cases where RMS_{ϕ} is entirely dominated by this term). The bottom panel from the same figure illustrates the RMS_H retrieved from the whole set of RMS_{ϕ}, assuming $RMS_{mpath} = 0.278$ rad and null values for $RMS_{fad/coh}$ and RMS_N in Equation (58). The color-pattern shows how RMS_{ϕ} propagates into RMS_H as a function of the elevation ($\propto 1/\sin^2(\varepsilon)$), as it can be derived from Equation (58). In particular, this dependency is clearly visible for the upper bound of RMS_H. Therefore, the applicability of this approach at L-band is mostly indicated for scenarios with low elevation angles of observation such as in our experimental case of study.

As a last comment, notice from Equation (58) that $\sin(\varepsilon(t, sat))$ is treated as a constant during the window's interval when computing RMS_{ϕ}. In spite of the small variation of the elevation in such interval, the impact of an error in the height estimation, which means a mean residual height (ΔH) different from zero after the counter-rotation of ϕ_I, has to be analyzed. We can model this situation by adding an additional RMS term to Equation (58) generated from a sawtooth wave of amplitude A_{res}:

$$A_{res} = \frac{2\pi}{\lambda} 2\Delta H \frac{T_M}{2} d\sin(\varepsilon)/dt \tag{59}$$

Therefore, $RMS_{res} = A_{res}/\sqrt{3}$ and, since $d\sin(\varepsilon)/dt \sim 0.000125$ and $T_M = 70$ sec, a maximum residual height of the order of 1 meter would represent a $RMS_{res} = 0.167$ rad (5 mm without the meter-to-radian $-2\pi/\lambda-$ conversion), while a more expected error in height estimation around 20 cm would divide this result by a factor of 5. We will neglect this effect for the retrieval of RMS_H.

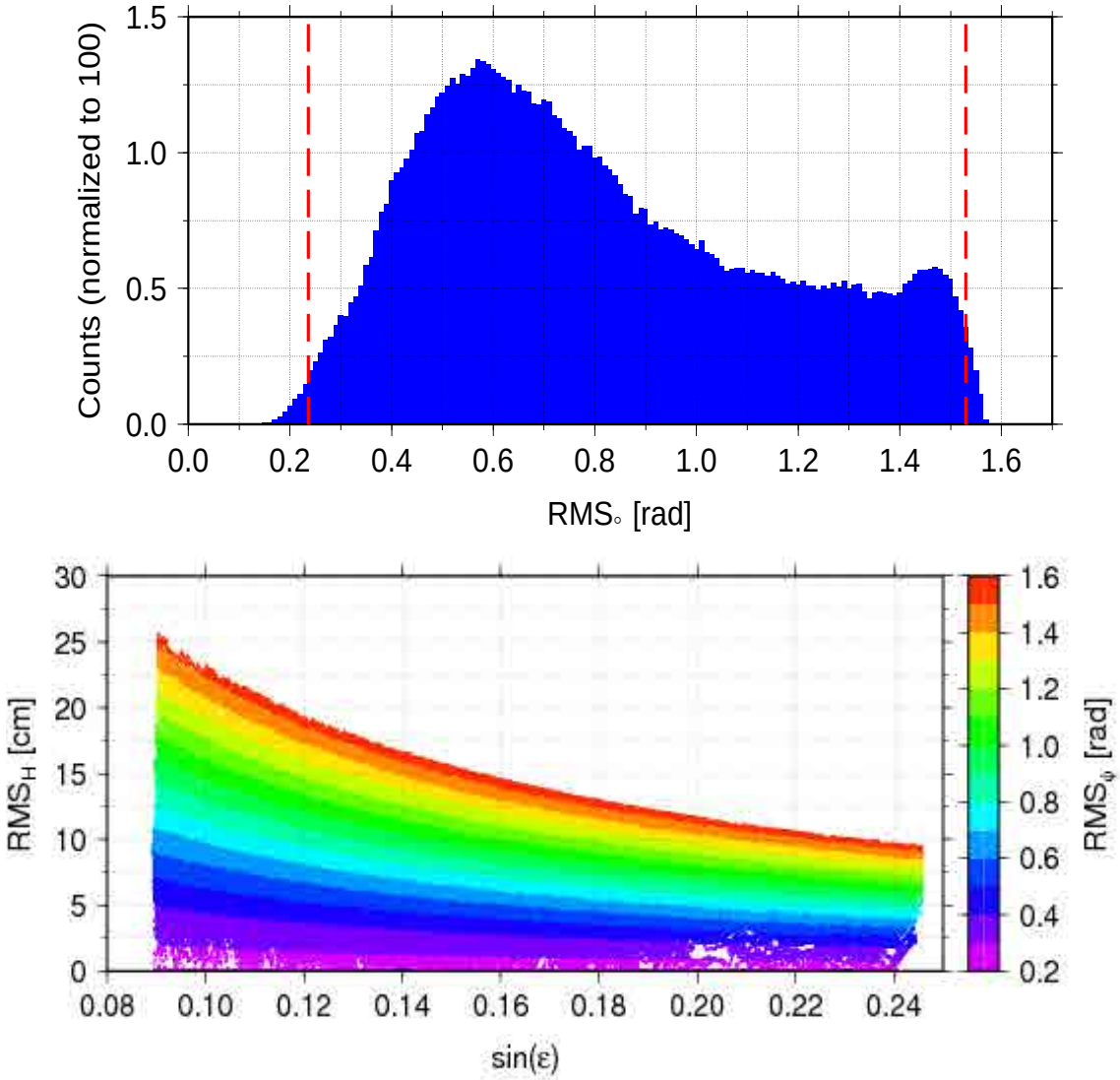

Figure 46.: [Top] Histogram of measured RMS_ϕ during the whole campaign. Two dashed vertical lines mark the estimated value for RMS_{mpath} (~ 0.278 rad) and the upper bound for a phase-based dispersion parameter, located around $\pi/2$ rad. [Bottom] Retrieved values of RMS_H during the whole campaign as a function of $\sin(\varepsilon)$. The color-pattern illustrates how RMS_ϕ propagates into RMS_H as a function of the elevation ($\propto 1/\sin^2(\varepsilon)$). An elevation-dependent upper limit is clearly noticeable, derived from the fixed upper bound in RMS_ϕ.

4.1.4 DIELECTRIC PROPERTIES' RETRIEVAL

The formation, evolution and melting of sea ice represents a continuous variation of the dielectric properties from the reflecting surface in our GNSS-R scenario. Table 15 shows the permittivity values for different types of ocean water and sea ice. From Chapter 2, we know that these changes, mainly provoked by variations in the salinity content, affect the reflected signal's power by modifying the backscattering coefficient (σ^0). This effect can be visualized in the evolution of the reflectivity Fresnel components from different types of ocean water and sea ice (First/Multi-year ice) shown in Figure 47. There is a clear distinction among both types of surfaces. However, young stages of sea ice, which do not have consolidated models of permittivity, show closer values to those from ocean waters (as illustrated in Figure 8 from results obtained in Belmonte et al. (2009)). Therefore, we will assume that intermediate steps of reflectivity will be reached by a mixture of both elements (specially during formation and melting of sea ice) and there is a continuous transition between both stages (ocean water and sea ice). Moreover, certain level of penetration through the thin sea ice layer (as expected by its dielectric properties) will allow the L-band GPS signal to reach the ice/water interface, thus favoring this hypothesis.

Regarding GNSS-R, Komjathy et al. (2000a) first showed correlation between the peak power of GPS returns and RADARSAT C-band SAR backscattered measurements over sea ice, thus showing the applicability of this technique for detection of this type of surface over ocean. More recently, similar results have been also achieved from space (Gleason, 2010). In Belmonte et al. (2009), scattered GPS waveforms proved to be sensitive to the state of the ice cover. In particular, changes in the estimated reflectivity demonstrated to be a good indicator of sea ice development stage.

There are two relevant aspects from the present study that represent an added value with respect to the previous work done: the low elevation range and the use of both LHCP and RHCP reflections. Higher angles of elevation are usually preferred for many reasons: less propagation of the signal through atmosphere, lower altimetric errors, more spatial resolution (due to smaller footprints), better fitting with known models, etc. By taking again a look to the top panel from Figure 47, we can see how under high elevation angles of observation, RHCP reflected signals are strongly reduced, so there are no practical reasons to collect them towards sea ice remote sensing purposes. However, the

Type	ϵ'	ϵ''	**Characteristics**
Sea water	73.42	56.07	Temperature = 15°C, salinity = 35 psu
	75.54	48.27	Temperature = 5°C, salinity = 35 psu
	79.02	33.73	Temperature = 5°C, salinity = 20 psu
Sea ice	3.75	0.39	$V_b = 70‰$
	3.39	0.19	$V_b = 30‰$
	3.12	0.04	$V_b = 0‰$

Table 15.: Relative permittivity values (real –ϵ'– and imaginary –ϵ''– parts) for different types of ocean water and sea ice at GPS-L1 frequency (1 GHz for sea ice). The dielectric properties are mainly determined by temperature and salinity in the case of open waters, and brine volume (V_b) in the case of sea ice.

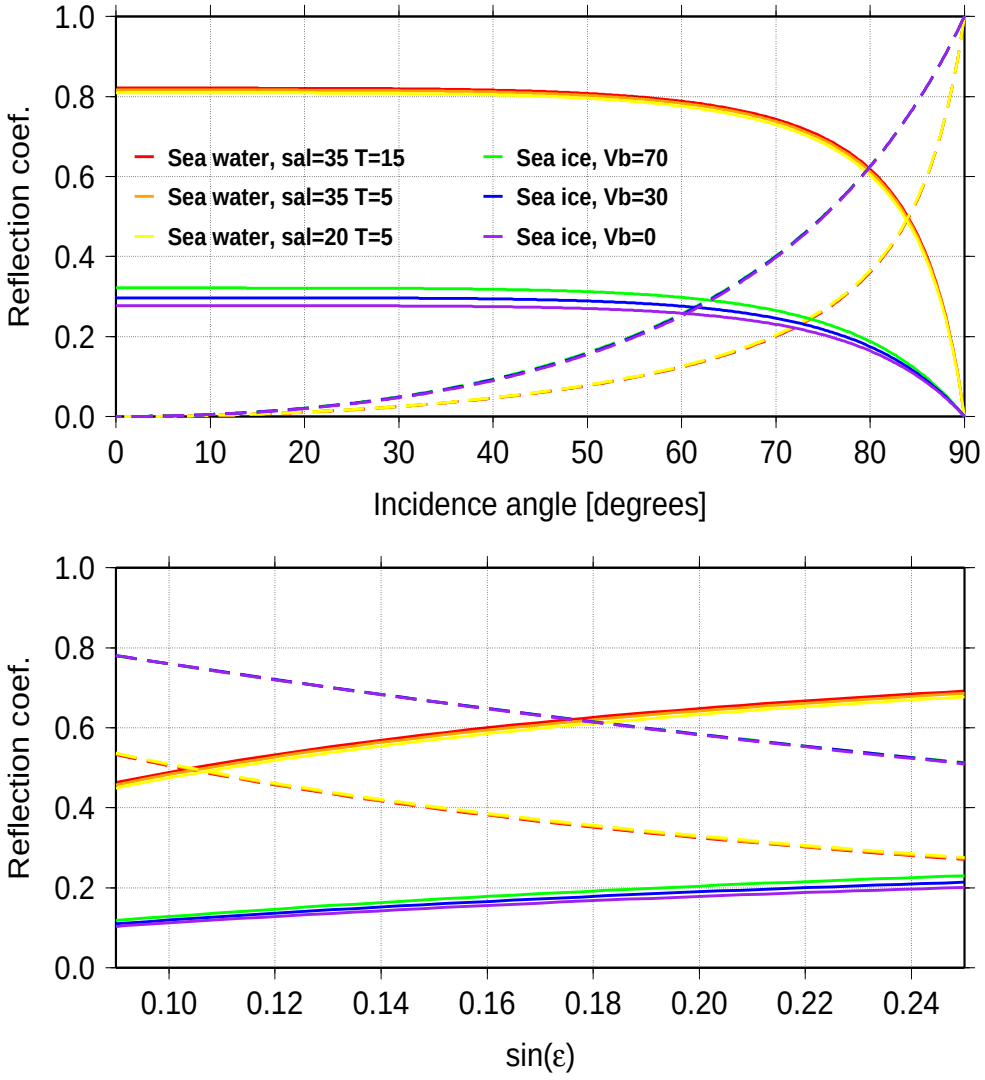

Figure 47.: [Top] Reflectivity Fresnel components for the different examples of sea water and sea ice from Table 15 with circular polarizations: co-polar –RHCP– (dashed line), cross-polar –LHCP– (solid line). [Bottom] Same values represented for $\sin(\varepsilon)$ within the visibility range of Greenland's campaign.

geometric conditions imposed in Greenland's scenario offers the opportunity to exploit around the **Brewster angle**, where both components of the circular polarization have similar levels (intersection between solid and dashed lines in the top panel from Figure 47). This allows to inspect different approaches based on dual-polarization measurements, that will be analyzed in Sections 4.1.4.1 and 4.1.4.2. The main advantage of such type of approach, given the symmetrical characteristics of the experimental setup (with the same antenna –plus pre-amplifier– and equal cables and front-ends for both reflected polarizations), is that allows to correct any feature affecting equally to both circularly polarized signals (like atmospheric fluctuations) and does not require precise instrumental calibration (like antenna pattern characterization), only differential aspects between polarizations.

4.1.4.1 *Polarimetric Ratio*

The first approach consists in the analysis of the power returns from reflected signals in both circular polarizations. We define the *polarimetric ratio* as the power coefficient between RHCP and LHCP signals (E_r^{RHCP}/E_r^{LHCP}). In the GPS-SI dataset, this magnitude is obtained from the INT observables, taking the peak power from RHCP waveforms divided by their equivalent in LHCP. For each satellite ground track, a low-pass filtering is applied to the data time-series for removing the residual multipath. Finally, an offset of 6 dB has to be summed due to the additional loss in the RHCP connector mentioned in Chapter 3.

If we assume identical conditions in both front-ends at reception for each polarized signal (i.e. same antenna orientation, whole system's noise figure, gain and length of the cables –electrical distance– in the setup), and the same roughness effect for both circular polarizations when reflecting off the surface, then according to the general expression of a reflected waveform following the KGO approach described in Chapter 2, the polarimetric ratio will be driven by the difference of their respective backscattering coefficients (σ^0), and more concretely, by the contribution of the Fresnel reflection components at each polarization inside the integration over the ocean surface. This effect is portrayed in the panels from Figure 48. On top, the ratio between the Fresnel reflection components ($\Re_{co}/\Re_{cross}$) is shown for different sea water and sea ice conditions along the scenario's visibility range. In addition, the same parameter has been computed for several intermediate values of absolute permittivity (dashed gray lines) in order to illustrate the transition between both stages. On the other hand, the bottom panel displays the polarimetric ratios from KGO simulated waveforms and taking two of the previous examples, modifying the surface state with different roughness values and applying the same geometrical characteristics than the experiment. Notice how, when decreasing roughness, the results tend to the values obtained with the Fresnel components, which is an expected behavior, given that we are approaching to the specular reflection case where the glistening area reduces to a single point over the sea surface. On the other hand, the increase of the roughness parameter provokes a flattening effect over the evolution of the polarimetric ratios along $\sin(\varepsilon)$, as a result of the variation of the incidence angle from the different facets –with different slope– that contribute to the reflected signal over a more spread glistening area.

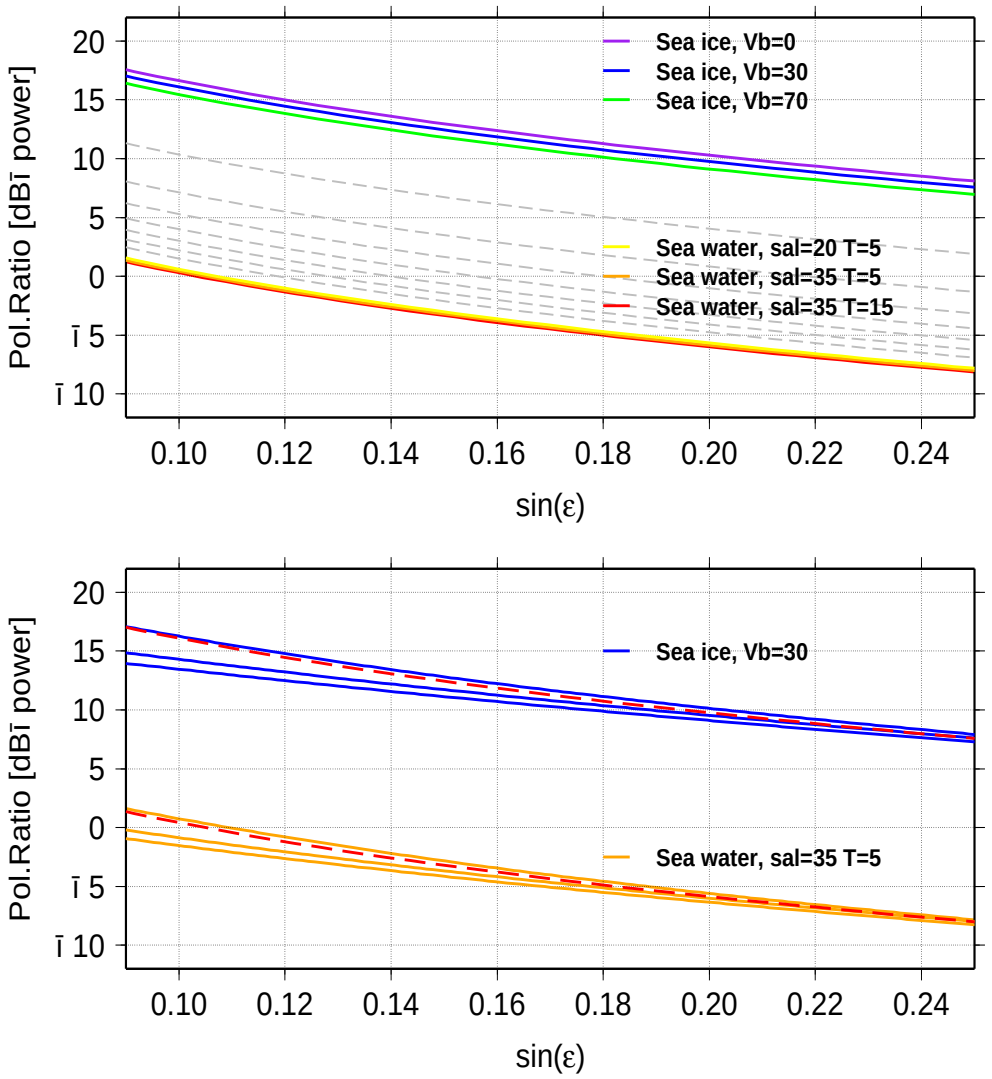

Figure 48.: [Top] Polarimetric Fresnel reflection ratio ($20\log(\Re_{co}/\Re_{cross})$) for different examples of sea water and sea ice from Table 15 (solid lines), and for absolute permittivities going from 10 to 70 F/m in steps of 10 F/m (up to down with dashed lines). [Bottom] Polarimetric ratios from KGO simulated waveforms for one example of sea water –orange– and sea ice –blue– under the geometrical characteristics of the experimental site. Each solid line represents a roughness state: from up to down, *MSS* values of 0.002, 0.014 and 0.026 (in both cases). Dashed red lines mark their equivalent polarimetric Fresnel reflection ratio ($20\log(\Re_{co}/\Re_{cross})$).

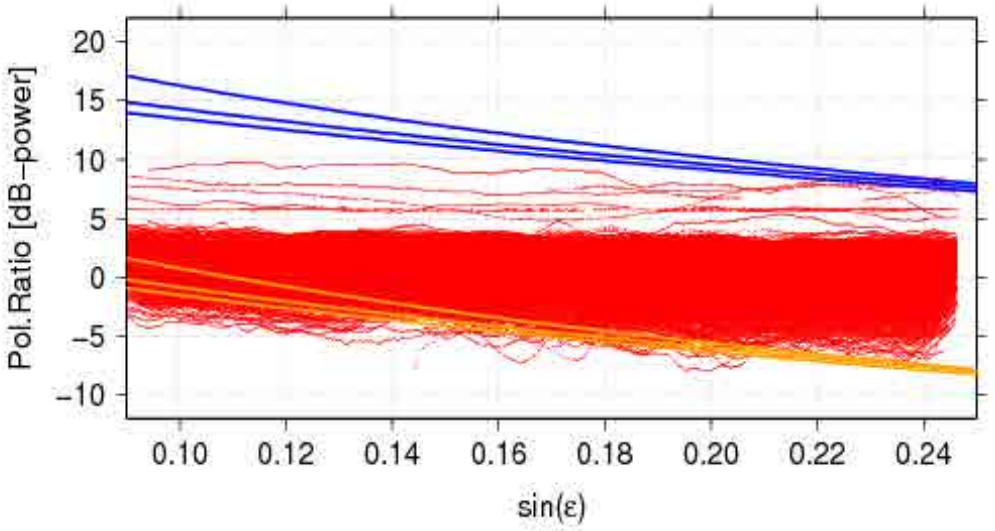

Figure 49.: Evolution of real measurements of polarimetric ratio with respect to $\sin(\varepsilon)$ for the whole campaign's period. Only satellites with trajectories close to the line-of-sight of the Horizon-looking antenna are taken (PRN's 5, 17, 20, 2 and 31). For comparison, the simulations shown in the right panel from Figure 48 are also displayed here.

In spite of the apparently coherent behavior demonstrated by the simulations of the polarimetric ratios, we have seen from Section 4.1.3.1 that our scattering models based on the KGO approximation show inconsistencies for the low elevation range studied here. As it was done in the aforementioned Section, it will be useful to compare the simulations done with real measurements of polarimetric ratios. Figure 49 shows this comparison by taking the examples displayed on the right panel from Figure 48 as a reference models, and the results obtained for several ground tracks visible around the main beam of the Horizon-looking antenna. The most relevant aspect that stands out is the flat shape of the dataset's trend along $\sin(\varepsilon)$. A linear regression reveals a negative slope of $\sim$8.75 dB, significantly smaller –in absolute terms– than the results shown by the simulations, which rang between 40 and 60 dB depending on the roughness parameter. A non-homogeneous distribution and evolution of sea ice over the ground track along the campaign, could explain this behavior. However, this option is discarded by the ancillary measurements described in Appendix D. Therefore, we will consider again a different hypothesis according to what the real measurements apparently show: the evolution of the polarimetric ratio behaves nearly planar for the elevation range considered and its absolute level is mainly driven by the combination of sea water and sea ice over the surface. In addition to the intrinsic limitations of the KGO approach at low elevations, a possible cause of the difference with our modeling might be the fact that we are not taking into account the impact of the refraction of the signal (unlike a ray tracing approach), which distorts the ray path and modifies the angle of incidence around the specular point, specially at such low elevations, provoking then a different power response from the reflective surface.

4.1.4.2 *POlarimetric Phase Interferometry: POPI*

The second approach towards reflectivity retrieval over sea ice is based on the analysis of the phase information from reflected signals in both circular polarizations. We define the POlarimetric Phase Interferometry (POPI) as the phase difference between RHCP and LHCP signals. This concept was first described and further analyzed in Cardellach et al. (2006), which provides also examples of real data from an aircraft campaign over ocean –sea water– using the GOLD-RTR.

From previous Section 4.1.4.1 we have seen how the degree of right and left decomposition is driven by the Fresnel reflection coefficients, which in turn depend on the electrical properties of the ocean surface and the geometry. While the power ratio between the RHCP and LHCP components strongly depends on the angle of incidence, the phase between the two polarization components sticks to a nearly constant value for all the elevations (variation of 0.0025 degree-phase/degree-elevation). The top panel from Figure 50 provides some examples of this phase difference over the visibility range of Greenland's experimental campaign. Therefore, the particular value of the relative RH-to-LH phase depends on the dielectric characteristics of the ocean surface (salinity and temperature in the sea water case, and brine volume for sea ice), covering a dynamical range of the order of 20° for our Arctic scenario. On the bottom panel, the same magnitude is plotted against the polarimetric ratio for a single elevation value (located in the center of the visibility range) in order to illustrate a first approximation of their cross-correlation when changing the ocean surface –in terms of permittivity– with different sea water and sea ice conditions. Polarimetric ratios computed from intermediate values of absolute permittivity –$|\epsilon_{sw}|$– have been added with vertical lines, given that the phase information cannot be retrieved (real and imaginary parts of ϵ_{sw} are needed). We will assume continuity in the POPI when moving from sea water to sea ice; moreover, given the important role played by the salinity content and its regular decrease in such situation, to assume an uninterrupted increase of the POPI seems also realistic. Under such conditions, both polarimetric measurements (phase- and power-based) have a positive trend when the sea water evolves towards sea ice.

The approach followed in Cardellach et al. (2006) is also based on the KGO approximation. Therefore, it assumes that the electromagnetic field received at a certain point above the surface is the sum of several field contributions, each of them coming from a specular reflection on a smooth and well oriented faced (mirror-like patch) of the surface. This total received field at pq polarization state can be expressed as (Equation 1.3 in Cardellach et al. (2006)):

$$E_r^{pq} = |E_{inc}| \sum_{k}^{N-facets} |\Re_{pq,k}| e^{i\Delta\phi_{geo,k}} e^{i\phi_{pq,k}} \tag{60}$$

where E_{inc} stands for the incident field; $\Re_{pq} = \left|\Re_{pq}\right| e^{i\phi_{pq}}$ is the Fresnel reflection coefficient at pq polarization state; k accounts for the facet's index; $N - facets$ is the total amount of facets; and $\Delta\phi_{geo,k}$ represents the phase increment due to the delay path travelled by the k-reflected signal. However, the interesting product in this study is the RHCP-to-LHCP phase difference, or POPI ($\phi_{POPI} \approx \phi_{co} - \phi_{cross}$), and in order to retrieve

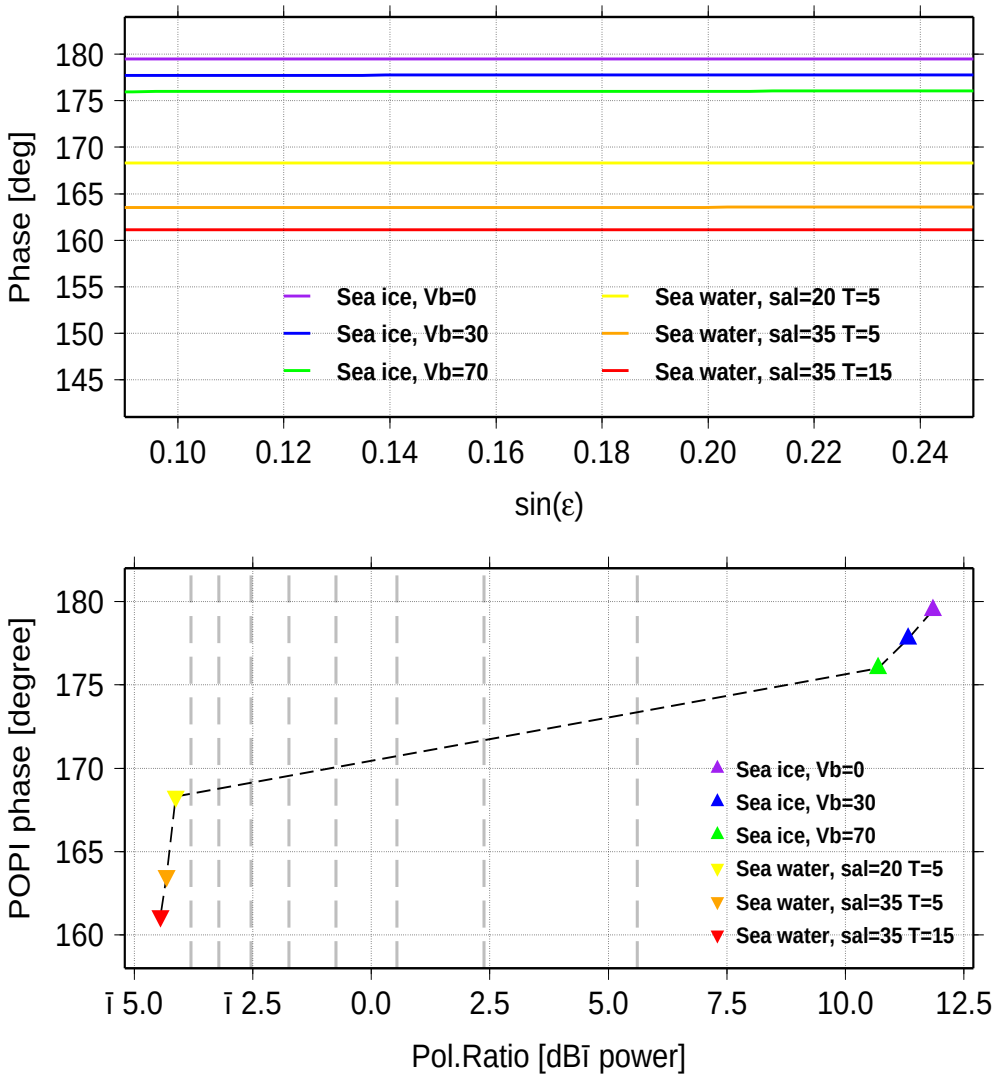

Figure 50.: [Top] Phase difference between co-polar and cross-polar Fresnel reflection components (circular polarization) for different examples of sea water and sea ice from Table 15. [Bottom] The same magnitude as a function of polarimetric ratio for $\sin(\varepsilon) = 0.17$ using the same examples of sea water and sea ice. Vertical gray dashed lines mark the polarimetric ratio for absolute permittivities going from 10 to 70 –left to right– in steps of 10 units (the phase cannot be determined).

it, a combination of electromagnetic fields in both polarizations is required, such as (from Equations 1.4 to 1.7 in Cardellach et al. (2006)):

$$\begin{aligned} E_r^{RHCP} E_r^{LHCP\,*} &= E_r^{co} E_r^{cross\,*} \\ &= \left[|E_{inc}| \sum_{k}^{N-facets} |\Re_{co,k}| e^{i\Delta\phi_{geo,k}} e^{i\phi_{co,k}} \right] \cdot \\ &\quad \cdot \left[|E_{inc}| \sum_{j}^{N-facets} |\Re_{cross,j}| e^{-i\Delta\phi_{geo,j}} e^{-i\phi_{cross,j}} \right] \\ &\approx \Gamma e^{i\phi_{POPI}} \end{aligned} \tag{61}$$

with Γ a real term. Hence, the conjugate product between RHCP and LHCP reflected fields becomes a phasor the phase of which is mostly driven by ϕ_{POPI}.

During the GPS-SI campaign, reflected signals in both polarizations were gathered for up to three different satellites simultaneously at a millisecond rate when RAW acquisition was enabled. Similarly to the process described in Section 4.1.2.1 for phase altimetry, the peak amplitudes and phases of the waveforms from Link-2 (E_r^{LHCP}) and Link-3 (E_r^{RHCP}) are taken to construct what we define as polarimetric field C_{pol}:

$$\begin{aligned} C_{pol}(t, sat) &= E_r^{RHCP}(t, sat) \cdot E_r^{LHCP}(t, sat)^* \\ &= |E_r^{co}(t, sat)||E_r^{cross}(t, sat)| e^{i\phi_{pol}(t, sat)} \end{aligned} \tag{62}$$

with

$$\phi_{pol}(t, sat) = \phi_{POPI}(t, sat) + \phi_0(sat) + \xi_\phi(t, sat) \tag{63}$$

In Equation (63), ρ_{POPI} is the phase product from Equation (61) that we want to retrieve. The term ϕ_0 is an undetermined and constant phase offset driven by the phase-model used in the GOLD-RTR open-look, which is arbitrary for every change of correlator. This has a relevant implication in the analysis of the results, since it hinders the possibility of retrieving the absolute value of ϕ_{POPI} from ϕ_{pol}. In spite of this drawback, the variations of ϕ_{pol} along each satellite's ground track will still be driven by ϕ_{POPI}, and therefore, will be related to changes in the dielectric properties of the ocean surface. Any phase jump provoked by a change of correlators during the acquisition of these data tracks (a known and controlled effect that barely happens during a single satellite's track) can be easily corrected. Finally, the term ξ_ϕ from Equation (63) accounts for phase errors and unmodelled effects, which can be split into several contributions, as defined in Equation (42). In this case, we will assume that the impact of fading or coherence loss is negligible due to the long stability of ϕ_{POPI} (Cardellach et al., 2006). To reduce the effects of instrumental noise and multipath, the approach followed is similar to the one described in Section 4.1.2.3 for phase altimetry: 1 second of coherent integration and low pass filtering with T_M period over each data time series of the complex phasor $C_{pol}(t, sat)$.

4.2 EXPERIMENTAL RESULTS

4.2.1 ALTIMETRIC RESULTS USING CODE- AND PHASE-DELAY

The desired goal would be to link altimetric results with formation, evolution and melting of sea ice. Two different approaches were tested to retrieve a height estimation of the sea surface level. Code altimetry has been computed from the estimated position of the specular point in the shape of the reflected waveforms, analyzing its evolution through whole INT data tracks; whereas phase altimetry is estimated from the phase variation between direct and reflected signals, taken along different continuous intervals in the RAW data tracks. Given the differences in the availability of the type of data required for each case, the amount of observables used in both approaches is not therefore the same.

For code altimetry, two parallel analysis have been presented in Section 4.1.1, depending on the secondary observable used for estimating the position of the specular point: maximum of the waveform and maximum of the waveform's first derivative. For a better comparison with the altimetric results obtained with the phase-based approach (that will be later shown), the receiver-to-surface height retrievals have been also converted to surface ellipsoidal heights referred to WGS84 using Equations (51) and (52), with $\widehat{H_S^R} = 668$ meters (650 m of the cliff plus 18 m of the tower) and $\widehat{H_{ellip}^S} = 23$ meters. The top panel in Figure 51 shows the code altimetric results obtained during the campaign, averaging the individual estimations from the different satellite tracks for each day and using weights based on the error computations from the linear fits applied. Two dashed lines have been added to mark the levels (22 and 23.5 m) where most of the GLAS' –laser altimeter– measurements lie (Figure 125 from Appendix D.5), to have an idea of the range of expected ellipsoidal heights in the experimental site. The bottom panel shows the same results, but applying the more realistic model of ρ_{geo} described in Section 4.1.2.2, which includes tropospheric delay adjustments, and adding tidal corrections from AOTIM-5. All the individual results were obtained from LHCP reflections, since no RHCP tracks passed the quality controls described in Section 4.1.1.1.

Table 16 provides mean and median values and their associated standard deviations of the whole campaign for each approach displayed in Figure 51. The altimetric results show high dispersion (σ_H around 8 m) in all the cases. To use a more realistic model of ρ_{geo}, apparently only adds an offset to the solution, mostly given by the tropospheric adjustments. On the other hand, tidal corrections (with $\sim$2 m peak to peak and zero-mean) do not have a significant impact on the height's dispersion (only cm-level variations). When comparing the results obtained with the two different secondary observables, it can be seen that there is a bias of $\sim$5 m between them. The reason of this effect can be explained by the theoretical evolution of ρ_{MAX} with respect to ρ_{DER} along the elevation angle. From Chapter 2, we know that slant reflections are nearly specular (mirror-like reflections). Therefore, the minimum distance between ρ_{MAX} and ρ_{DER} will occur at the limit of $\sin(\varepsilon) = 0$ (direct signal) and it will increase with the elevation until a constant value (related to the surface conditions and further analyzed in Section 4.2.2). This effect will provoke a positive increment in the slope of $\rho_{MAX}(\sin(\varepsilon))$ compared with $\rho_{DER}(\sin(\varepsilon))$ (something that can be seen in the example in Figure 36), that will be translated into a negative offset in the ellipsoidal height retrieved (since it goes in the opposite direction than H_S^R), as it is reflected on the results obtained. Finally, we could consider

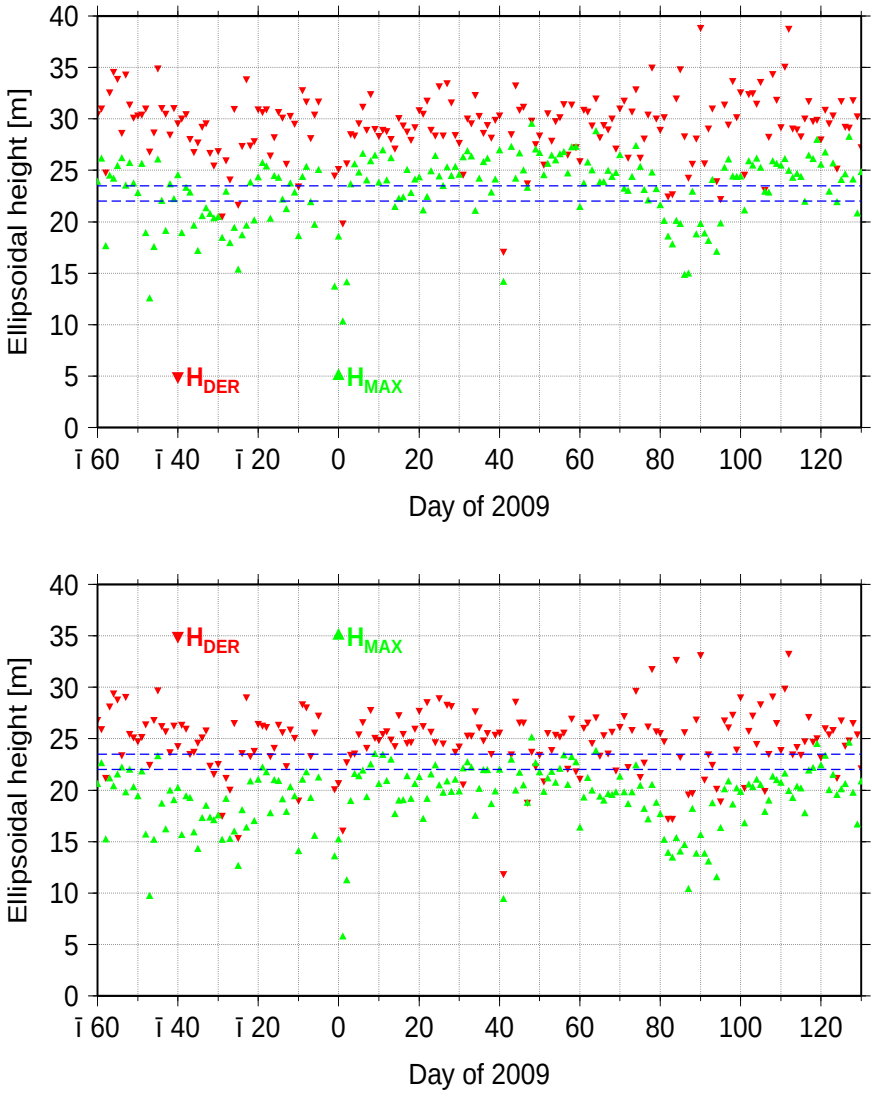

Figure 51.: Time-series of daily averaged ellipsoidal heights retrieved using code-delay from two different secondary observables: maximum of the waveform (H_{MAX} in green) and maximum on its first derivative (H_{DER} in red). All the results come from LHCP reflections. The blue dashed lines mark the sea surface levels measured by GLAS laser altimeter (from Figure 125) during different dates (only one coincident track was available). Each panel shows the results obtained depending on the model of ρ_{geo} employed: [Top] basic approach using $2\widehat{H_S^R}\sin(\varepsilon)$ with $\widehat{H_S^R} = 668$ meters; [Bottom] more realistic model described in Section 4.1.2.2, which includes tropospheric delay adjustments, and adding tidal corrections from AOTIM-5.

Secondary Observable	Corrections	MEAN		MEDIAN	
		H	σ_H	H	σ_H
DER	None	29.40 m	8.01 m	30.10 m	8.04 m
	Troposphere and tide	24.90 m	7.88 m	25.76 m	7.93 m
MAX	None	23.41 m	8.15 m	24.67 m	8.25 m
	Troposphere and tide	19.51 m	8.17 m	21.07 m	8.32 m

Table 16.: Campaign mean and median values, with their associated standard deviations, of single-track ellipsoidal heights (referred to WGS84) retrieved with Code delay. Two secondary observables were under test: position of maximum of the waveform (MAX) and maximum of its first derivative (DER).

H_{DER}, with tropospheric and tide corrections, the formal solution provided by code altimetry. Its mean and median values lie a few meters above the range of estimations obtained with GLAS laser altimeter. Since the error-propagation from delay to height is rather high at low elevations ($\propto 1/\sin(\varepsilon)$), any elevation-dependent unmodeled effect, such as the contribution of the direct signal, might have an important impact on the altimetric estimation. However, the high dispersion of the solution do not justify to dedicate more efforts to remove residual biases.

The poor results obtained with code altimetry in this campaign cannot be employed for sea ice remote sensing purposes. The standard deviation of the ellipsoidal heights retrieved (~ 8 m) is even larger than the tidal signature (~ 2 m), so they cannot be used for detecting variations at cm-level. Note that $\sigma_H = 8$ m corresponds to $\sigma_\rho \simeq 2-4$ m, in our range of elevations. If the observations were conducted at nadir elevations, σ_H would have been reduced to $\sim 1-2$ m for the same σ_ρ. Therefore, in our slant experiment, the task of linking altimetric results with formation, evolution and melting of sea ice will entirely rely on phase altimetry. The next subsections illustrate the efforts made using the phase-delay approach described in Section 4.1.2 towards this purpose.

4.2.1.1 *Phase-altimetry results obtained and comparison with ancillary data*

Following the methodology explained in Section 4.1.2, ellipsoidal height estimations from valid data intervals are obtained. However, in order to extract information about the long-term time evolution of the sea ice surface level, corrections due to the ocean tide have to be included. Figure 52 shows an example of the good agreement between the height measurements and the tide model described in Appendix D.6, AOTIM-5 (Padman and Erofeeva, 2004). In addition, it stands out the consistency between the results obtained from reflections with different polarizations. Notice that the tide model, which has semi-diurnal period, has been evaluated at the time-stamps of the GNSS-R observables, so an aliased signal is thus sampled. AOTIM-5 has a precision around 9.7 cm at the location of the experiment (Padman and Erofeeva, 2004). The average formal precision of the individual height estimates is 2.9 cm for LHCP and 3.2 cm for RHCP. In order to keep low systematic errors, only estimations computed from data intervals longer than 320 1 second-samples have been considered ($>$ 1 km over the ground track). To compare the results between polarizations, 1-day averaged heights have been taken, resulting in a RMS standard deviation of their difference of 8.4 cm.

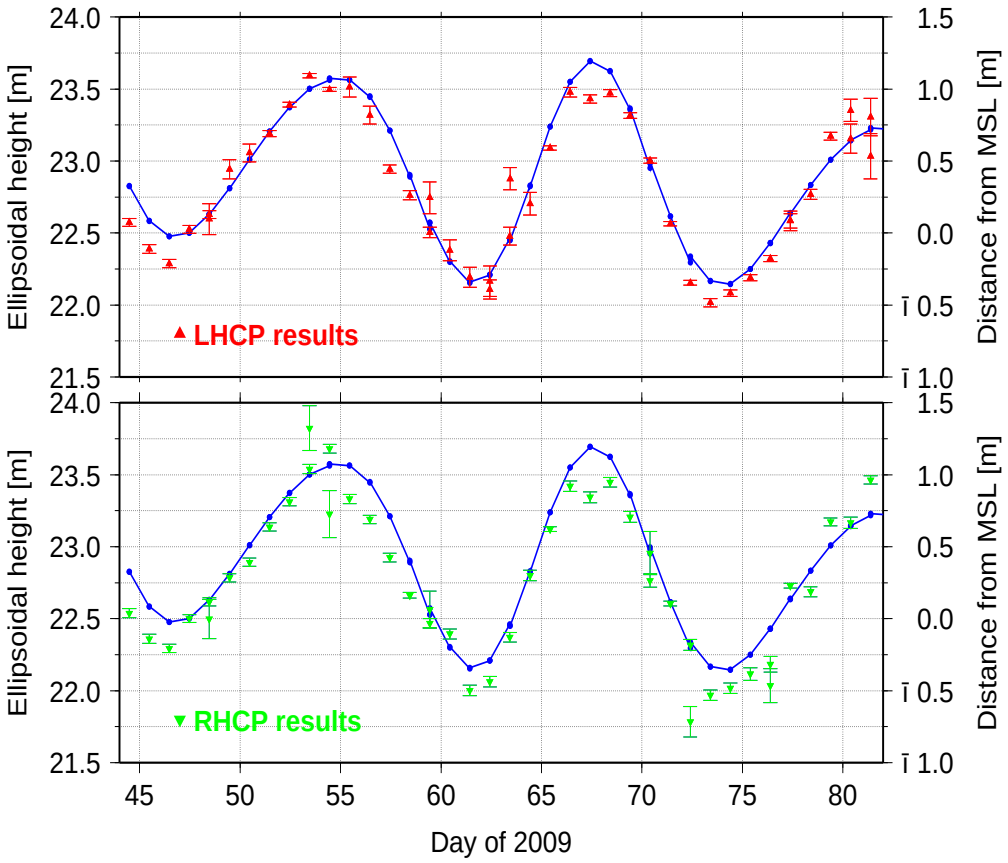

Figure 52.: Ellipsoidal height estimations from reflected GPS signals (PRN 20) at two polarizations compared with AOTIM-5 (blue dots and solid line). The tide model is referred to the mean sea level (MSL, right axis) and its period of oscillations of about 12 days is due to aliasing effect of the one-day sampling rate for GPS measurements (raw acquisition). Figure from Fabra et al. (2011b).

Once corrected with the tide model, the height retrievals are smoothed for a long-term analysis. LHCP and RHCP results are used together after having proved its internal consistency. Their combination seems the better strategy since, despite having less average variance, LHCP estimates need to be complemented with RHCP results to achieve continuity during the whole campaign. Later we will see that RMS_ϕ values from LHCP estimates significantly increase between DoY 85 and 110 (Section 4.2.2.1), coinciding with presence of *fast ice* in the area (Section 4.2.2.3). The bottom panel of Figure 53 shows the smoothed tide-corrected ellipsoidal height estimation using 1 and 10 days of filter's width. For comparison, the top panel shows the ice surface temperature product from MODIS, with an accuracy of 3.0 K. They have been taken by computing the average value from the pixel samples shown in Figure 124 from Appendix D.4. The ice surface temperature controls the rate of sea ice growth by means of the heat transfer at the ice-water interface. This relation is reflected in the results obtained, where the slow variation of the height estimations is in good agreement with the ice temperature evolution. Notice that the temperature's axis in the top panel of Figure 53 is inverted for a better appreciation of this effect. The RMS standard deviation of the 1-day averaged results is 15.4 cm. It is important to consider that the averaged results include all the satellite tracks across an observation area of $\sim$5x5 km^2 of extension. Images from PALSAR available in Appendix D.8 show inhomogeneities within this area that might be related to different ice/water conditions.

Independent altimetric measurements are needed for evaluating the results obtained. The available GLAS data tracks in the experimental area during the last 7 years, with only one coincidence in time for the whole campaigns' period (96 as DoY 2009), have been employed to have a better knowledge of the expected ellipsoidal height variations of the sea ice surface at a given instant of time (geographical variation across the observed area). The comparison of these results with the ellipsoidal heights obtained with GPS reflections is shown in the top panel of Figure 54. The bottom panel takes the measurements shown in Figure 125 from Appendix D.5. The range of height estimations obtained with GPS reflections during the campaign (between 21.9 m and 22.9 m for 1 day sampled) is in good agreement with the results given by GLAS (mostly between 22.3 m and 23.1 m), specially taking into account the offset that the snow loading may add to the latter and the penetration of the L-band signal through ice.

As a last comment, the other dedicated GNSS-R receiver (GORS) also got ellipsoidal height estimations using phase information. The processing steps followed, using a *ray tracing* tool, and the altimetric results obtained, concentrated during a short period of time (4 days) and showing good agreement with semi-diurnal tides, were published in Semmling et al. (2011, 2012). However, the difference in time-resolution between Semmling's approach and the approach presented here impairs a proper statistical comparison.

4.2.1.2 *Accuracy budget and relationship with ice thickness*

The **formal precision** of the height estimations ($\sigma_{\Delta H}$) is here derived from the uncertainties of the slopes obtained after applying a least squares linear fitting algorithm to the processed and continuous phase segments (parameter σ_b from *f*itab routine (Press et al., 2007)). That process uses the single 1-sec standard deviation of the samples (computed

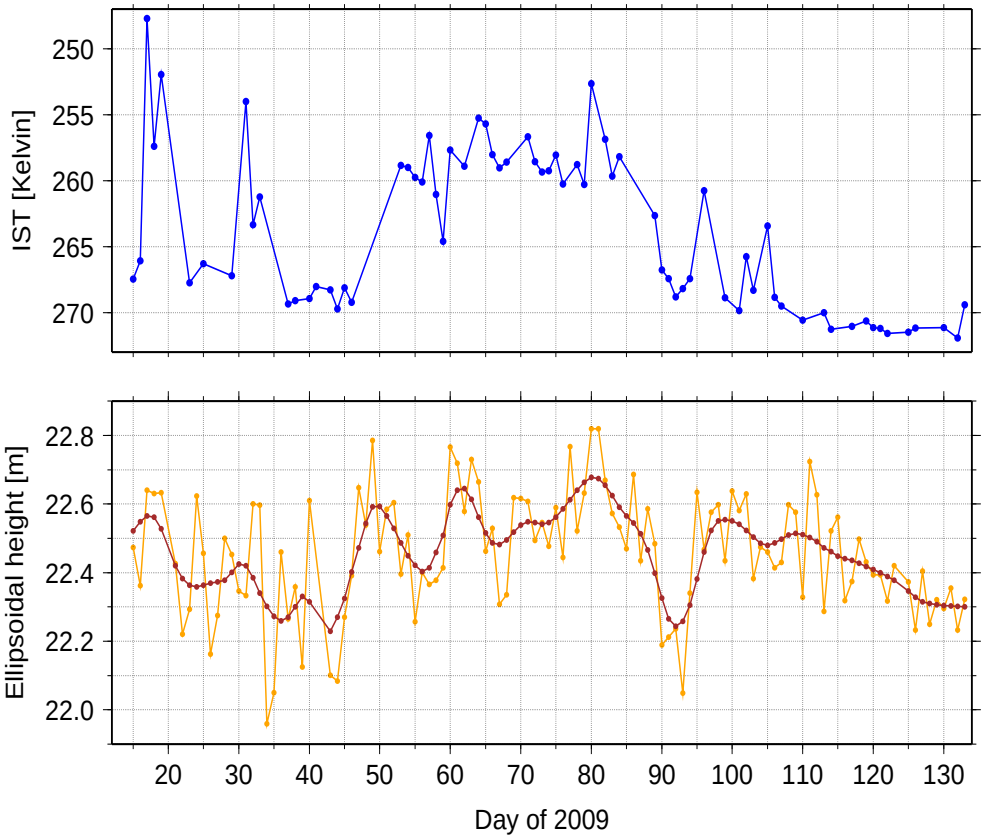

Figure 53.: Time series of ice surface temperature from MODIS (Top) and the result from applying two cosine arch filters to the height estimates from both polarizations (Bottom). The widths of the filters are 1 day (higher variability -orange-) and 10 days (lower variability -brown-). The temperature's axis is inverted for a better comparison. Figure from Fabra et al. (2011b).

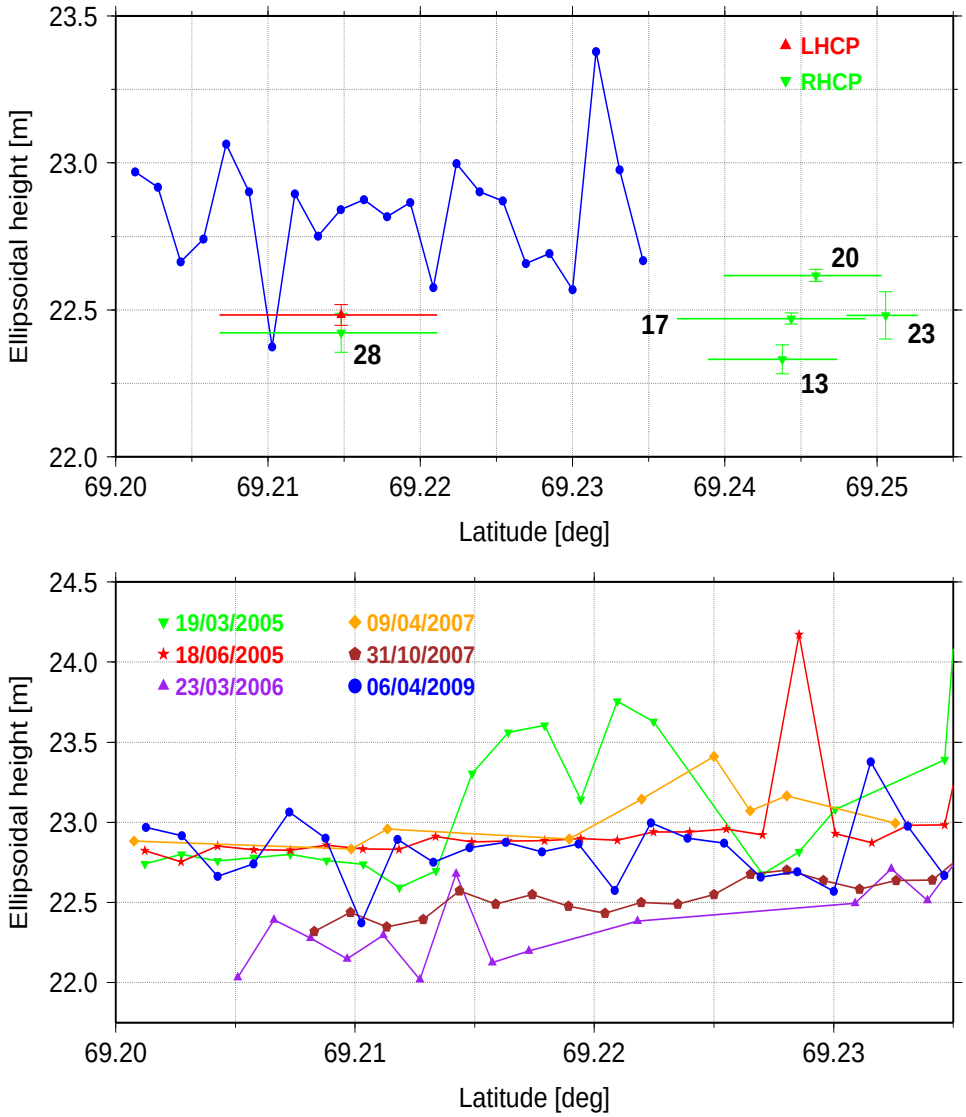

Figure 54.: [Top] Comparison between the altimetric results obtained with GPS reflections (with PRN number) in both polarizations (red and green triangles) and ICESat GLAS (blue circles) during the only day of time coincidence during the campaign (April 6th 2009). In the case of GPS results, the horizontal lines stand for the length of the data interval over the ground track (bottom panel from Figure 24) needed to estimate the ellipsoidal height. [Bottom] Height retrievals from ICESat GLAS at the campaign's location for several days. The reference ellipsoid is WGS84 in all cases. Figure from Fabra et al. (2011b).

Altimetric Errors		Type
GOLD-RTR: **Actual Formal Precision** (given by LSQ fit)	LHCP: 2.9 cm ($\geq$ 320 seconds) RHCP: 3.2 cm ($\geq$ 320 seconds) 15.4 cm (1 day average, tide corrected with AOTIM-5, all polarizations and satellites)	dispersion
GOLD-RTR Robustness: **LHCP vs. RHCP**	8 cm ($\geq$ 320 seconds)	dispersion
Multipath induced error	$<$5 cm ($\geq$ 320 seconds) $<$15 cm ($\geq$ 150 seconds)	bias
Troposphere induced errors	Between 1 and 5 cm (assuming typical TZD errors)	bias

Table 17.: Estimated errors in phase altimetry.

during the coherent integration) to weight them. Basically, $\sigma_{\Delta H}$ contains the information of how good is the matching between the data samples and the straight line fitted to them, which is related to their noise. Table 17 compiles the formal precision of the measurements.

Despite that precision is mainly affected by the thermal noise of the reflected signal, there are other contributors:

- Slow variations in the ice surface and roughness along the averaged track.
- For 1-day averaging, variability given by the fact that individual samples are taken from a large area with different ice conditions.

In addition, there are two main effects that may add a systematic error to the estimation (Section 4.1.2.4):

- **Multipath:** In addition to increase the signal's dispersion, multipath may affect the correct estimation of the slope of the data track, inducing systematic errors up to **5 cm** for phase tracks longer than 320 samples (Figure 40).
- **Troposphere:** The procedure requires TZD measurements. A typical error in the TZD estimates of the order of 0.5 cm would produce systematic errors **between 1 and 5 cm** in altimetry at low elevations.

Regarding **accuracy**, the most limiting factor for its retrieval has been the lack of a proper "ground truth". The altimetric estimate can be defined as a sum of several factors:

$$H_{WGS84} = H_{sea} + \Delta H_{ice} + \Delta H_{tide} \tag{64}$$

Being H_{WGS84} the height between the reference ellipsoid WGS84 and the sea ice surface level, H_{sea} stands for the mean sea level with respect to WGS84, ΔH_{ice} is the increment due to presence of ice and, finally, ΔH_{tide} stands for the variation given by the tide movement. Therefore, the second term is the most relevant for sea ice remote sensing purposes. This term, usually known as sea ice freeboard level, is related to the **thickness** of the ice mass following the Archimedes buoyancy principle.

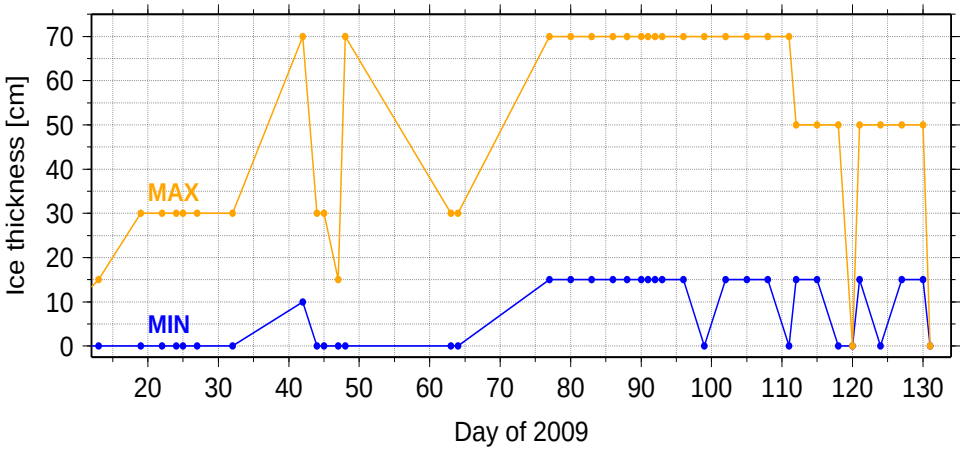

Figure 55.: Daily ranges of ice thickness in the experimental area according to DMI's ice-charts.

During the altimetric process, ΔH_{tide} is corrected using AOTIM-5, an Arctic tide model with data assimilation with **9.7 cm** of error. After that, the remaining altimetric estimates are the sum of the two first terms in Equation 64. A proper "ground truth" is then required for an analysis of the accuracy of these results. The ellipsoidal height product provided by GLAS laser altimeter would be a valid option, but there is only one coincidence during the whole campaign. In order to have a better knowledge of the expected height variations in the area, the time window search of satellite passes was increased until 2005, obtaining then five additional data tracks. The variability of the different single-shot height samples found shows good agreement with the altimetric estimates obtained with GPS reflections (approximately between 22 and 23 meters), specially taking into account the offset that the snow loading may add to the GLAS measurements and penetration of the GPS L-band signal in ice (not determined). The accuracy then, *seems* to be below 1 meter at least (and it simply *seems* because there are no other altimetric or tide gauge measurements to confirm it).

As it has been mentioned before, a desired result would be to relate height estimates with ice thickness records. The ice-charts provided by DMI contain this information (described in Appendix D.3) for different days during the campaign. However, the main concern about this data product is the lack of precision, since they provide up to 3 code-numbers for a given region, where each of them represents a range of valid values of ice thickness. Moreover, in order to have a long term evolution of height estimates, the results from different GPS ground tracks are 1-day averaged, merging sometimes different regions from the ice-charts. As a consequence, the daily records of ice thickness in the experimental area results in a wide range of values, as it can be seen in Figure 55. Notice that the maximum thickness reported in these ice-charts (with the exception of winter ice) is 70 cm (Table 24 from Appendix D.3).

4.2.2 REFLECTIVITY AND ROUGHNESS TOWARDS SEA ICE CLASSIFICATION

The work done in Belmonte et al. (2009) has been already mentioned in Sections 4.1.3 and 4.1.4 as a reference research of GNSS-R over sea ice. After comparison with several remote sensing instruments (a multi-frequency polarimetric scanning radiometer and a lidar profiler plus RADARSAT and MODIS imagery), they concluded that GPS roughness and permittivity –linked to reflectivity– retrievals are helpful in the interpretation of signatures observed by more traditional passive/active microwave sensors. In the present study, different strategies have been tested for the same purpose from Greenland's dataset. Table 18 summarizes the main characteristics of the followed approaches. The results obtained and their comparison with the ancillary data available are described in Sections 4.2.2.1 and 4.2.2.2, depending if they are roughness- or reflectivity-sensitive respectively, and finally, they are jointly employed in order to make a rough estimation of the sea ice state during the whole campaign in Section 4.2.2.3.

4.2.2.1 *Roughness retrieval of the ocean surface*

Two different approaches have been followed to retrieve an estimation of surface roughness. The first one, described in Section 4.1.3.1, exploits how the scattering redistributes the power along the waveform in order to get a secondary observable, called scatterometric delay, from simply two delay positions (peak and maximum of its first derivative), and then to infer from it a measurement of roughness –*MSS*– using an empirically corrected version of a standard KGO-based electromagnetic model. The second method, explained in Section 4.1.3.2, is focused on the variability of the interferometric phase, which contains altimetric information, to perform an estimation of the RMS of the surface height level –RMS_H–, a parameter often employed to characterize surface roughness.

Figure 56 shows the results obtained with both approaches, taking the median value from each daily time-series covering a single ground track. The *MSS* retrievals here displayed (top panel) correspond to PRNs whose ground track is located inside the main

Secondary Observable	**Retrieval**	**Sensitive to**	**Analyzed in Section**	**Data type**	**Polarization**	**Temporal resolution**
Scatterometric delay	*MSS*	Roughness	4.1.3.1	INT	LHCP	1-sec$^{(a)}$
RMS interferometric phase	RMS_H	Roughness	4.1.3.2	RAW	LHCP, RHCP	1-sec$^{(b)}$
Peak power	Polarimetric ratio	Reflectivity	4.1.4.1	INT	LHCP + RHCP	1-sec$^{(a)}$
Phase from peak	POPI	Reflectivity	4.1.4.2	RAW	LHCP + RHCP	1-sec$^{(a)}$

Table 18.: Secondary observables for reflectivity and roughness retrieval of the ice surface (considerations for GPS-SI campaign). $^{(a)}$Due to multipath, the time series of each result have been filtered with a 70-sec (T_M) low pass filter. $^{(b)}$Since the computation of RMS requires a time window, T_M has been chosen.

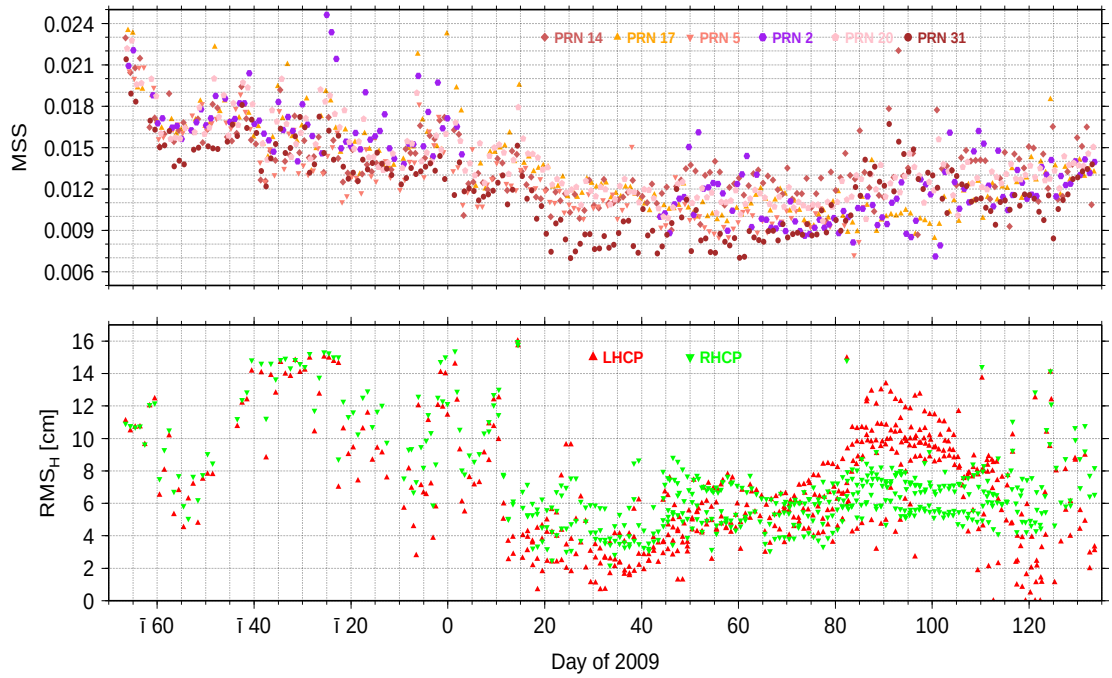

Figure 56.: [Top] Daily single-track median values of MSS for the whole campaign. Only PRNs whose ground track is located inside the main beam of the Horizon-looking antenna with LHCP are considered. [Bottom] The same type of measurement for RMS_H. In this case, all the single-tracks and polarizations are considered (RHCP with red triangles, RHCP with green inverted triangles). Note that the results reach a maximum level between 15 and 16 cm, which corresponds to the mean upper limit shown in the bottom panel from Figure 46.

beam of the Horizon-looking antenna, where a better SNR is obtained. Only LHCP is considered. We can see that there is good agreement in the general pattern followed by different satellites. Small differences can be explained by the fact that, even being close to each other, their respective ground tracks have a different location (and time of observation) and certain degree of variation in the sea surface conditions is expected. On the other hand, given their limited availability (RAW acquisition) and their robustness against thermal noise (due to long coherent integration), all the estimations of RMS_H are plotted (bottom panel), including those obtained from RHCP reflections. At a first glance, we can see that the number of samples is not uniformly distributed along time due to the RAW acquisition strategy. The comparison between different polarizations shows good agreement with the exception of the period comprised between DoY 85 and 110, where the LHCP values rise significantly with respect to those obtained from RHCP samples. The reasons are explained later on.

Common patterns appear during the campaign when comparing both roughness retrievals. High values are measured (a bit scattered for RMS_H) until mid January – DoY 15/20–; from this point on, they keep consistently low values until DoY 85 (with a small step for RMS_H around DoY 45), where they increase again until DoY 110 (in a more moderate manner for RMS_H in RHCP); finally, they show a similar behavior than at the beginning. According to the information provided from the in-situ Arctic weather

station, presence of sea ice was confirmed in the area between DoY 20 and 110 (with some additional sea ice around DoY 125/130). In terms of roughness over the ocean surface, the formation of sea ice –new ice– represents a smoother scenario compared to open waters and other stages of development; therefore, its time evolution (from new to young ice) will provoke an increase of roughness. Both conditions are consistent with the results obtained. Further analysis about the estimation of sea ice state using these roughness retrievals will be given in Section 4.2.2.3.

Regarding the range of values achieved with the different estimates, Figure 57 shows their histograms when considering only the period with confirmed presence of sea ice (DoY 20-110). The MSS values show a nearly Gaussian distribution with $\mu \sim 0.011$ and $\sigma \sim 0.003$, which has a general good agreement with the estimations made in Belmonte et al. (2009) for early stages of sea ice (MSS from 0.004 to 0.014). On the other hand, the retrieved RMS_H displays a more asymmetric shape that could be increased by the elevation-dependent limit derived from RMS_ϕ and previously illustrated in Figure 46. In addition, when comparing polarizations, the LHCP case shows a higher dynamic range ($\sigma \sim 5$ cm) than the RHCP case ($\sigma \sim 3$ cm). Such differences were not expected in the theoretical analysis given in Section 4.1.3.2, where it was assumed that, after processing and for a given elevation, the variation of RMS_ϕ^2 was directly proportional to RMS_H^2, which, in principle, should not be polarization-dependent. Therefore, a contribution from other term in Equation (58) provokes an overestimation of RMS_H from one polarization with respect to the other. By checking this expression, the best candidate responsible for such behavior is RMS_N. This term is inversely proportional to the SNR –in amplitude dimensions– achieved after the long coherent integration applied to the counter-rotated interferometric phasor C_I. We assumed that this process would rise enough the SNR to make RMS_N not relevant. However, the results obtained indicate that this parameter has still a residual impact on RMS_ϕ that affects the proper retrieval of RMS_H. Comparing the RMS_H histograms with the temporal evolution of their median values shown in the bottom panel from Figure 56, we can see how the mismatched spread of the results' distributions from opposite polarizations is produced by a different rate of variation with sea ice evolution. We have seen from Section 4.1.4.1 how changes in permittivity vary the reflected signal's power and therefore, they would also affect RMS_N. Our new hypothesis will be that, even thought RMS_ϕ is mostly driven by RMS_H, offset differences between opposite polarizations on the retrieval of this last term might be produced by RMS_N, which in a long term analysis of RMS_H would manifest a differential rate variation. A cross-comparison with other polarimetric retrievals that might help to understand this effect will be given in Section 4.2.2.3.

The roughness of the ocean surface in absence of sea ice –open waters– is mainly driven by the wind speed. Chapter 2 mentioned several research studies on the applicability of GNSS-R for the retrieval of this magnitude, including some of them comparing experimental measurements of MSS with wind speed and showing good agreement with the relationship predicted by Elfouhaily's model (Elfouhaily et al., 1997). In the GPS-SI campaign, real measurements of wind speed and direction were provided by QuikSCAT (only available over open waters). However, a land mask that enters 50 km into the sea has to be applied, disallowing the acquisition of these retrievals at the experiment's location (up to $\sim$5 km from the coast) as illustrated in Figure 58. In spite of that, wind measurements collected from a geographical window of Long $\in$ {52°W,56°W} and

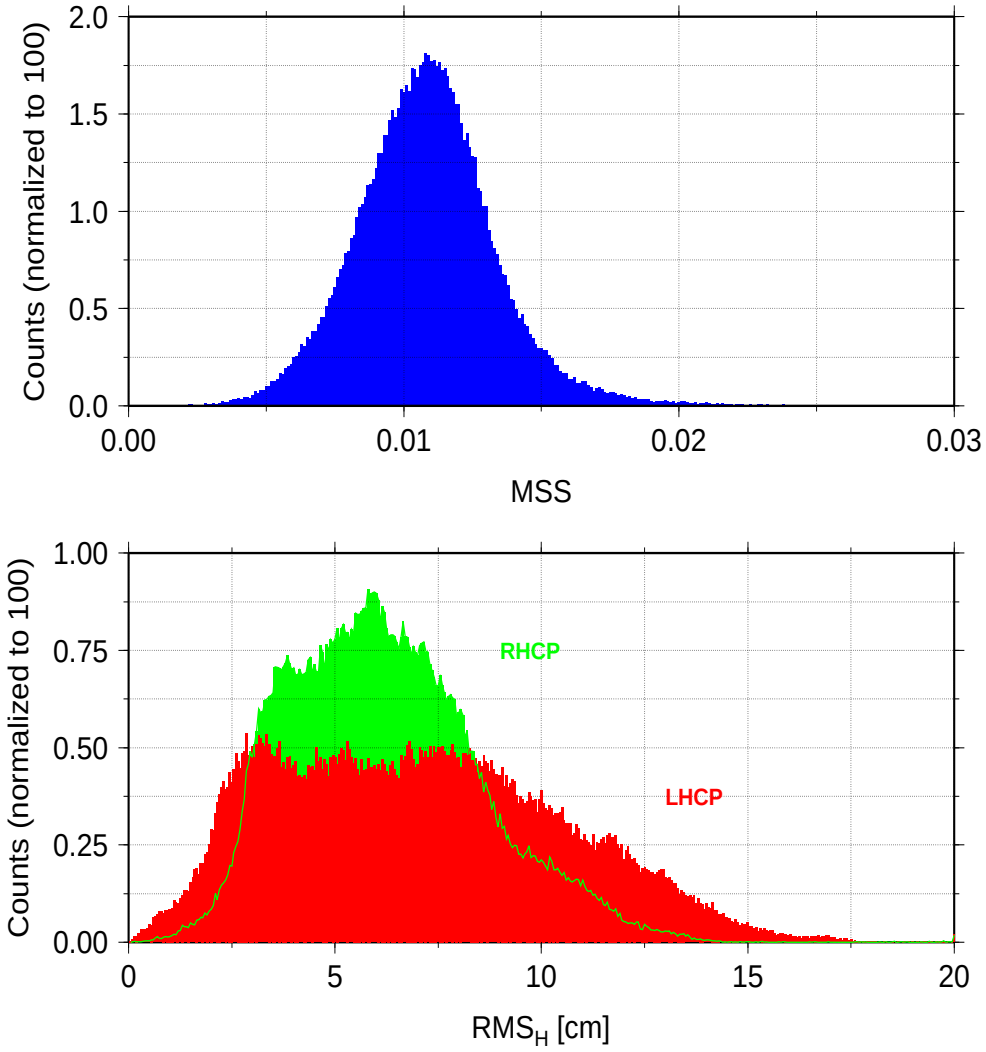

Figure 57.: [Top] Histogram of MSS measured when presence of sea ice was confirmed in the area (DoY 20-110). Only PRNs whose ground track is located inside the main beam of the Horizon-looking antenna with LHCP are considered. [Bottom] The same type of measurement for RMS_H. In this case, all the single-tracks and polarizations are considered (RHCP in red, RHCP in green).

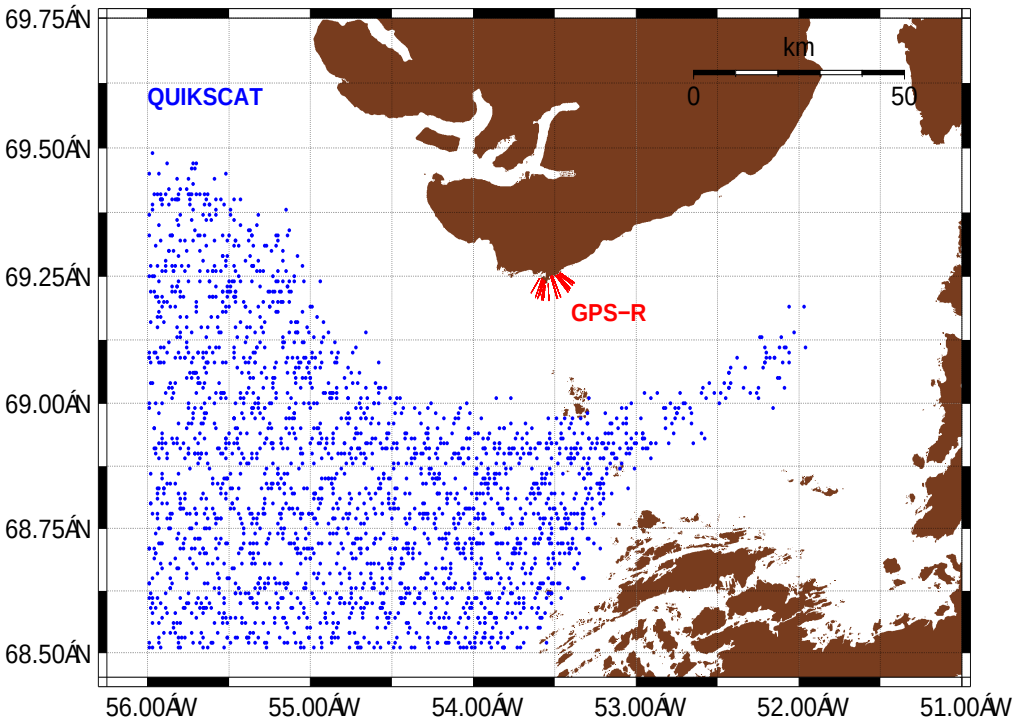

Figure 58.: Position of QuikSCAT measurements compared with GPS-R ground tracks at Disko Bay. In the case of the latest, the location of high cliffs and mountains at North/North-West might offer some protection near the coast against strong winds coming from these directions.

Lat $\in$ {68.5°N,69.5°N} have been considered in order to have an approximation of how this magnitude evolved during the first months of the campaign. Figure 59 shows the comparison between our ice-free sea surface roughness retrievals (MSS and RMS_H) and these wind speed measurements (displayed on the top three panels respectively). The bottom panel illustrates the slow evolution of each magnitude, after applying a box filter of 2 days to the time series made up from the upper panels. By checking this last representation, we can see how the pattern followed by the roughness retrievals show common variations, or in other words, they have similar positions of peaks (e.g. DoY -62, -41, -24, -17, -1, 10 and 14) and valleys (e.g. DoY -56, -38, -28, -20, -4, 4 and 12). Regarding the level achieved for the RMS_H retrievals compared to MSS (not only their variations), it seems that they have a positive offset from DoY -45. If we take a look to the individual measurements (second panel up to down), we can observe that this effect specially affects to PRNs whose ground track is located far from the line-of-sight of the Horizon-looking antenna (PRN 31 would be on the limit of the main beam), then having a lower gain and SNR. Under such situations, a residual noise factor could overestimate RMS_H in both polarizations. Notice that this would be consistent with our previous hypothesis about the residual impact of RMS_N.

By comparing the roughness retrievals with wind speed measurements in the bottom panel from Figure 59, we can see that in spite of the general good agreement shown

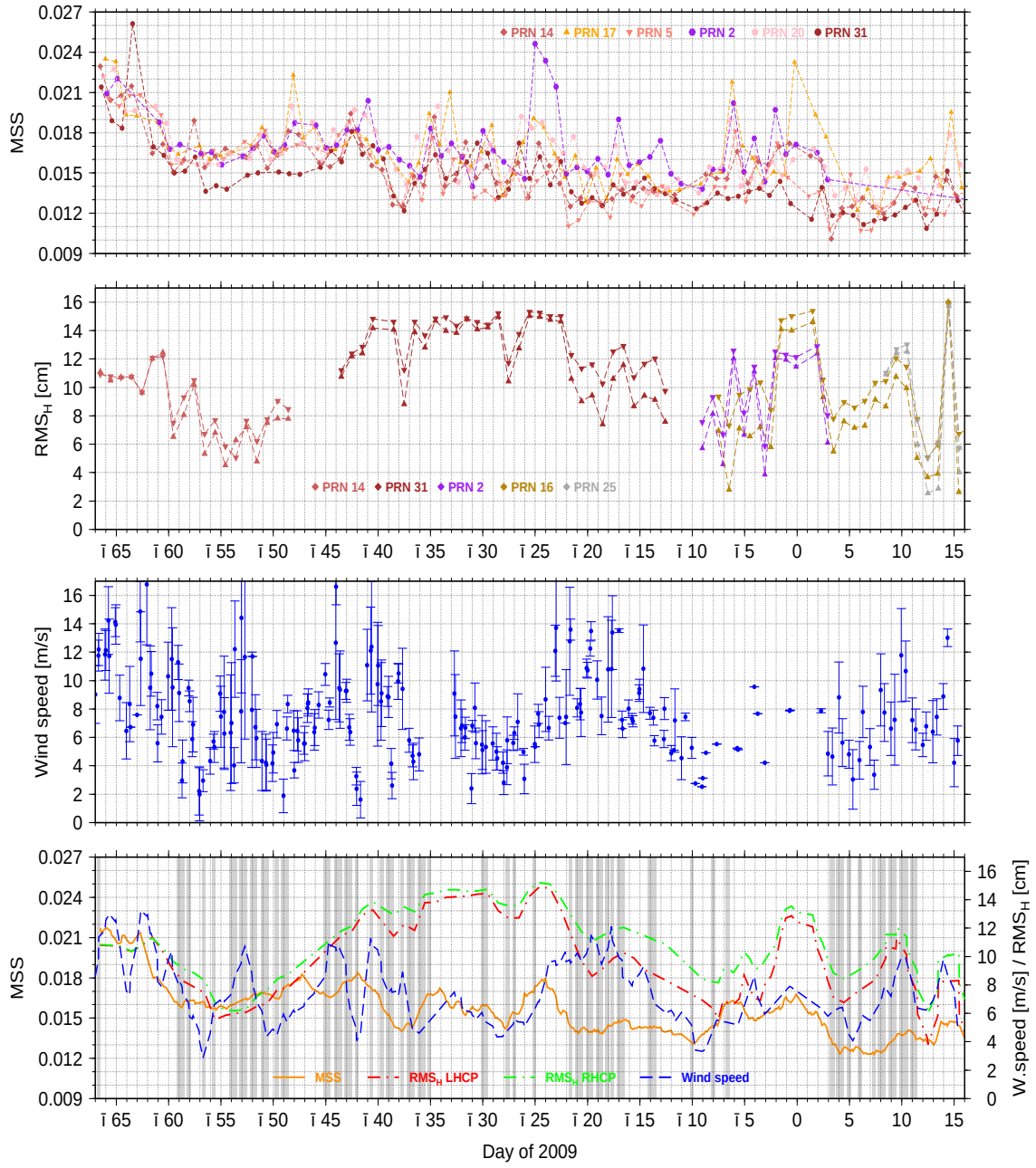

Figure 59.: Evolution of different magnitudes with respect to day of year 2009 (negative values for 2008). From up to bottom: [First] Daily single-track median values of MSS. [Second] The same type of measurement for RMS_H. Different symbol stand for different polarization (LHCP-triangle, RHCP-inverted triangle). Note that the results reach a maximum level between 15 and 16 cm, which corresponds to the mean upper limit shown in the bottom panel from Figure 46. [Third] QuikSCAT wind speed retrievals from a geographical window of Long. $\in \{52°\text{W},56°\text{W}\}$ and Lat. $\in \{68.5°\text{N},69.5°\text{N}\}$. If several samples were available at the same time, only the mean value is plotted and an error bar marks their standard deviation (the single measurements were displayed in Figure 127). [Fourth] Slow evolution of the magnitudes plotted in the three upper panels, after applying a box filter of 2 days. A gray background marks the time periods where the wind direction (provided also by QuikSCAT and displayed in Figure 127) has azimuth$\in \{-60°,15°\}$ (i.e. winds coming from North/North-West) and therefore, the impact of high winds may be lower in the GPS retrievals (locations shown in Figure 58).

during some time periods, there are high winds apparently not sensed by the roughness estimates (e.g. DoY -53, -44 and from -22 until -17). A possible explanation for this behavior can be found in the wind direction provided also by QuikSCAT. On the aforementioned panel, gray background areas mark the time periods where this magnitude has azimuth$\in \{-60^{\circ},15^{\circ}\}$ (i.e. winds coming from North/North-West). Note that the inconsistencies found between GPS and QuikSCAT measurements coincide with this background. On the map displayed in Figure 58 we can observe that Disko island is right on the North from the GPS reflections. The presence of high cliffs (like the receiver's location) and mountains at these positions will offer some protection near the coast against strong winds coming from these directions, which will be better sensed at more distant locations (like those from QuikSCAT).

4.2.2.2 *Results obtained with Reflectivity-sensitive observables*

Similarly to the previous case, two methodologies have been tested to obtain reflectivity estimations linked to the dielectric properties of the ocean surface. Both of them exploit the use of combining RHCP and LHCP reflected signals. While the first approach, described in Section 4.1.4.1, consists on measuring the polarimetric ratio of the peak power waveforms with opposed polarizations, the second gets their phase difference (POPI), as explained in Section 4.1.4.2. These two parameters might determine the presence and evolution of sea ice by means of the Fresnel reflection components.

Figure 60 displays the evolution of polarimetric ratio compared with sea ice concentration as obtained from visual inspection from the Arctic weather station. Different angles of elevation and only PRNs whose ground track was placed close to the weather station are considered. We can see how the polarimetric ratio clearly raises when there is presence of sea ice. In addition, there is consistency between the results obtained from different satellites, and in particular, their combined evolution at the central location of the experimental site (line of sight of the Horizon looking antenna and mid-elevation) shows good agreement with changes in sea ice percentage. This is due to the fact that, for relatively thin ice (during formation and melting of sea ice), the reflectivity properties of the ocean surface respond to a combination of sea water and sea ice, in particular to the resultant salinity content driven by the relative amount of the last element, and this relationship is reflected on the results obtained.

With the purpose of better illustrating their spatial variability, Figure 61 shows the polarimetric ratio measurements plotted over maps (ground track representation) for a given time period. In particular, the selected time window goes from DoY 44 until 51, when a drop in sea ice concentration has a different impact over these measurements in previous Figure 60, depending on the elevation angle. We can clearly distinguish common patterns over the ocean surface which potentially indicate ice-water (or different ice concentration levels) transitions, and how they evolve as time goes by.

In order to check the impact of the surface state on these retrievals, a cross-comparison with roughness measurements will be given in next Section 4.2.2.3, where a new type of representation will be first introduced to allow a better spatial and temporal analysis.

Regarding POPI, we know from Section 4.1.4.2 that it was not possible to get its absolute value due to limitations in the GOLD-RTR's architecture during the GPS-SIDS campaigns. Therefore, we can only check POPI variations along single data tracks. In order to validate such measurements, the only retrieval related to the dielectric properties of the ocean surface which was available during the experimental campaign with an acceptable spatial resolution (in the order of hundreds of meters) is the polarimetric ratio, whose good agreement with sea ice concentration has been shown in previous Figure 60. In addition, like other phase-based retrievals obtained by means of RAW acquisition, the availability of POPI measurements is not uniformly distributed along the campaign. We focus our analysis around two relevant time periods where there was repeatability in the acquired RAW data tracks in terms of location (i.e. two PRNs with closer ground tracks available): from DoY 17 to 32, when there was consistent formation of sea ice (ice concentration arriving to 50%), and from DoY 60 to 75, when the ice cover achieved certain stability (ice concentration over 90%). The daily comparison of POPI measurements with polarimetric ratio during the first period is shown in Figures 62 and 63, while the

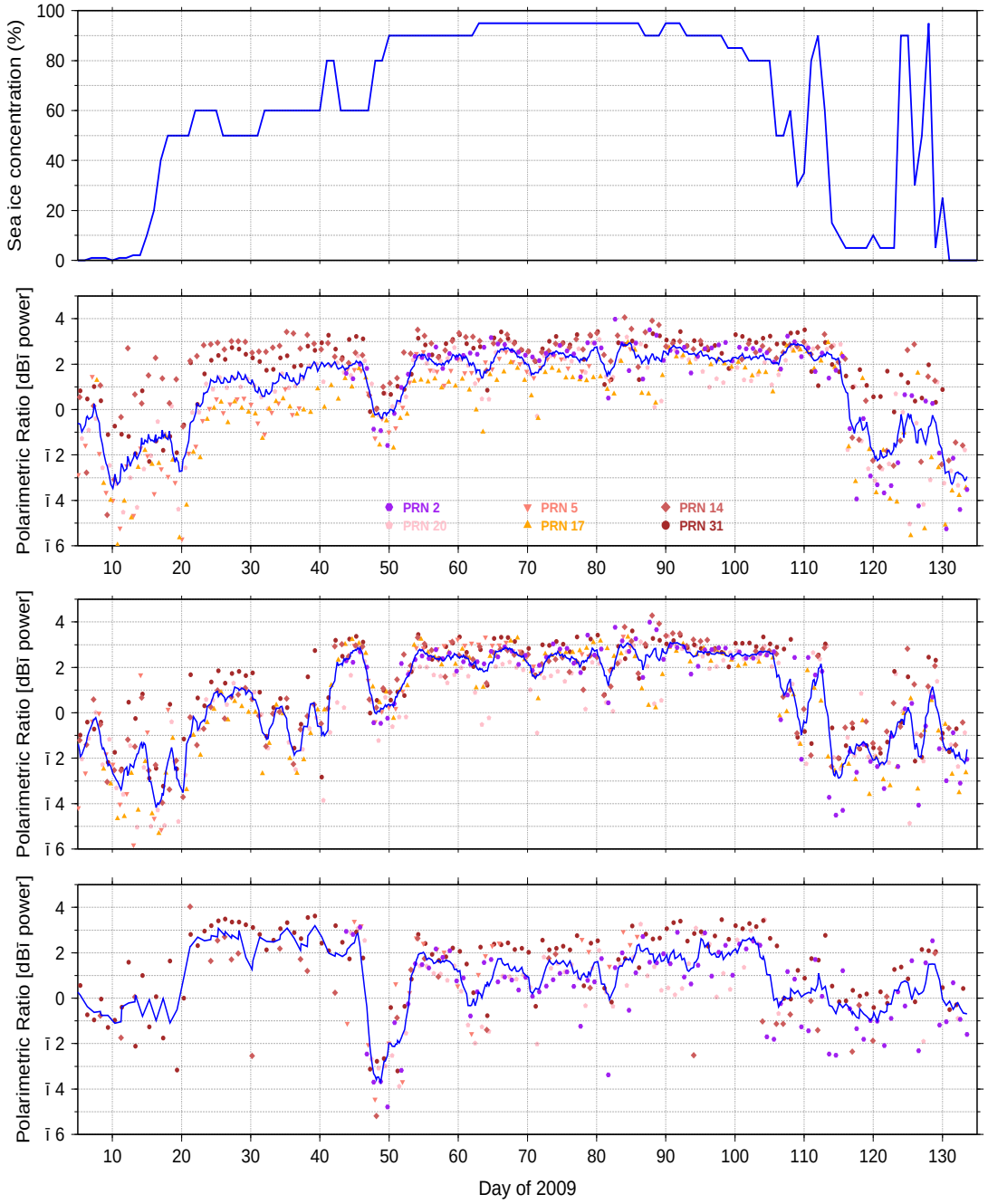

Figure 60.: Evolution of polarimetric ratio measurements compared with sea ice concentration with respect to day of year 2009. From up to bottom: [First] Sea ice concentration obtained by in-situ visual inspection. [Second] Polarimetric ratio at $\sin(\varepsilon) = 0.21$. [Third] Polarimetric ratio at $\sin(\varepsilon) = 0.17$. [Fourth] Polarimetric ratio at $\sin(\varepsilon) = 0.12$. Only PRNs whose ground track is located inside the main beam of the Horizon-looking antenna are considered. A solid blue line has been added to the polarimetric ratio measurements that stands for their joint slow evolution after applying a 2-days box filter.

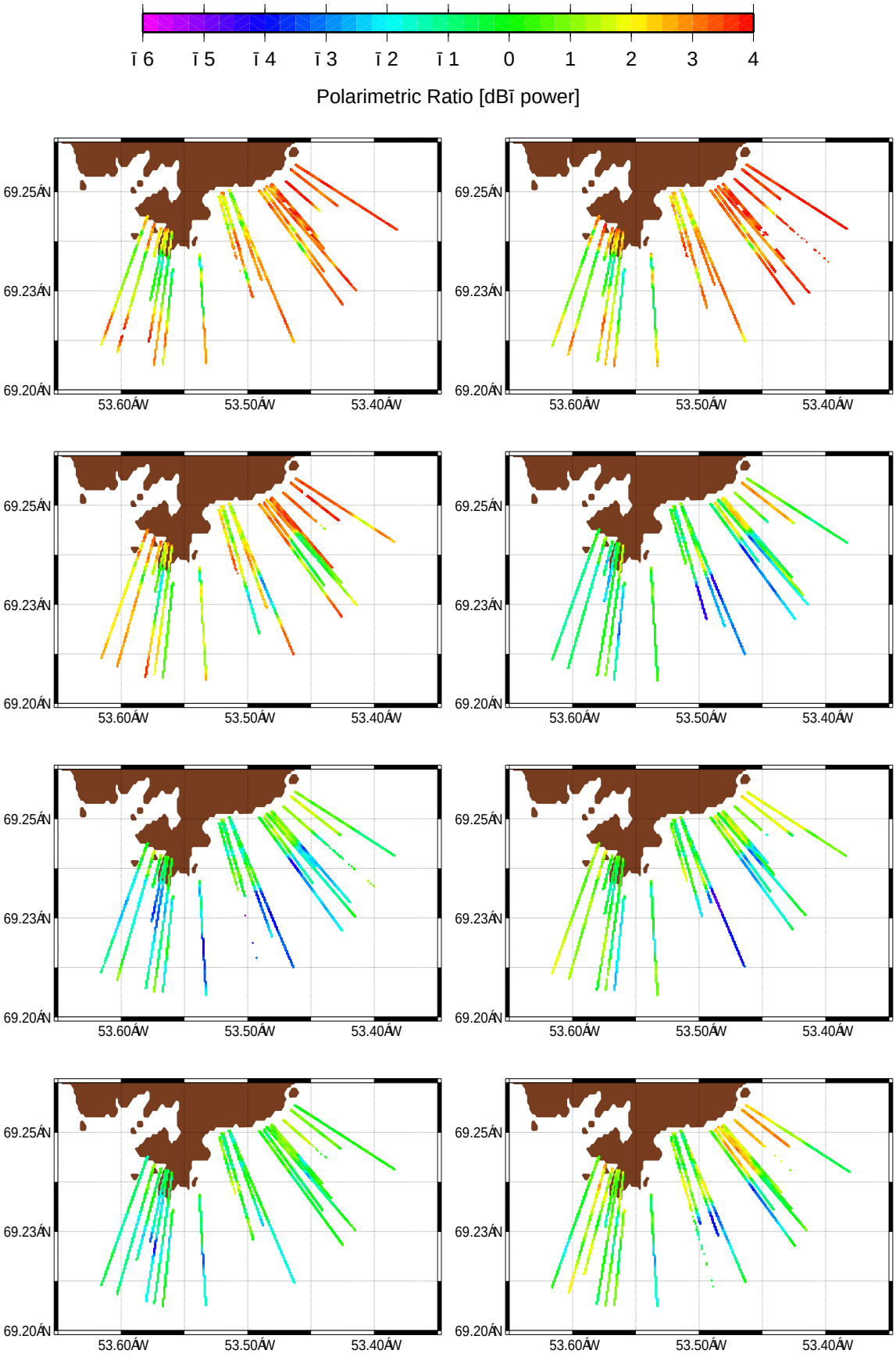

Figure 61.: Maps of polarimetric ratio measurements for 8 consecutive days: from left to right and up to down, DoY 44 until 51.

results from the second period are displayed in Figures 64 and 65. In general, we can see that the most significant variations found in the polarimetric ratio, which indicate changes in the dielectric properties of the surface (e.g. sea water to sea ice transitions or between different sea ice stages), are consistently sensed by POPI as well. This statement specially holds during the first period, while the second period shows more discrepancies. In fact, notice that the best agreement is found for the lowest values of polarimetric ratios ($\sim 0dB$), which means that this happens for open waters and very thin sea ice. On the other hand, for higher values ($\sim 2dB$), both magnitudes are affected by uncorrelated fluctuations. However, a closer inspection of the results reveals a curious behavior: these fluctuations have a similar pattern and period for both cases, but with a different phase offset (they are nearly in counter-phase). Clear examples of this effect that appear on the previous Figures are PRN 25 –first period– for $\sin(\varepsilon) > 0.155$ and PRN 2 –second period– for $\sin(\varepsilon) \in \{0.14, 0.22\}$. Finally, an additional disagreement with our theoretical expectations from Section 4.1.4.2 relies on the range of variation of the POPI measurements. While less than 20° were expected in a sea water to sea ice scenario (Figure 50), phase departures up to 60° can be found in the results.

The type of inconsistencies found in these results, added to the fact that, as it has been pointed out at the end of Section 4.2.1, the L-band signal might penetrate through the ice cover, motivated us to perform an interferometric analysis similar to what will be explained in Chapter 5 for dry snow. A simple two layer model (with air/sea-ice and sea-ice/sea-water interfaces) was constructed to get the simulated values of polarimetric ratio and POPI shown in Figure 66. The amplitude and frequency of the fluctuation pattern obtained basically depend on the attenuation and thickness of the ice layer respectively. As we can see, there is good agreement with the results obtained, however, to reach such frequencies at these low elevations requires ice depths from 60 to 80 meters, which is not realistic in our current scenario. Given the limitations of this dataset, specially for the lack of reliable absolute values and discontinuities in RAW acquisition, further research on POPI is out of the scope of this work.

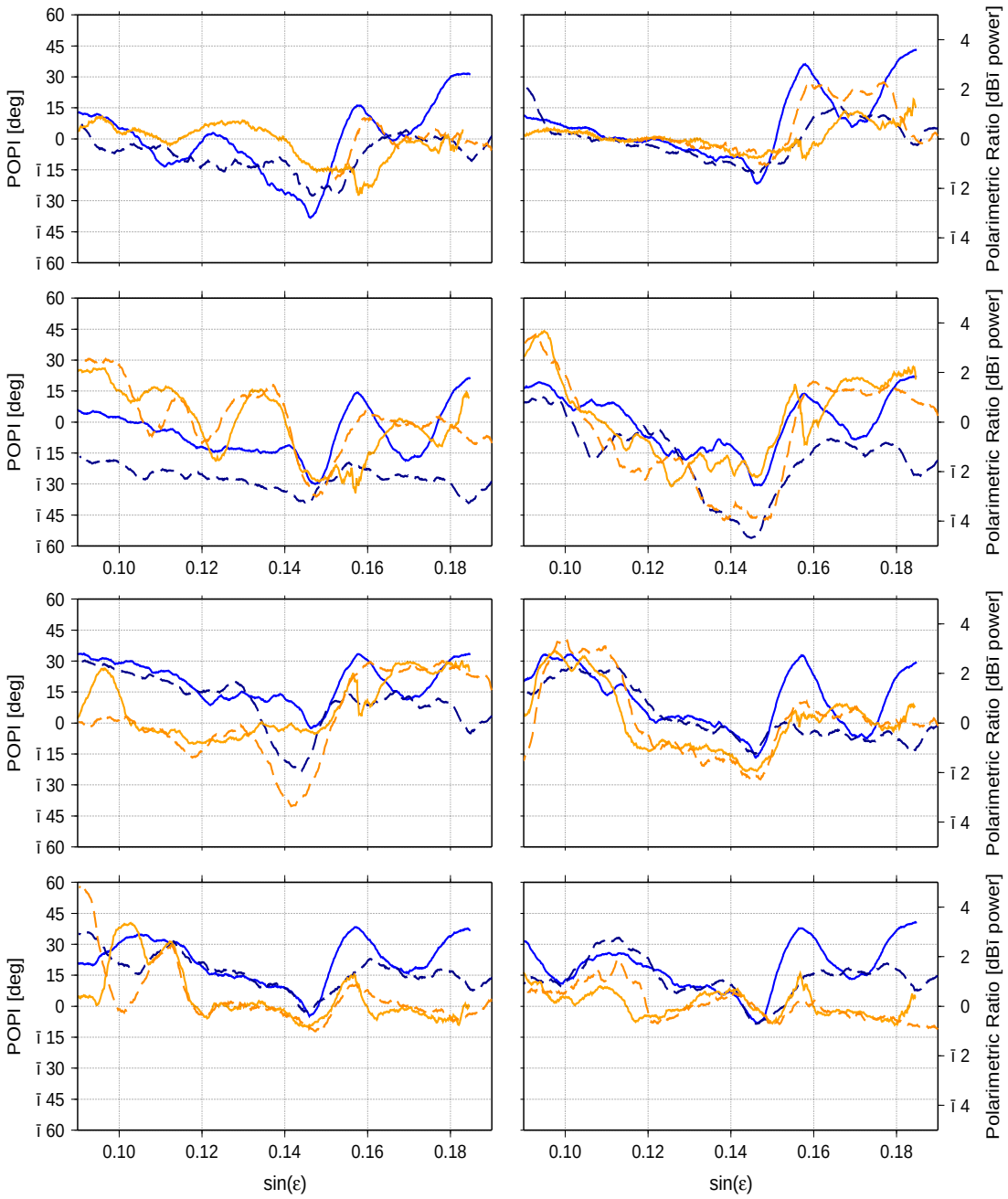

Figure 62.: Comparison between POPI (orange) and polarimetric ratio (blue) measurements for PRNs 7 (dashed line) and 25 (solid line) as a function of $\sin(\varepsilon)$ in different daily panels: from left to right and up to down, DoY 17 until 24.

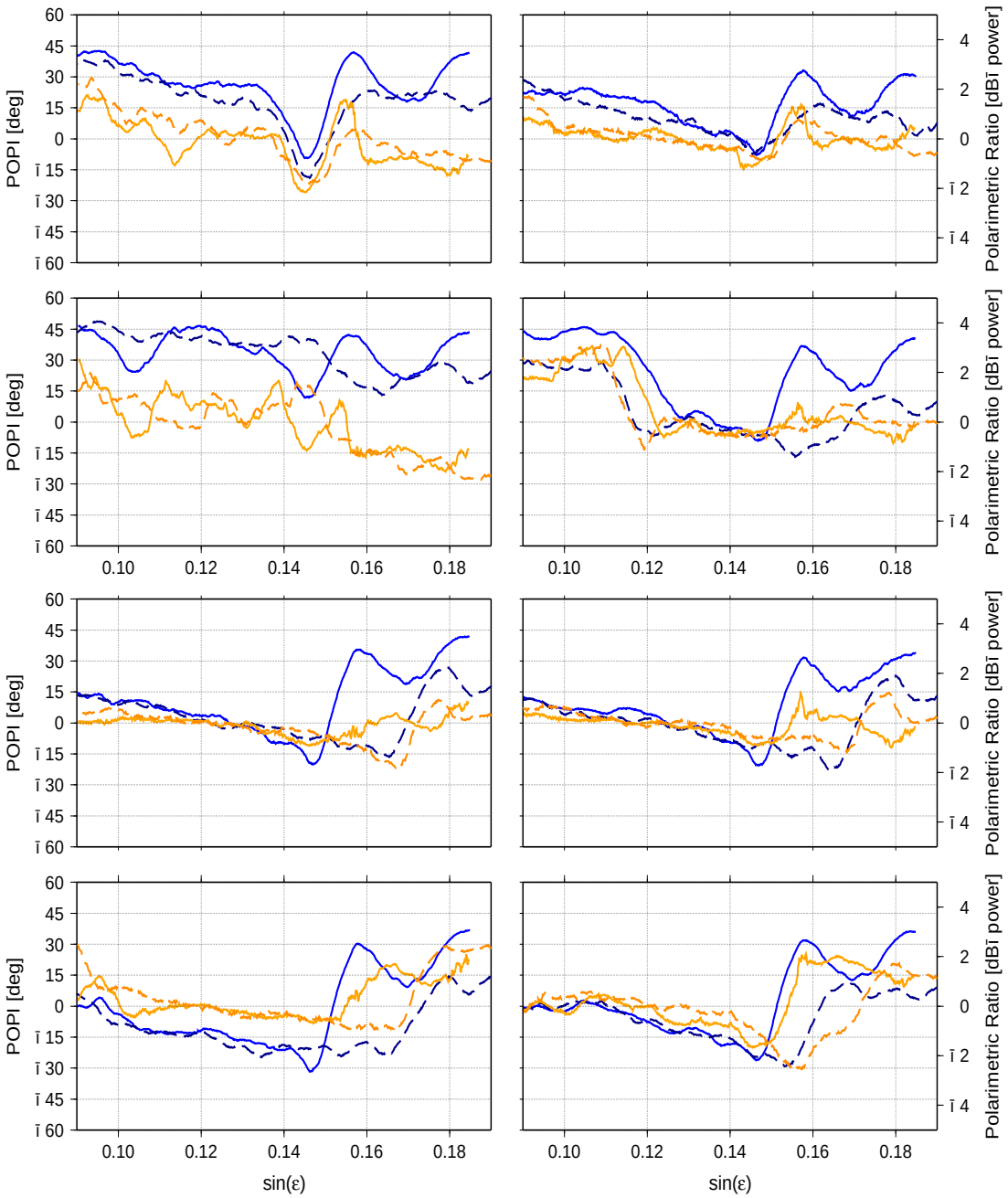

Figure 63.: Comparison between POPI (orange) and polarimetric ratio (blue) measurements for PRNs 7 (dashed line) and 25 (solid line) as a function of $\sin(\varepsilon)$ in different daily panels: from left to right and up to down, DoY 25 until 32.

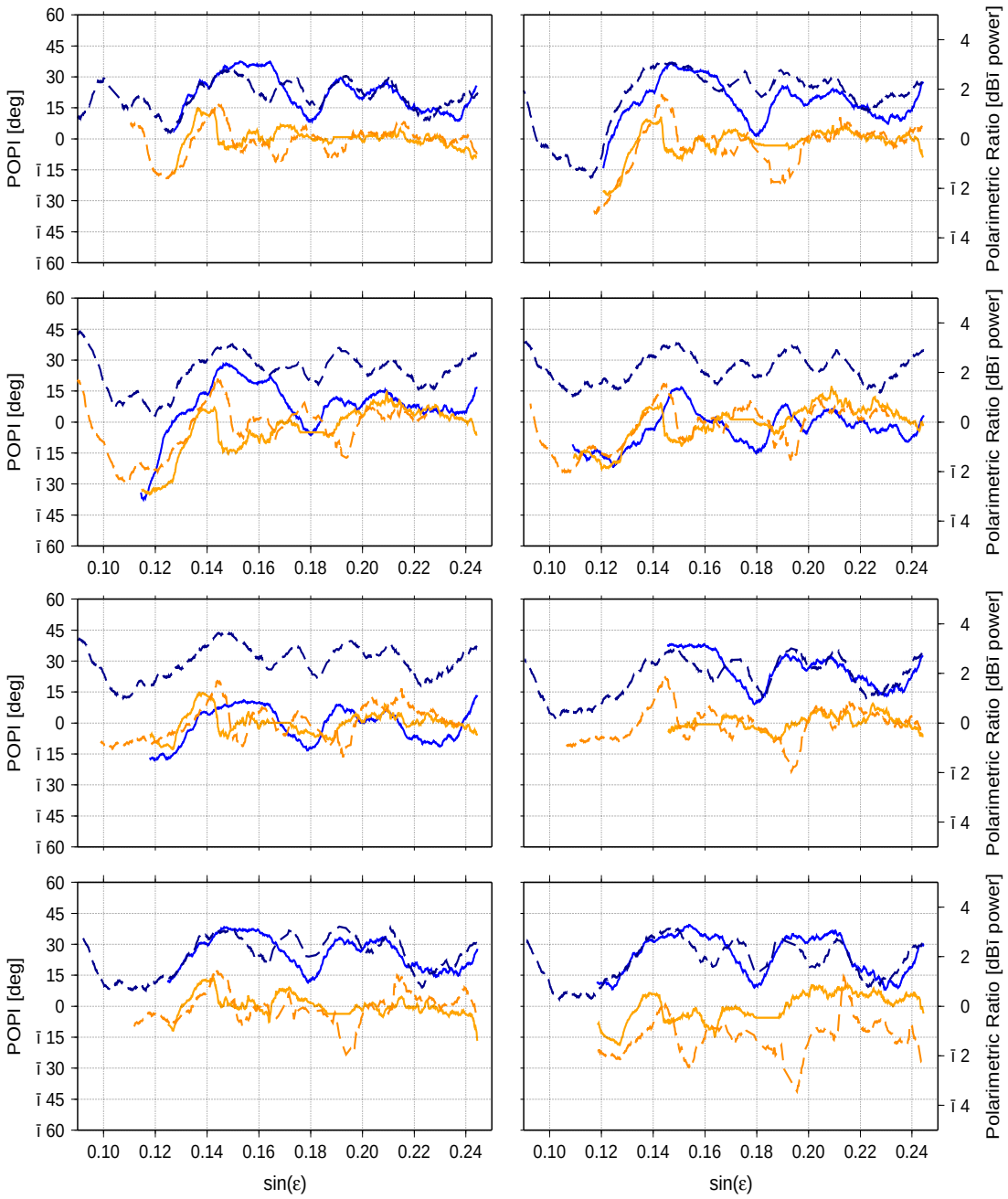

Figure 64.: Comparison between POPI (orange) and polarimetric ratio (blue) measurements for PRNs 2 (dashed line) and 20 (solid line) as a function of $\sin(\varepsilon)$ in different daily panels: from left to right and up to down, DoY 60 until 67.

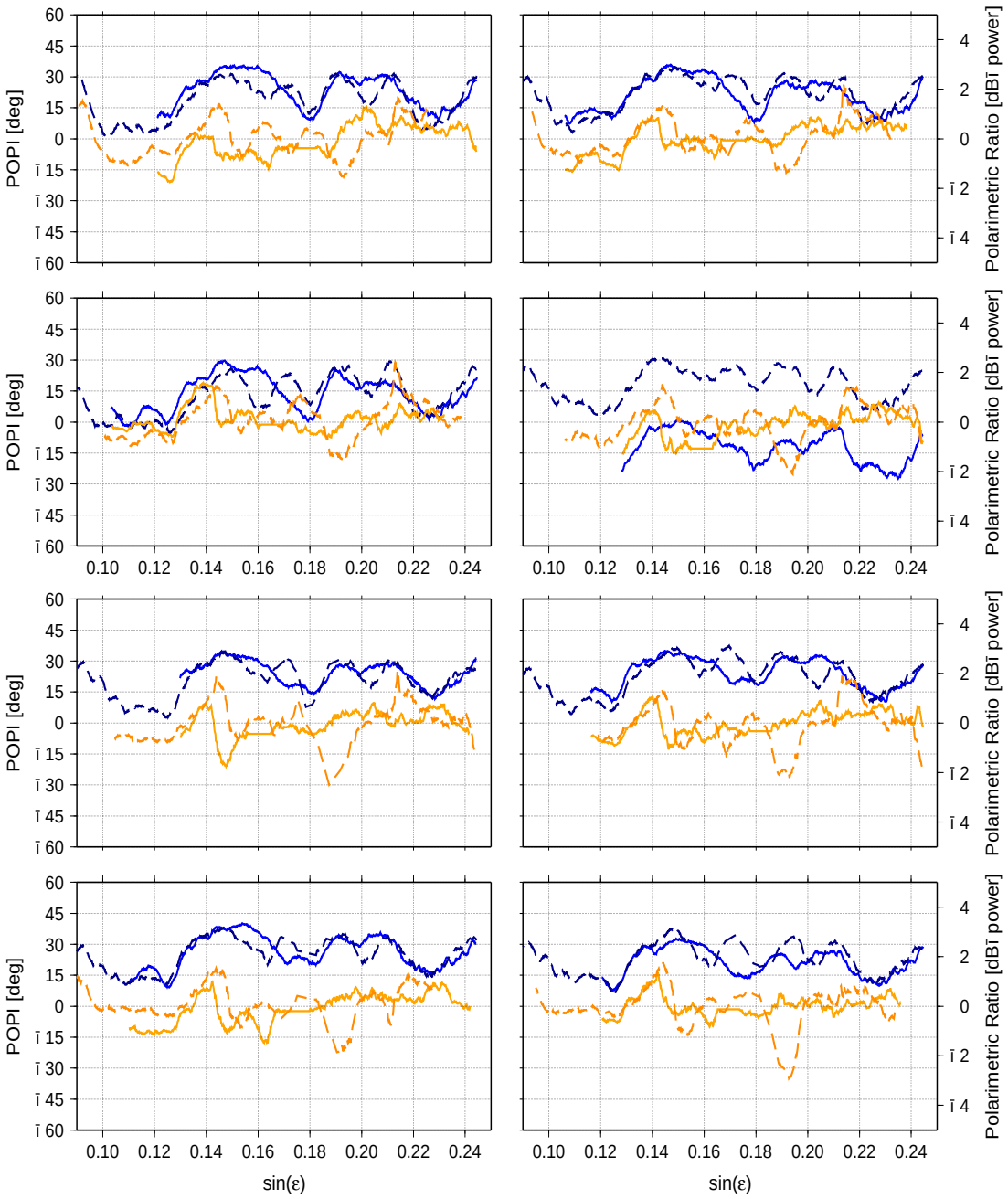

Figure 65.: Comparison between POPI (orange) and polarimetric ratio (blue) measurements for PRNs 2 (dashed line) and 20 (solid line) as a function of $\sin(\varepsilon)$ in different daily panels: from left to right and up to down, DoY 68 until 75.

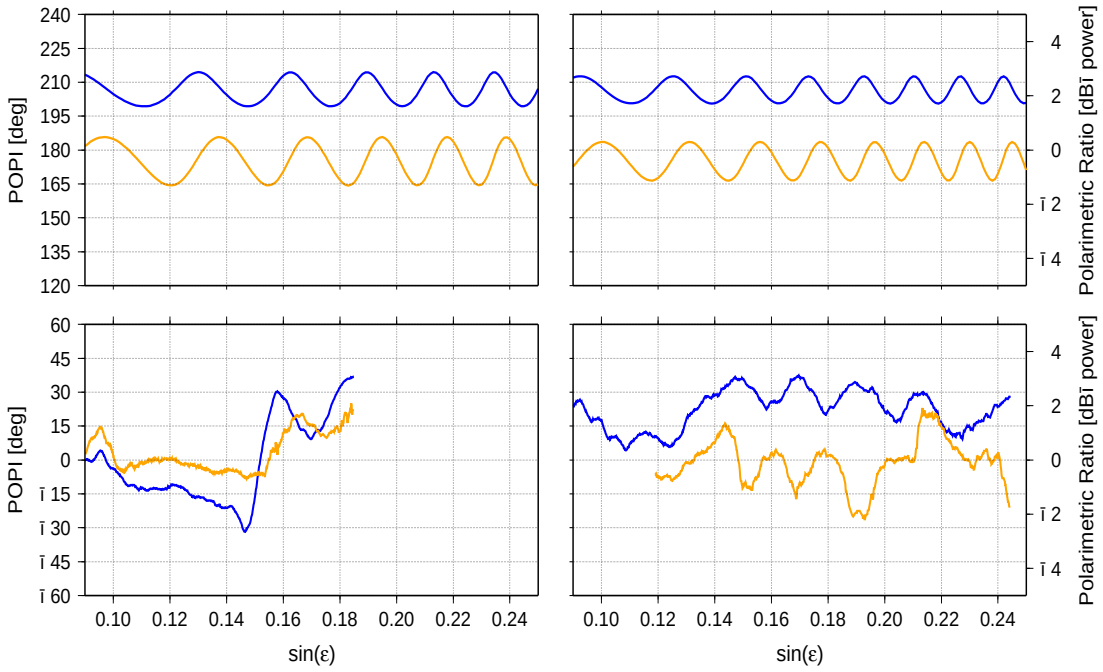

Figure 66.: Comparison between POPI (orange) and polarimetric ratio (blue) simulations with a 2-layers model and real measurements as a function of $\sin(\varepsilon)$ in different panels: [Up-Left] Simulation with a sea-ice layer 60 meter thick. [Up-Right] Simulation with a sea-ice layer 80 meter thick. [Down-Left] Results obtained for PRN 25 from DoY 31. [Down-Right] Results obtained for PRN 2 from DoY 73.

4.2.2.3 *Rough estimation of sea ice state in the experimental site*

Sections 4.2.2.1 and 4.2.2.2 have shown the daily evolution of roughness and reflectivity retrievals obtained and compared with ancillary measurements with lower spatial resolution, limiting then the analysis to the temporal scale. A proper way then to analyze the signatures found in the data and to represent both its temporal and spatial variation is what will be defined here as **global campaign plot**: a two-dimensional plot of a variable at a particular ground track (PRN), as a function of time and sinus of the elevation. Figure 67 gives an example of how a global campaign plot is made. In the present section, the results are compared with the available ice charts provided by DMI and using this form of representation in all the cases. Further details of this ancillary measurement are given in Appendix D.3. Despite that the spatial resolution of the ice charts is still lower to detect all the expected variations along the ground tracks from GPS-R (as shown by the PALSAR's images in Figure 128 at Appendix D.8), they will provide an approximation of the location of the most significant changes over the ice cover. In addition, this type of representation allows to check the consistency and repeatability of the GPS retrievals among different satellites.

In order to analyze the spatial diversity of the results, three pairs of ground tracks have been chosen to illustrate the retrieved parameters at different areas from the experimental site. From Figures 68 to 73, the results from PRNs 25/28 –Western location–, 20/2 –central location– and 31/29 –Eastern location– are displayed. Each of these figures contains six panels (four in the last pair, due to absence of RAW data within the considered time period) with the following information: on top, sea ice concentration and form from DMI's ice charts interpolated along the GPS-R ground track; in the middle (bottom for the last pair), the retrievals obtained with INT observables, polarimetric ratio and *MSS* ; at the bottom, the retrievals obtained with RAW observables, POPI (adding to each daily track a fixed offset obtained as a function of the polarimetric ratio's median value) and

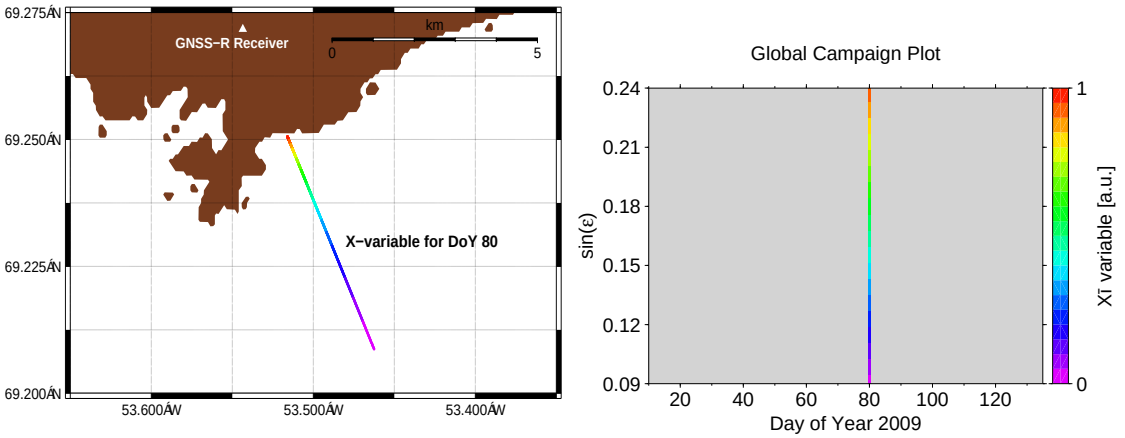

Figure 67.: Example of how to make a global campaign plot: [Left] ground track for a given X-variable and PRN during arbitrary DoY 80. [Right] Global campaign plot for X-variable and the given PRN (by assuming the only contribution from the left panel). The spatial variation (across the PRN's ground track) in the resultant Global campaign plot is given as function of sinus of the elevation (Y-axis), while the temporal evolution is given by the days of the campaign (X-axis).

RMS_H (only results from LHCP are plotted, given that those from RHCP show similar behavior with less dynamic range as seen in Figure 46). This panel distribution splits the results from each figure in two columns, on the left column we can contrast the reflectivity retrievals against sea ice concentration (whose relationship was already shown in Section 4.2.2.2), while the right column provides the comparison of the roughness measurements with ice form. This last representation has three categories: (1) ice free or growlers, (2) small to giant floes and (3) fast ice. The first category will be dominated by the effect of open waters, then showing relatively high values of surface roughness. The second case will correspond to early stages of sea ice, which represent a smoother reflecting surface. Finally, the term *fast ice* refers to the ice anchored to the coast and has the characteristic that, although being fixed to land, it still moves with the tides, contributing then to the development of cracks and fissures in the ice cover and therefore, increasing significantly its roughness without major changes on its permittivity.

By checking the different GPS retrievals from Figures 68 to 73, we can see that there is general good agreement between the different PRNs from similar locations. There is also consistency and repeatability on the results in both temporal and spatial scale. Regarding the comparison against the ancillary measurements from DMI's ice charts, we can observe a consistent correspondence in the temporal evolution with their related INT observables and, in spite of the relatively poor spatial resolution, we can even distinguish similar shape patterns between them (specially for the higher values). In the case of RAW observables, the POPI measurements show the same features that were found in Section 4.2.2.2 when comparing with polarimetric ratio: good agreement in the general variations and different fluctuations along the track when higher values of polarimetric ratio are reached. On the other hand, the results of RMS_H show important discrepancies with the retrieved *MSS* (although there are common patterns like the consistent increase during the period between DoY 80 and 115). In fact, they demonstrate better similarities with the polarimetric ratio, revealing then that the impact of RMS_N in RMS_ϕ hinders the proper retrieval of RMS_H (the lower the peak of LHCP waveforms, the higher the polarimetric ratio and the contribution of RMS_N in RMS_ϕ).

Finally, we can conclude that retrievals obtained from INT observables show better results and they may help us to make a rough characterization of the sea ice cover in our area of interest. From Belmonte et al. (2009) we know that basically, permittivity goes down with the time evolution of the ice cover, while roughness gets a minimum value during its formation (new ice) and increases for consecutive stages. In our experiment, by looking the evolution of polarimetric ratio and *MSS* from Figures 71 to 72 (corresponding to a wider central location, although the others show a similar behavior), we could assume that, after its formation from open waters, the ice cover evolves from *new ice* to *young ice* from DoY 15 to 80. From then on, while the polarimetric ratio keeps stable levels, the retrieved *MSS* have a sudden increment until DoY$\sim$ 115, which agrees with the behavior of *fast ice*. Afterwards, both parameters decrease until they get again typical values for open waters around DoY 130. Notice that this description matches with the results provided by the ice charts, enabling the possibility to infer a rough characterization of the sea ice cover (evolution from new to young and fast ice) that seems realistic in a coastal Polar environment.

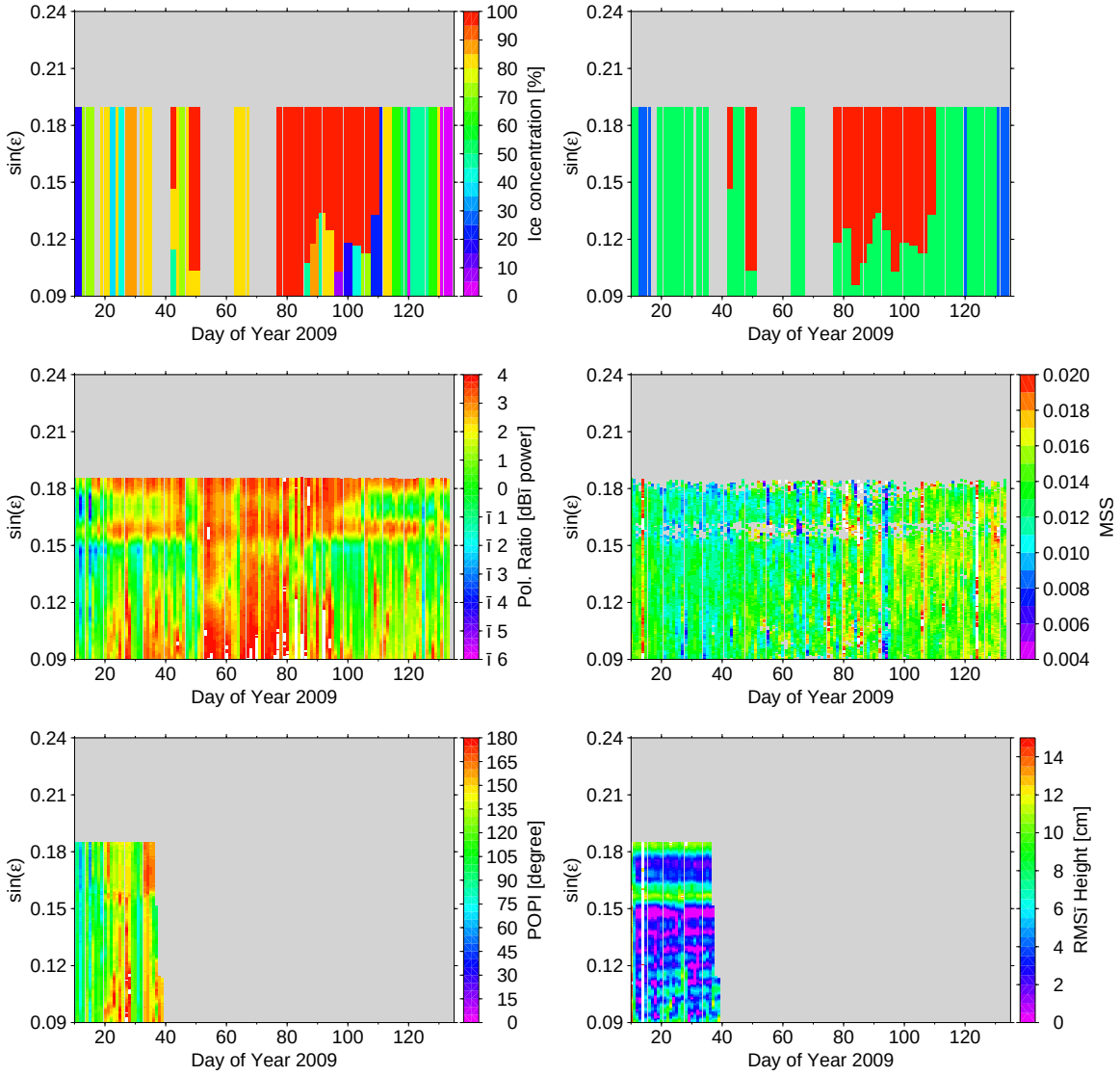

Figure 68.: Global campaign plots from PRN 25. In all cases, a gray background is added to mark the lack of data and those samples out of the range are plotted in white. From up to bottom and left to right (matrix notation): [1,1] Ice concentration from DMI's ice charts. [1,2] Ice form from DMI's ice charts (ice free or growlers in blue, small to giant floes in green, fast ice in red). [2,1] Polarimetric ratio. [2,2] Retrieved MSS. [3,1] Corrected POPI. [3,3] RMS_H from LHCP samples.

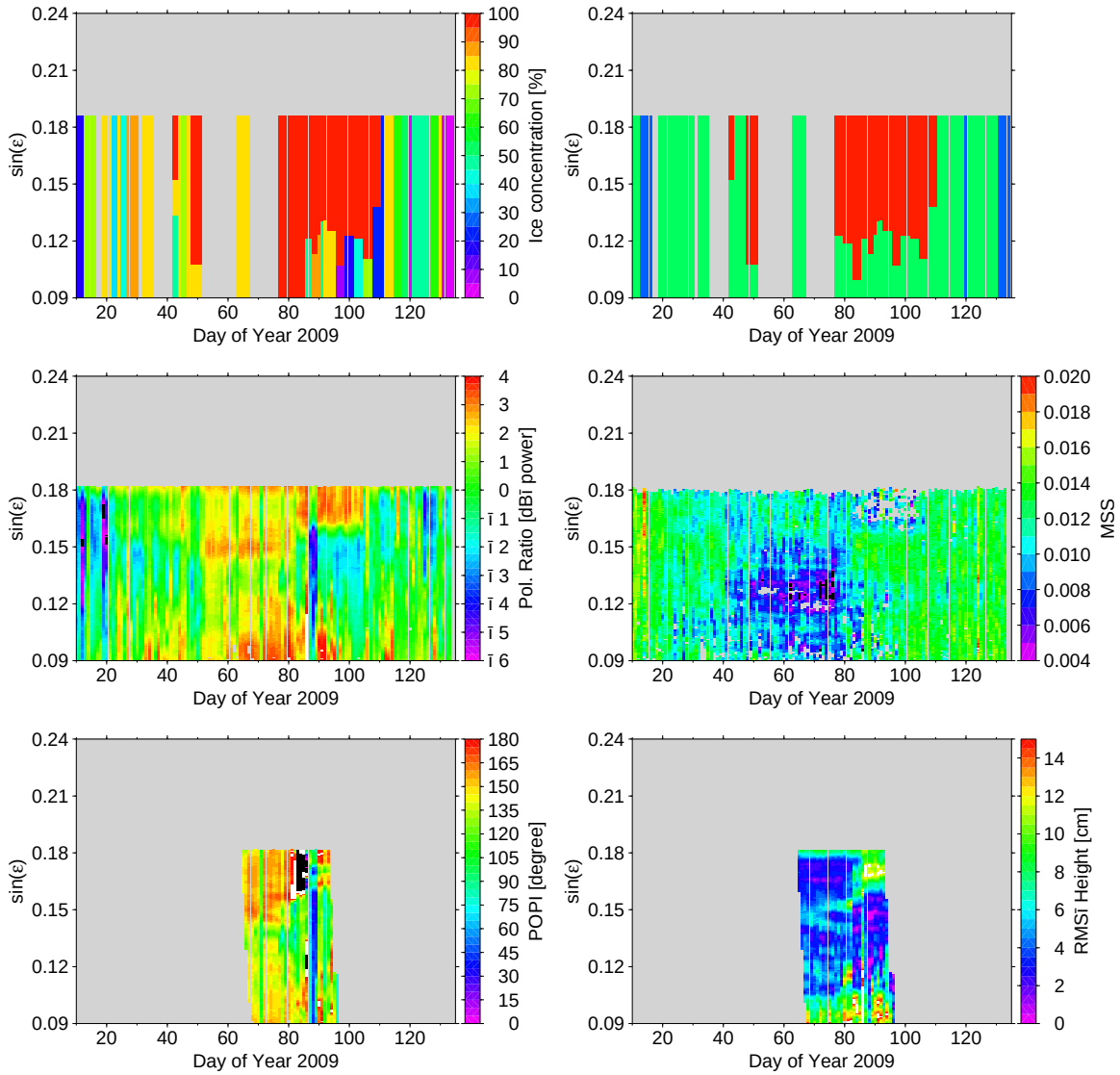

Figure 69.: Global campaign plots from PRN 28. In all cases, a gray background is added to mark the lack of data and those samples out of the range are plotted in white. From up to bottom and left to right (matrix notation): [1,1] Ice concentration from DMI's ice charts. [1,2] Ice form from DMI's ice charts (ice free or growlers in blue, small to giant floes in green, fast ice in red). [2,1] Polarimetric ratio. [2,2] Retrieved MSS. [3,1] Corrected POPI. [3,3] RMS_H from LHCP samples.

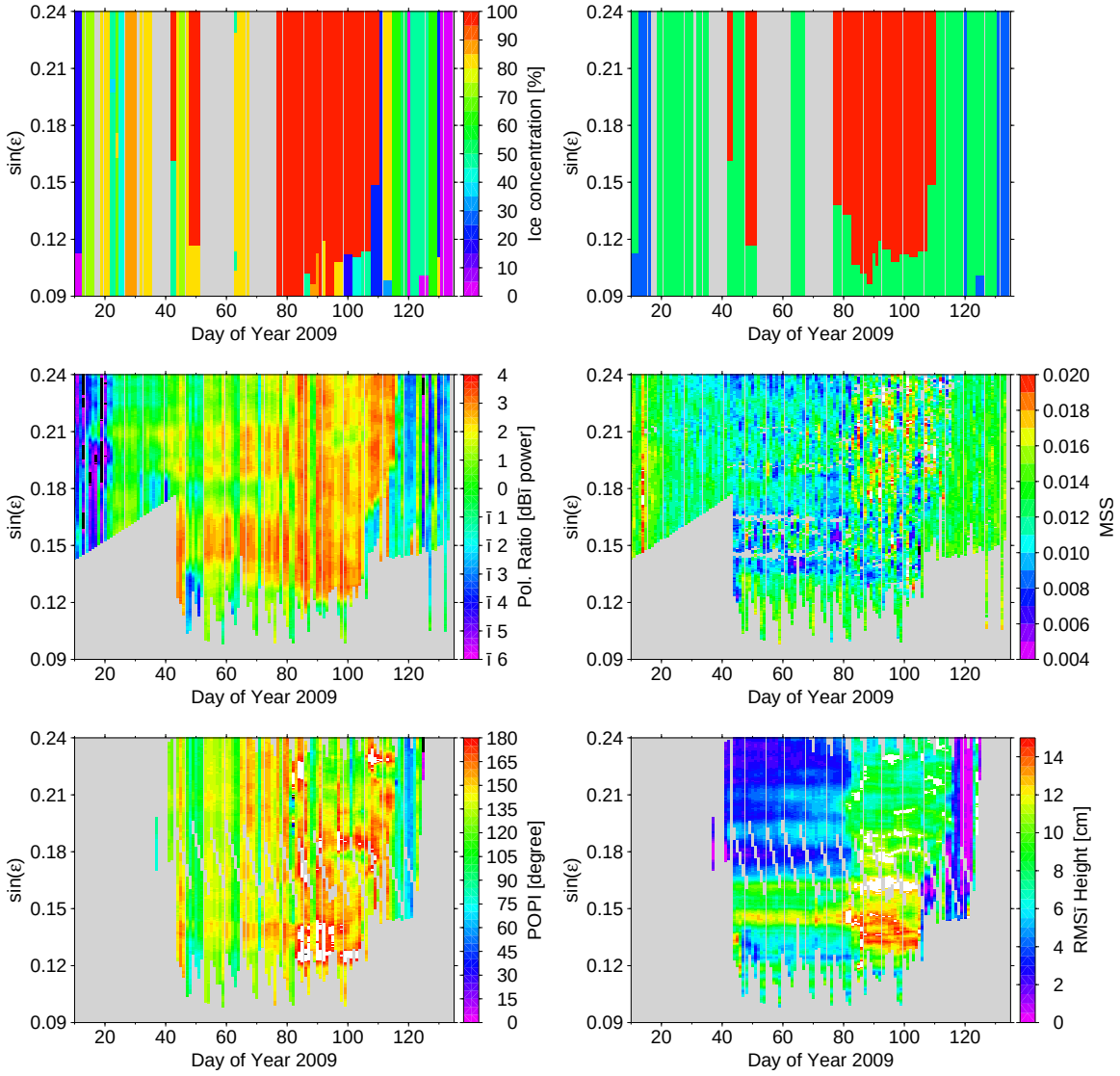

Figure 70.: Global campaign plots from PRN 20. In all cases, a gray background is added to mark the lack of data and those samples out of the range are plotted in white. From up to bottom and left to right (matrix notation): [1,1] Ice concentration from DMI's ice charts. [1,2] Ice form from DMI's ice charts (ice free or growlers in blue, small to giant floes in green, fast ice in red). [2,1] Polarimetric ratio. [2,2] Retrieved *MSS*. [3,1] Corrected POPI. [3,3] RMS_H from LHCP samples.

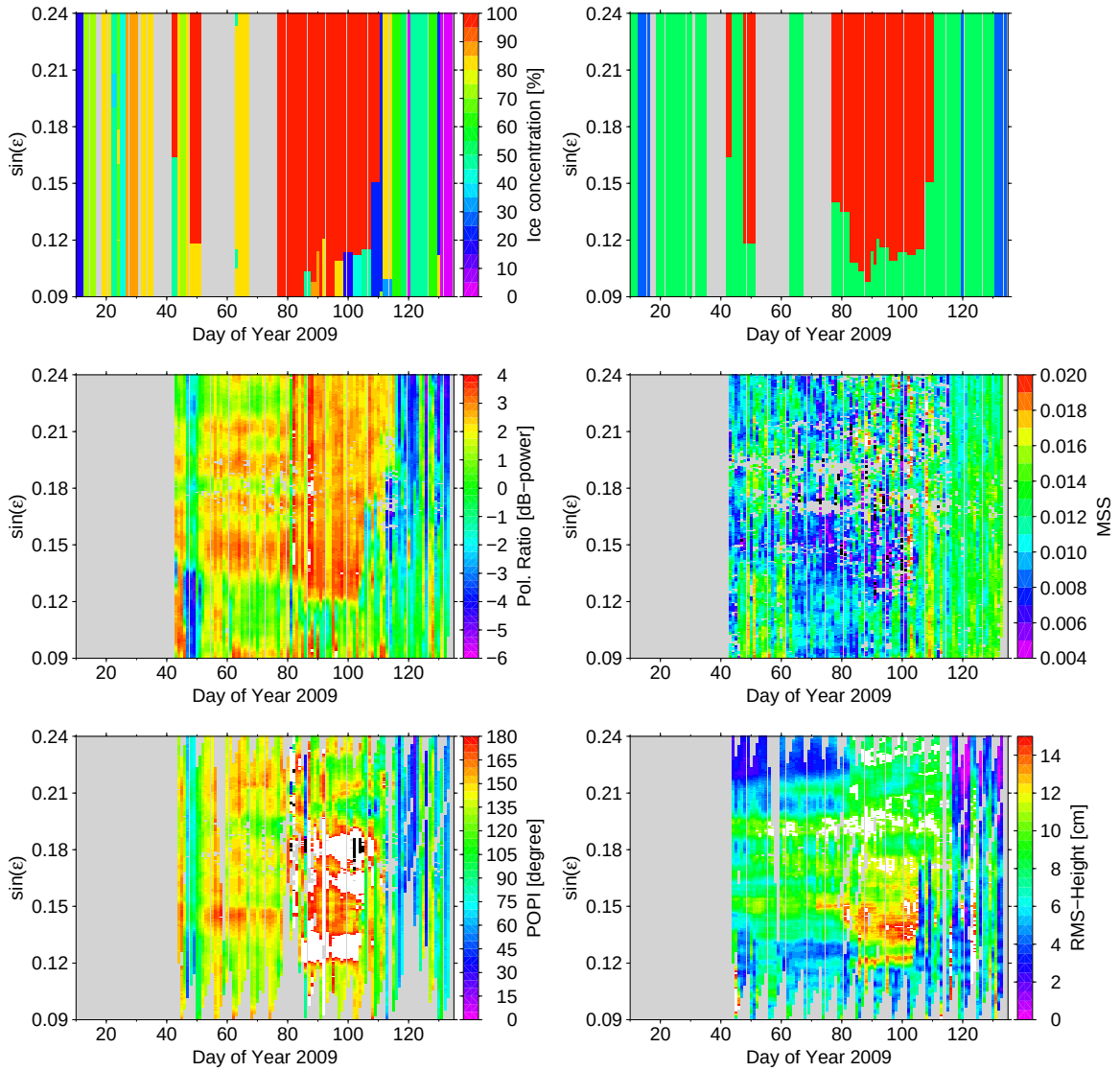

Figure 71.: Global campaign plots from PRN 2. In all cases, a gray background is added to mark the lack of data and those samples out of the range are plotted in white. From up to bottom and left to right (matrix notation): [1,1] Ice concentration from DMI's ice charts. [1,2] Ice form from DMI's ice charts (ice free or growlers in blue, small to giant floes in green, fast ice in red). [2,1] Polarimetric ratio. [2,2] Retrieved MSS. [3,1] Corrected POPI. [3,3] RMS_H from LHCP samples.

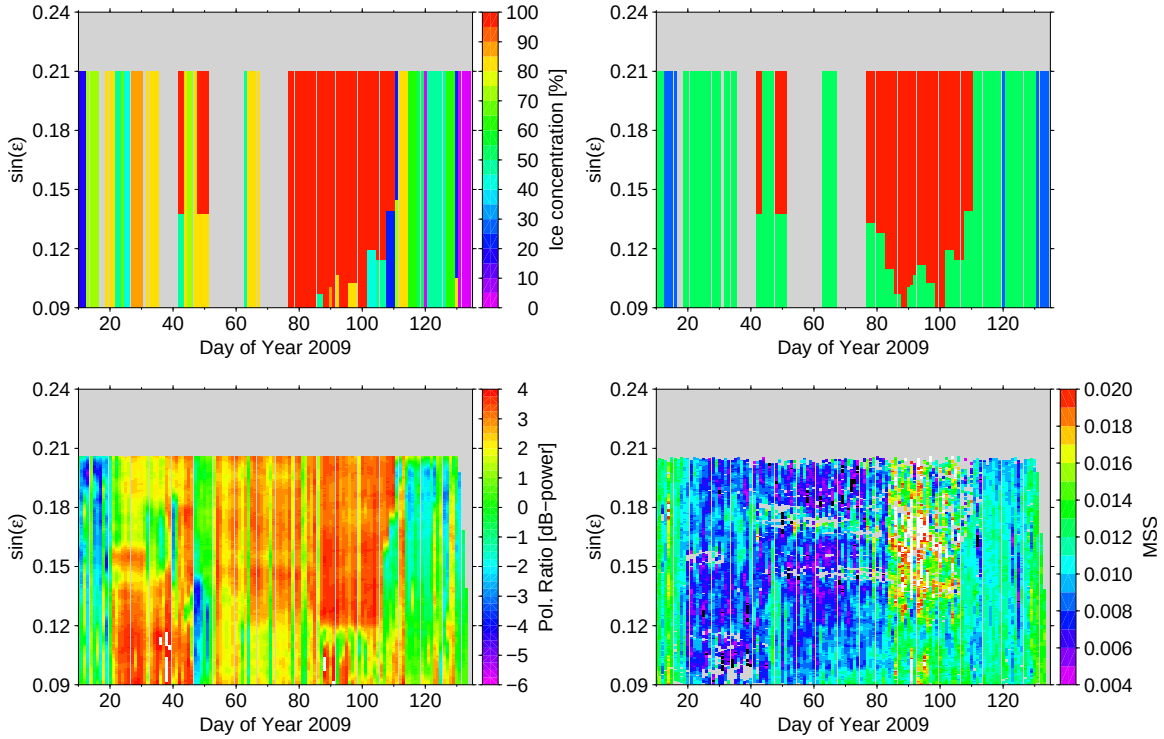

Figure 72.: Global campaign plots from PRN 31. In all cases, a gray background is added to mark the lack of data and those samples out of the range are plotted in white. From up to bottom and left to right (matrix notation): [1,1] Ice concentration from DMI's ice charts. [1,2] Ice form from DMI's ice charts (ice free or growlers in blue, small to giant floes in green, fast ice in red). [2,1] Polarimetric ratio. [2,2] Retrieved *MSS*.

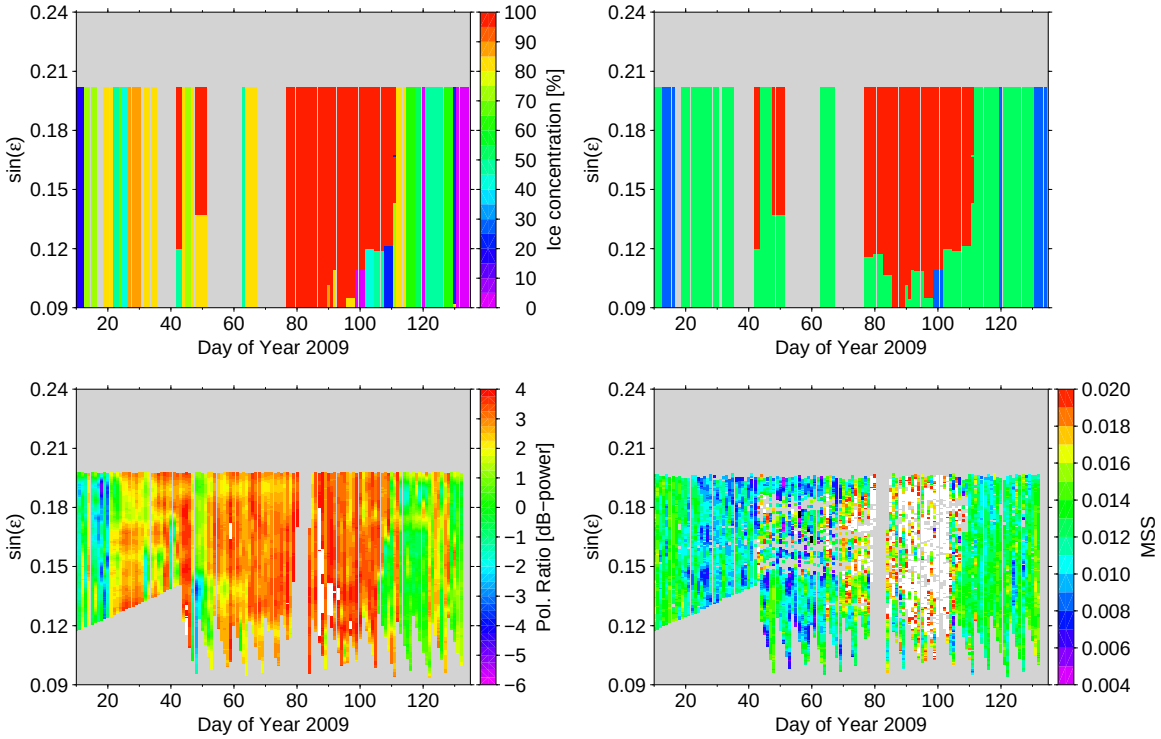

Figure 73.: Global campaign plots from PRN 29. In all cases, a gray background is added to mark the lack of data and those samples out of the range are plotted in white. From up to bottom and left to right (matrix notation): [1,1] Ice concentration from DMI's ice charts. [1,2] Ice form from DMI's ice charts (ice free or growlers in blue, small to giant floes in green, fast ice in red). [2,1] Polarimetric ratio. [2,2] Retrieved *MSS*.

4.2.3 CONSIDERATIONS FOR A SPACEBORNE SCENARIO

Even thought the results of this experiment show the potential detection of sea ice and its characterization by means of reflected GPS signals from a fixed platform, the final application of this technique should be performed from satellite receivers in order to achieve global coverage. The extrapolation of these results to a spaceborne scenario is therefore needed.

A first consideration is that the peak power of the waveforms will be substantially lower, due to higher propagation losses and the signal's spreading over range delay and frequency shifts (increase of the glistening area). In spite of this, the detection of these signals from space has been already probed experimentally after comparing ice concentration estimates from AMSR-E with GPS reflections collected on-board the UK-DMC satellite (Gleason, 2010) with a low gain antenna. Nevertheless, better antenna gains would be needed in order to obtain enough SNR in the reflected signals to properly characterize rougher and less reflective stages of sea ice. Taking into account that at the same time, different elevation angles of observation are desired for achieving spatial coverage, a beamforming strategy like in Martín-Neira et al. (2011) seems to be the best option.

With hundreds of kilometers of distance from the surface level, direct-reflected signals delay contamination will not affect in a LEO spaceborne scenario. In addition, with a proper satellite design, near-multipath will not be present either. These two conditions will imply a significant improvement in the results obtained compared to the fixed-platform case.

Regarding Doppler effects, the velocity of the receiver in a LEO satellite ($\sim$7.5km/s) leads to different Doppler-frequency contributions over the reflecting ground region. However, previous experiments with real GPS reflections show how these frequencies can be properly determined from space (Lowe et al., 2002a; Gleason, 2010).

When comparing delays from direct and reflected GPS signals in spaceborne scenarios, the differential ionospheric delay has to be corrected. Since the refractive index of the ionosphere is frequency dependent, to follow a multi-frequency approach, typically using L1 and L2 observations, or L1 and L5 as suggested in Martín-Neira et al. (2011), would solve this problem.

Finally and regarding phase measurements, the recovery of the transmitted carrier phase from a LEO satellite still remains unclear (Gleason, 2010). The coherence of the signal from GPS reflections over sea ice should be properly studied for space scenario. That includes also the effect of speckle noise and the impact of roughness. To asses this problem is not straightforward and it remains as an open question that will require a deeper analysis.